RHEINISCHE FRIEDRICH–WILHELMS–UNIVERSITÄT
BONN

PULSAR SEARCHING AND TIMING WITH THE ARECIBO AND EFFELSBERG RADIO TELESCOPES

Dissertation

zur

Erlangung des Doktorgrades (*Dr. rer. nat.*)

der

Mathematisch-Naturwissenschaftlichen Fakultät

der

Rheinischen Friedrich–Wilhelms–Universität, Bonn

vorgelegt von

Jose Guadalupe Martinez

aus

Brownsville, Texas, U.S.A.

Bonn 2019

Angefertigt mit Genehmigung der Mathematisch-Naturwissenschaftlichen Fakultät der Rheinischen Friedrich–Wilhelms–Universität Bonn

1. Referent: Prof. Dr. Michael Kramer
2. Referent: Prof. Dr. Norbert Langer
Tag der Promotion: 24.06.2019
Erscheinungsjahr: 2019

Diese Dissertation ist auf dem Hochschulschriftenserver der ULB Bonn unter
http://nbn-resolving.de/urn:nbn:de:hbz:5n-55403 elektronisch publiziert

RHEINISCHE FRIEDRICH–WILHELMS–UNIVERSITÄT BONN

Abstract

by Jose Guadalupe Martinez

for the degree of

Doctor rerum naturalium

Pulsars are rapidly rotating, highly magnetized, neutron stars; they are remnants of supernova explosions from massive stars. They emit beams of electromagnetic radiation from their magnetic poles that can be seen mostly in radio. Ever since the discovery of the first radio pulsar in 1968 by Jocelyn Bell; their population keeps increasing at an ever much faster rate as our computing technologies and radio telescopes instrumentations advances. Recent advancements has given an increase in the discovery of fast spinning pulsars. Most of them are recycled pulsars; which are old ($\gtrsim 10^8$ yr) neutron stars that are descendants from a close, interacting binary systems. They have extraordinary rotational stability due to being spun-up (recycled) to fast spin periods (few to tenths of milliseconds) by accretion of mass and angular momentum from their companion star. Their extreme properties have made them fundamental tools for a broad range of applications, including the study of ultra-dense matter, the tests of relativistic theories of gravity, and the search for low-frequency gravitational waves.

Of the $>$ 2600 pulsars known to date, the majority were discovered in blind, large-scale searches at radio wavelengths. This thesis will focus on two large pulsar surveys conducted at the Arecibo and Effelsberg radio telescopes. The Arecibo 327-MHz Drift Scan Pulsar survey (AO327) is searching for pulsars and radio transient signals in the entire Arecibo field of view (declination range $-1°$ to $38°$). The High Time Resolution Universe - North Pulsar survey (HTRU-N) is conducted at Effelsberg to search the whole sky accessible to the telescope (declination $\geq -31°$) for pulsars.

In Chapter 1, I will summarize the formation, structure, and behavior of radio pulsars. In Chapter 2, I present the basics of standard pulsar searching methodology with a focus of the Arecibo and Effelsberg radio telescopes surveys. The full potential of a pulsar survey can only be realized through the follow-up of its discoveries. The following chapters will be on the discoveries I have made in AO327. In Chapter 3 and 4, I will present the discovery and follow-up of PSR J0453+1559 and PSR J1411+2551, which both are double neutron star systems. Chapter 5, will also be on the discovery and follow-up of 6 recycled pulsars, five which are in a binary and one isolated millisecond pulsar. Lastly, Chapter 6 closes with a summary of the most important scientific results derived as part of this thesis and additional discussion on the future work.

Acknowledgements

Finally, writing my acknowledgements, a bittersweet moment, as it is the final piece of this thesis!

There are many people I would like to thank and I will try my best to mention everyone. First, I would like to thank my advisors that supported me during my time here at the MPIfR, David Champion and Paulo Freire. Both of you have been very patient and gave me the all the advice and mentorship I needed not only to complete my work in this thesis but you also helped me to prepare for future challenges and endeavours.

David, thank you for always being there for me, making sure I never veer off from the ultimate goal of, how we like to say in the south 'git er done!'. Your advice has been very important for me in my thesis work and future goals. If it was not for you, I would have probably never finished this thesis.

Paulo, from the very start, you accompanied me to Germany and guided me in the beginning of my studies here with the many, many exciting discussions about pulsars that genuinely kept me motivated in my work. But most of all, I am grateful for being able to call you a friend.

I would also like to thank Michael Kramer for having created such an incredible Fundamental of Physics group (fundi); that is, in my opinion, the best place for any student that wants to become a pulsar astronomer. Which comes to my next thank you, the fundi group. Your support that has been vital in my work here, thank you everyone for all the time you have given to me, letting me ask many questions, especially Gregory (software guru king), Ralph (having a few beers with me in the beginning), and Aris (joining the student lunch table). Also, I would like to thank the administration of MPIfR, special thanks go to Kira Kühn, Barbara Menten, and especially Tuyet-Le Tran, y'all have been very welcoming and helpful from the beginning to the end of my time here.

Now comes the hard part, to thank all of my friends at both MPIfR and the other side of the wall, AIfA. Special thanks to the first office mates in the basement room Alice, Marina, Jason, Pablo, Phillip, Carolina, Ancor, Andrew, and Eleni♡. It was never a dull moment in that office and was a really good starting place to meet most of the students in my group. Pablo, thank you so much for helping me at the beginning with getting an apartment, phone, Internet, electricity, water, bank account, literally everything I needed to survive here in Germany! Also, for all the good times we had of watching Anime as gluttons with Ancor, Frühlingsfest at Stuttgart, visits to Granada and your incredible hospitality. You were the first person I called a friend here in Germany. Also Felipe, even though your time was a bit short here in Germany, we really made the best of it! Thanks for coming with me so many times for a pint at James Joyce and Fiddlers.

Next thanks goes to my second office mates at the new awesome office E0.10, the four original amigos, Marcel, Maja, and Leon. We had a good time together by truly making an effort to get to know each other. Now to the four amigos part *deux*, the remix: Henning, Mary, and Leon, which I spent the majority of my time here with. Thank you guys for always caring for one another, random cool gifts from around the world, and for making the office feel like a home away from home. Henning, *takk* for being the best Icelandic friend I've ever had (and also the only), I will never forget the Rob Zombie concert and the epic gaming night of ice climbers at level 1. Mary, gracias por todos los BBQs, fiestas, y por nunca pasar un momento sin reír en la oficina. Leon, you were the last survivor of the four amigos, thanks for that, and for being a good friend. You are the one that introduced me to the world of climbing and really pushed me

to get out of my comfort zone in heights. Quick shout-out to the new officemate Joscha!

Other MPIfR students to thank are, Grande Alessandro aka gym buddy, Natalia and Marina priviet!, $\chi\omega\rho\iota\acute{\alpha}\tau\eta$ Tillemachos, el caballero Nicolas, Andrew for taking me to the doctor during our IMPRS retreat, Hans my new climbing mentor and master of balance, Joonam Fateme, Michael Mattern for introducing me to good German beer, Arshia for watching Pepper with me, and Melisse the cow lover.

I would like to thank my friends from the other side of the wall, AIfA peeps Abel, Ana, David, Nathan, Toma, Eleni, and Vica. For all those Fridays at Fiddlers, exciting dart tournaments, football matches, and especially all those sophisticated conversations about anything else other than work (for the most part). A big thank you to the Fiddler's crew Gosia, Ida, Victoria, Yannik, Roberto, Yannis, Kieran, James, Mauricio, Miguel, especially Maggie and Brian; y'all made us feel like home for the past 3 years every Friday.

For friends back home, I have not forgotten about y'all! Emma Handzo, thank you for being the first friend to visit me in Germany, teaching me how to cook, and especially for helping me to proofread this thesis. Adriana Elizondo, thank you for all our European travels together. Ever since our high school adventures, we never seemed to stop travelling and let us not break the trend! Victoria, for visiting me as well and being very excited when she saw I lived a block away from Robert Schumann last house. Also thanks to all my brothers from another mother: Fabian, Damon, Eddie, Pyro, Ricky, Grady, Wynton, Kenny-B, J.D., Frank, Jesse, Sent, Gio, and Rico.

I would like to really thank two influential people in my life, my old advisor Fredrick Jenet (Rick) and especially my middle and high school science/physics teacher Mr.Miller! You two have been a constant support in my life and introduced me to the world of pulsars.

Now, of course, Eleni♡, I can't write enough words to express how thankful I am for you. You kept me afloat these past few years with food, food, and your unconditional love.

Y por último quiero agradecer sinceramente a toda mi familia, por toda su ayuda y comprensión aun en la distancia. Quiero agradecer en especial a mis padres, y mis hermanos y hermana por el apoyo y el ánimo que siempre me dan en todo. Sin ustedes, nada de esto habría sido posible. Mamá y papá gracias por siempre luchar por nosotros y hacernos mejores personas cada dia. A mis hermanos, ustedes marcaron el camino que me permitió llegar tan lejos y descubrir nuevos mundos.

Contents

Acronyms used in this thesis

ADC	Analogue-to-Digital Converter
AU	Astronomical Unit
BAT	Barycentric Arrival Time
BB	Binary Barycentre
BH	Black Hole
BT	Blandford & Teukolsky binary model
BWP	Black Widow Pulsar
CO WD	Carbon-Oxygen White Dwarf
DFT	Discrete Fourier Transform
DM	Dispersion Measure
DNS	Double Neutron Star
EoS	Equation of State
EPTA	European Pulsar Timing Array
FAST	Five-hundred-meter Aperture Spherical Telescope
FFT	Fast Fourier Transform
FPGA	Field-Programmable Gate Array
FT	Fourier Transform
FWHM	Full Width at Half Maximum
GC	Globular Cluster
GR	General Relativity
GW	Gravitational Wave
He WD	Helium White Dwarf
HMXB	High-Mass X-ray Binary
IMBH	Intermediate-Mass Black Hole
IMXB	Intermediate-Mass X-ray Binary
IPTA	International Pulsar Timing Array
ISM	Interstellar Medium
LIGO	Laser Interferometer Gravitational-wave Observatory
LMXB	Low-Mass X-ray Binary
MJD	Modified Julian Date
MRP	Mildly Recycled Pulsar
MS	Main Sequence
MSP	Millisecond Pulsar
NANOgrav	North American Nanohertz Observatory for Gravitational Waves
NS	Neutron Star
ONeMg WD	Oxygen-Neon-Magnesium White Dwarf
PA	Linear Polarization Position Angle
PFB	Polyphase Filterbank
PK	Post-Keplerian
PMB	Parkes Multi-Beam Receiver
PPTA	Parkes Pulsar Timing Array
PTA	Pulsar Timing Array
PUPPI	Puertorican Ultimate Pulsar Processing Instrument
RBP	Redback Pulsar
RCP	Right-handed Circular Polarization
RFI	Radio Frequency Interference
RM	Rotation Measure
RVM	Rotating Vector Model
S/N	Signal-to-Noise ratio
SKA	Square Kilometre Array
SMBH	Stellar-Mass Black Hole
SN	Supernova
SNR	Supernova Remnant
TOA	Time of Arrival
UTC	Universal Coordinated Time
WD	White Dwarf

Physical and Astronomical Constants

Speed of light	c	$299\,792\,458$ m s^{-1}
Newton constant of gravitation	G	$6.674\,08(31) \times 10^{-11}$ m^3 kg^{-1} s^{-2}
Planck constant	h	$6.626\,070\,040(81) \times 10^{-34}$ J s
Elementary charge	e	$1.602\,176\,6208(98) \times 10^{-19}$ C
Electron mass	m_e	$9.109\,383\,56(11) \times 10^{-31}$ kg
Proton mass	m_p	$1.672\,621\,898(21) \times 10^{-27}$ kg
Boltzmann's constant	k_B	$1.380\,648\,52(79) \times 10^{-23}$ J K^{-1}
Astronomical unit	AU	$149\,597\,870\,700$ m
Parsec	pc	$3.085\,675\,581\,491\,367\,3 \times 10^{16}$ m
Julian year	yr	$31\,557\,600$ s
Solar mass	$\mathrm{M}_\odot$	$1.988\,55(25) \times 10^{30}$ kg
Solar mass in units of time	$\mathrm{T}_\odot = G\,\mathrm{M}_\odot/c^3$	$4.925\,490\,947 \times 10^{-6}$ s
Nominal Solar radius	$\mathrm{R}_\odot$	$695\,700$ m

Main pulsar data analysis software used in this thesis

Package	Used for	References	Website
`PRESTO`	Pulsar searching	Ransom (2001)	`http://www.cv.nrao.edu/~sransom/presto`
`PSRCHIVE`	Pulsar data reduction	Hotan et al. (2004) van Straten et al. (2012)	`http://psrchive.sourceforge.net`
`DSPSR`	Folding	van Straten & Bailes (2011)	`http://dspsr.sourceforge.net`
`TEMPO`	Timing	–	`http://tempo.sourceforge.net`

Chapter 1

Introduction

Contents

1.1 Pulsars

In 1054 A.D. Chinese astronomers observed a bright object in the sky which they called a "guest star". That bright object happened to be the Crab supernova and was the birth of a neutron star. But this was not realized until the 20th century. In 1934, (Baade & Zwicky, 1934) proposed that a supernova is the transition of an ordinary star into a very compact remnant - a dead, cold star composed mostly of neutrons. They remained theoretical objects until 33 years later, a PhD student named Jocelyn Bell observed something rather strange in her data charts - some periodic tick marks appeared above the noise floor. This unusual signal was a highly regular source of repeating pulses with a periodic rate of 1.337 seconds that appeared at the same sidereal time each day, which led to believe it was a celestial object. This accidental discovery introduced the world to the first radio pulsating star ("pulsar"), CP1919 (Cambridge Pulsed source at an RA of 19 h 19m, which was later renamed PSR B1919+21) (Hewish et al., 1968). This discovery was one of nature's surprises: no one ever predicted these radio pulsations, even up to today

there is no complete model that fully accounts for the radio emission of a pulsar. At the time of the discovery, the physical nature of pulsars was the subject of much debate. It was thought that the pulses might be due to orbital motion of a close binary, or perhaps radial oscillations of a white dwarf star. It was not until the discoveries of the Vela (Large et al., 1968) and Crab pulsars (Staelin & Reifenstein, 1968), with their respective pulse periods of 0.089s and 0.033s, (too fast for white dwarf oscillation or rotation) that scientists were able to put the final pieces of the puzzle together. The generally accepted hypothesis by (Gold, 1968) states that pulsars are highly magnetized, rapidly rotating neutron stars formed only by supernova remnants. This was the beginning of a new field called pulsar astronomy.

1.1.1 Formation

Stars are powered by powerful nuclear fusion in their cores, which creates the principal elements of life. The mass of the progenitor star determines which of the end points is obtained, with the most massive stars evolving into black holes, intermediate star masses into neutron stars, and the least massive stars into white dwarfs. For the purposes of this thesis, we now concentrate on the formation of a neutron star.

The end phase of a massive main sequence star of 8 up to 15 $M_{\odot}$ (Woosley & Weaver, 1986; Lyne & Graham-Smith, 2012) can give birth to a neutron star. Throughout its life, a massive main sequence star sustains itself against gravity by the outward radiative pressure generated by nuclear fusion (Russell, 1931), which happens by burning hydrogen in its core to fuse into helium. But once all the hydrogen is exhausted, the radiation pressure turns off and the star contracts due to the gravitational force stemming from its large mass. The main sequence star starts to shrink, and the large mass being compressed into a smaller space causes the core temperature of the start to increase due to friction. It then becomes hot enough to begin to fuse helium, which gives the star more energy, causing the star to expand into a giant. This then turns into a cycle of exhausting nuclear fuel in the core, contracting again, reheating, and reigniting fusion. At each stage, heavier elements are being fused together, from helium, to carbon, to oxygen, to neon, to sodium, to magnesium, to silicon, and ending at iron. The process stops because fusing iron into heavier elements is a endothermic process. At this stage, the star cannot support its own weight and is unable to fuse any more elements together, so it suddenly collapses in a core-collapse supernova. During this event, the strong nuclear force causes it to rebound, producing an outward shockwave that expels a large portion of the star's mass. This event is more luminous, by many orders of magnitude, than our Sun (L $\sim 10^{10} L_{\odot}$). The core that remains after this explosion is a neutron star, a compact dense mass of $\sim$ 1 - 2 $M_{\odot}$ within a radius of $\sim$ 10 km.

A pulsar is a subclass of a neutron star, specifically it is a rotating neutron star. Pulsars are rapidly rotating ($\sim 0.04 - 800$Hz), highly magnetized ($\sim 10^{8} - 10^{15}$ G) neutron stars. The strong magnetic field accelerates charged particles along the magnetic field lines to move at relativistic speeds towards the magnetic pole regions, which then get shot off into space as a collimated beam of emission. If the magnetic axis is inclined with respect to the rotational axis (as in most cases), then every time a magnetic pole sweeps through an observer's line of sight, a radio pulse maybe detected, almost as a lighthouse (see Figure 1.1). Due to their extreme density, their rotational rates are stable, making some of them the Universe's finest natural clocks.

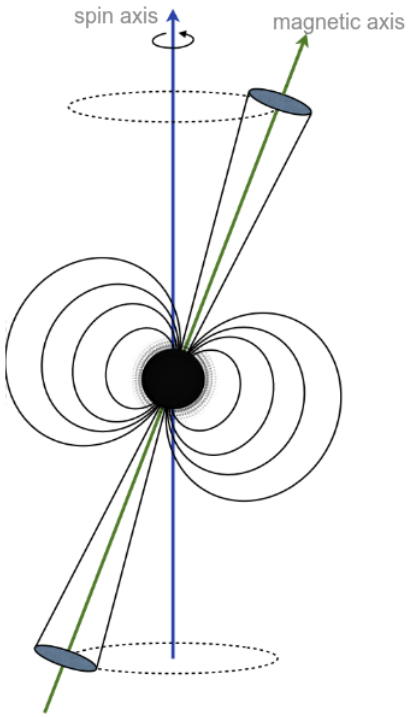

Figure 1.1. This is the simplified pulsar model. The neutron star at the center rotates about its spin axis. This causes the beams of radiation to sweep across the sky like a lighthouse since they are oriented on the magnetic axis, typically misaligned with the spin axis.

1.1.2 Spin-down Energy and Evolution

Even though pulsars have a very stable rotational spin period, their periods gradually increase over time due to the loss of rotational kinetic energy. If the pulsar is undergoing "spin-down", then the rate of change of rotational kinetic energy is known as "spin-down luminosity". This relationship is given by Lorimer & Kramer (2004)

$$\dot{E}_{rot} = -\frac{d(I\Omega^2/2)}{dt} = -I\Omega\dot{\Omega} = 4\pi^2 I\dot{P}P^{-3}, \tag{1.1}$$

where $I = kMR^2$ is the moment of inertia of the pulsar, rotational frequency $\Omega = 2\pi/P$, with the inertia constant, k, the pulsar's mass, M, and radius, R. Despite the internal structure of the neutron star that is not clearly understood it is generally assumed that the moment of inertia is $I = 10^{38}\text{kgm}^2$. This value corresponds to standard dimensions of a pulsar, $M = 1.4\text{M}_\odot$, $R = 10\text{km}$, and $k \simeq 0.4$.

If we consider a pulsar as a rotating dipole magnet, this "spin-down" is expected to follow the rules of classical electrodynamics (Jackson, 1962), which allows us to calculate several interesting characteristic quantities. A rotating dipole with dipole moment $|m|$ emitting an electromagnetic wave at the rotational frequency $\Omega = 2\pi/P$. The release of radiation power is given by,

$$\dot{E}_{dipole} = \frac{2}{3c^3}|m|^2\Omega^4 \sin^2\alpha, \tag{1.2}$$

where α is the angle between the magnetic moment and rotational axis and c is the speed of

light. Assuming that magnetic dipole radiation is the only mechanism for energy loss from the pulsar, and by combining Equation 1.2 and 1.1, it is possible to derive the expected evolution of the rotational frequency as,

$$\dot{\Omega} = -\frac{2|m|^2 \sin^2 \alpha}{3Ic^3}\Omega^3. \tag{1.3}$$

Expressing Equation 1.3 has a general power law form in terms of spin frequency, $\nu = 1/P$, as

$$\dot{\nu} = -K\nu^n \; or \; \dot{P} = -KP^{2-n} \tag{1.4}$$

where n is known as the braking index, and K is a constant. For pure magnetic dipole braking, n is generally considered to be $n = 3$. By further differentiating Equation 1.4, with respect to time and differentiating again to eliminate the constant K, we get:

$$n = \frac{\nu\ddot{\nu}}{\dot{\nu}^2}. \tag{1.5}$$

The braking index can be obtained by only measuring the spin frequency and its first two time derivatives. Even though it is often difficult to measure the second derivative of a pulsar's spin period, due to dominated by either timing noise or it is too small to be measured. There are some cases where it can be measured in young pulsars. These pulsars have a breaking index value range from $n = 0.9(2)$ (Espinoza et al., 2011) to $n = 3.15(3)$ (Archibald et al., 2016), which indicate that the assumption of $n = 3$ might not be correct. Nevertheless, this assumption is used as it allows us to define a number of useful quantities that characterize the basic properties of a radio pulsar.

1.1.3 Characteristic Age

One of the basic properties of a pulsar is its characteristic age, τ_c, which is an estimate of the pulsar's age. By first integrating Equation 1.4, expressed in terms of pulse period, we find:

$$T = \frac{P}{(n-1)\dot{P}}\left[1 - \left(\frac{P_o}{P}\right)^{n-1}\right]. \tag{1.6}$$

The P_o is the initial spin period of the pulsar. Assuming that $P_o \ll P$, and that the spin-down is due to magnetic dipole radiation ($n = 3$), Equation 1.6 then simplifies to:

$$\tau_c = \frac{P}{2\dot{P}}. \tag{1.7}$$

An estimate of a pulsar age can be inferred by using Equation 1.7, with a well measured pulsar's spin period (P) and period derivative ($\dot{P}$).

1.1.4 Characteristic Surface Magnetic Field Strength

Although it is currently not possible to directly measure the magnetic field strength for radio pulsars, it is possible to estimate the strength by assuming that the spin-down process is through dipole braking. The magnetic field strength scales with distance, r, from the magnetic moment as $B \approx |m|/r^3$. By rearranging Equation 1.3, we get

$$B_s = \sqrt{\frac{3c^3}{8\pi^2}\frac{I}{R^6 \sin^2 \alpha}P\dot{P}}. \tag{1.8}$$

Assuming $\alpha = 90°$ and by using previously defined values for I and R, it is possible to derive the expression for the "characteristic magnetic field" as:

$$B_s = 3.2 \times 10^{19} G \sqrt{P\dot{P}}. \tag{1.9}$$

1.2 Effects of the interstellar medium

A pulsar's signal travels through the cold ionized interstellar medium (ISM) before reaching a telescope. The ISM consists mostly of ionized gas at very low densities that can be inhomogeneous and/or turbulent, which in turn affects the radio emission signal from a pulsar. It produces four distinct propagation effects on a pulsar's signal: dispersion, Faraday rotation, scattering and scintillation.

1.2.1 Dispersion

In a perfect vacuum, a broadband pulsar signal would propagate unhindered, traveling at the speed of light, c and all of its frequencies arriving at an observer simultaneously. This is not the case for a signal traveling through the ISM, as its phase velocity is reduced by a frequency dependent factor, called the refractive index μ. As found by the observations of the first radio pulsar by (Hewish et al., 1968), the pulsation arrive earlier at higher frequencies compared to its lower frequency: this is dispersion. Which is expected for a signal when it travels through space consisting of cold plasma (e.g. the ISM). For an electromagnetic wave traveling in this medium, its speed, better known as group velocity, v_g, is given by Lorimer & Kramer (2004),

$$v_g = c\mu = c\sqrt{1 - \left(\frac{f_p}{f}\right)^2}, \tag{1.10}$$

where f is the frequency of the wave and f_p is the plasma frequency. The plasma frequency is defined as

$$f_p = \sqrt{\frac{e^2 n_e}{\pi m_e}} \approx 8.97 \text{ kHz} \sqrt{\frac{n_e}{\text{cm}^{-3}}}, \tag{1.11}$$

where e is the electron charge, n_e is the free electron number density, and m_e is the electron mass. Below this frequency, no radio waves can travel in the medium. From Equation 1.10, considering the case of $f \gg f_p$, the group velocity approaches the speed of light, c. For a pulsar's signals which is broadband, each frequency will have a different group velocity.

By integrating the electron number density along the line of sight to a pulsar, as shown in Lorimer & Kramer (2004), for a path length of l, the time delay is given to first approximation by

$$\Delta t = \frac{e^2}{2\pi m_e c} \frac{\text{DM}}{f^2}, \tag{1.12}$$

where DM is the *dispersion measure* of the pulsar, defined as the electron column density

$$\text{DM} = \int_0^{\text{d}} \text{n}_\text{e} \text{dl}, \tag{1.13}$$

in units of pc cm^{-3}. Filling in the constants in Equation 1.12, we obtain the time delay for the

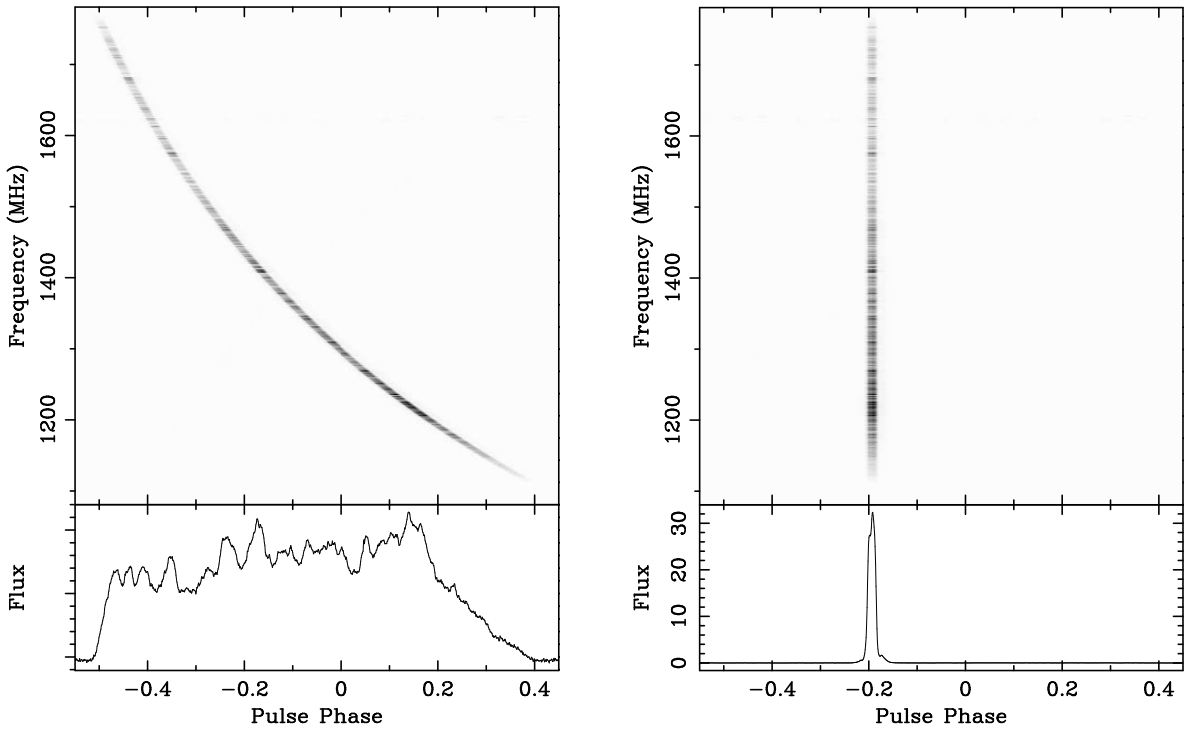

Figure 1.2. Dispersion effect in an example observation of pulsar PSR B1933+16 taken with a broadband receiver centered frequency 1.4 GHz with the Arecibo radio telescope. Left top panel shows the observing band of the pulsar's signal in a characteristic quadratic delay due to the dispersion effect, having a DM of 158.52 pc cm^{-3}. As a result, the bottom panel shows the integrated profile is completely smeared out. The right panel's shows the same observation after dedispersing the signal. The pulsar's signal in all frequency channels are now aligned and the actual integrated pulse profile shape is correctly detected. These data were provided by Alessandro Ridolfi.

arrival of the pulses at $f_{\rm high}$ compared to $f_{\rm low}$

$$\Delta t \simeq 4.15{\times}10^{6}{\rm ms}\left(\frac{1}{{\rm f}^2_{\rm low}}-\frac{1}{{\rm f}^2_{\rm high}}\right)\times {\rm DM}. \tag{1.14}$$

A pulsar signal's can be missed in the noise if one does not dedisperse its signal, as shown in Figure 1.2. Once the DM is known for a pulsar, it is possible to estimate its distance by integrating Equation 1.13 and using a model for the Galactic electron number density, $n_e(l)$, such as the NE2001 Galactic free electron density model by (Cordes & Lazio, 2002) or more recently the YMW16 model by (Yao et al., 2016). It is important to note that the distance estimates provided by these models are considered to have a typical $\sim$ 30% uncertainty, or more. Unfortunately, for the vast majority of pulsars, this is the only method to estimate their distance.

1.2.2 Faraday Rotation

In 1845, Micheal Faraday provided the connection between light and magnetism. He discovered that plane polarized light propagating through matter parallel to a static magnetic field, underwent a systematic rotation of its plane of polarization. This effect is now known as *Faraday*

rotation. Our galaxy has a magnetic field that crosses with the ISM. The free electrons in this field are forced to move in a circular motion due to the Lorentz force, which is perpendicular to the magnetic field direction. The circular motion of the electrons causes two circular polarizations within the light to propagate at two different refractive indices, which result in different velocities. Pulsars are generally highly polarized sources and the propagation of their signal through the magneto-ionized ISM is affected by *Faraday rotation* caused by the magnetic field of the Galaxy.

For an electromagnetic wave with frequency, f, propagating at a distance, d, in a magnetized ionized ISM, the lag in its phase is expressed as (Lorimer & Kramer, 2004):

$$\Delta\Psi = -kd, \tag{1.15}$$

where $k = \frac{2\pi}{\lambda}$ is the wavenumber and λ is the wavelength. For a cold magnetized plasma, the circular polarization state of radiation is expressed with a new refractive index, μ, as:

$$k(f) = \frac{2\pi}{c} f\mu = \frac{2\pi}{c} f\sqrt{1 - \frac{{f_p}^2}{f^2} \mp \frac{{f_p}^2 f_B}{f^3}}, \tag{1.16}$$

where the "$-$" is for a left-handed circular polarized wave, and the "$+$" sign is for a right-handed circular polarized wave. The f_B is called the cyclotron frequency, which contains the dependence of the Galactic magnetic field along the line of sight, $B_\parallel$

$$f_B = \frac{eB_\parallel}{2\pi m_e c}. \tag{1.17}$$

The *Faraday rotation* is the differential phase rotation between the left and right circular polarizations and since $f \gg f_p$ and $f \gg f_B$, we get:

$$\Delta\Psi_{\text{Faraday}} = \int_0^d (k_R - k_L) dl \simeq \frac{e^3}{\pi {m_e}^2 c^2 f^2} \int_0^d n_e B_\parallel dl, \tag{1.18}$$

where k_L and k_R are the wavenumber of the left and right circularly polarized wave. The polarization position angle (PPA), is a periodic on π rather than 2π for phase. The change in PPA can be expressed as,

$$\Delta\Psi_{\text{PPA}} = \frac{\Delta\Psi_{\text{Faraday}}}{2} = \lambda^2 \times \text{RM}, \tag{1.19}$$

where λ is the wavelength, and RM is the *rotation measure*

$$\text{RM} = \frac{\text{e}^3}{2\pi {\text{m}_\text{e}}^2 \text{c}^4} \int_0^\text{d} \text{n}_\text{e} \text{B}_\parallel \text{dl}. \tag{1.20}$$

By measuring the RM and the DM of a pulsar, it is possible to get a measure of the average magnetic field strength in the direction of the line of sight by combining Equations 1.13 and 1.20:

$$\langle B_\parallel \rangle = \frac{\int_0^d n_e B_\parallel dl}{\int_0^d n_e dl} = 1.23\mu\text{G} \left(\frac{\text{RM}}{\text{rad}\,\text{m}^{-2}}\right) \left(\frac{\text{DM}}{\text{cm}^{-3}\,\text{pc}}\right). \tag{1.21}$$

1.2.3 Scattering

The ISM is a inhomogeneous gas that often shows irregularities and turbulence that have a significant impact on a pulsar signal. The effect called scattering is caused by the density irregularities of the local free electron content caused a continuous change in the local refractive index seen by the electromagnetic waves. This then causes the different rays to have multiple non-straight paths from the pulsar to the observers, all of which have extra delays relative to straight path. As a result, the signal may be seen with a "tail" in the observed pulse profile.

The simplest method to describe scattering is called the thin-screen model developed by (Scheuer, 1968). Scheuer (1968) modeled the turbulent ISM as a thin screen of irregularities midway between the pulsar signal and the observer, where this screen is the reason for phase perturbations of the signal, see Figure 1.3. It has been showed in, Lorimer & Kramer (2004) the observed intensity as a function of time as,

$$I(t) \propto e^{-\Delta t/\tau_s}, \tag{1.22}$$

where Δt is the time delay due to the longer optical path and τ_s is a characteristic timescale. The characteristic timescale is related to the observing frequency, f, and the distance to the pulsar, d, that scales as:

$$\tau_s \propto \frac{d^2}{f^4}. \tag{1.23}$$

As a result, the sharp single pulse emitted by the pulsar is seen as a one-sided exponential function to the observer. At low frequencies ($\lesssim$ 1 GHz), the scattering effect is stronger and could cause a pulsar signal to be completely smeared out.

1.2.4 Scintillation

The inhomogeneities of the ISM that cause the scattering of a pulsar's signal can also be responsible for intensity fluctuations of the observed pulsar signal, which is known as *scintillation*. This was first noted by Lyne & Rickett (1968), when they recognized that the distorted wavefronts produce a constructive and destructive interference pattern that will produce a modulated variation of the detected intensities of the source. This interference can only occur if the phases of the waves are no different by more than 1 radian, which means that there is a limiting bandwidth, Δv, called *scintillation bandwidth*. It has been shown, (e.g. Lorimer & Kramer, 2004), that the condition of interference is:

$$2\pi\Delta v\tau_s \sim 1. \tag{1.24}$$

From Equation 1.23, the scaling of the bandwidth to the timescale is $\Delta v \propto 1/\tau_s \propto v^4$, which shows that scintillation produces a pattern of intensity variation in both time and frequency. This can cause a pulsar's signal to be seen as faint or strong at different times of an observations and is generally referred to as diffractive interstellar scintillation. In addition to diffractive scintillation effects, larger scale inhomogeneities in the ISM can refract the propagating signal, causing long timescale flux density variations known as refractive interstellar scintillation (Rickett et al., 1984).

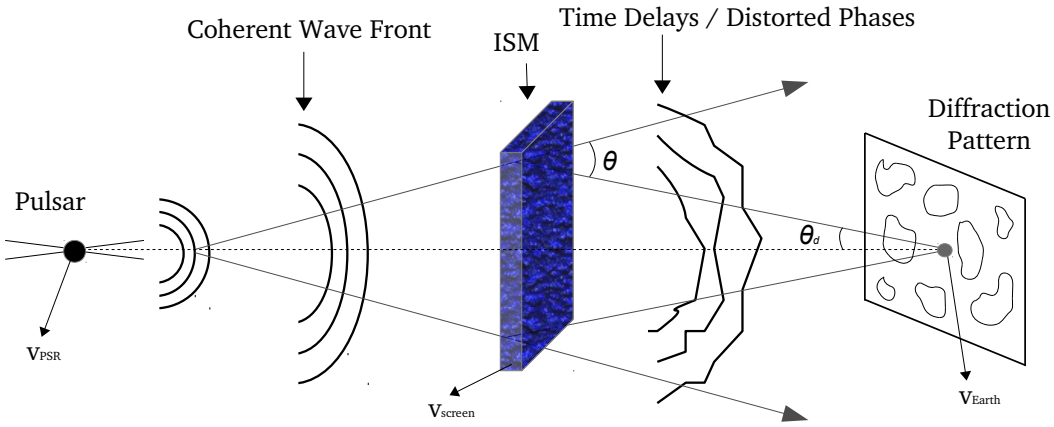

Figure 1.3. This thin-screen model shows the inhomogeneities in the ISM that results in observed scattering and scintillation effects. The pulsar signal is initially a coherent electromagnetic wave that is later distorted by a thin screen of irregularities of the ISM. The resulting randomly distorted waves have a multi-path propagation towards the observer that forms the scattering effect. Scintillation is produced by randomly distorted wavefronts that form an interference pattern that can be observed as intensity fluctuations.

1.3 Pulsar Population

As of today, according to the most extensive pulsar catalog, the ATNF Pulsar Catalog (version 1.57, (Manchester et al., 2005), there are 2,627 known pulsars. The majority of them have been discovered in radio, with a growing population that is observed at higher frequencies (e.g. Gamma, X-ray). As most pulsar properties can be inferred from the spin period and its derivative, a common representation of the pulsar population is a plot of P versus $\dot{P}$ diagram. These two quantities are evolve and change with the pulsar's age, and if the pulsar is in a binary interaction. The $P-\dot{P}$ diagram for the current known pulsar population is shown in Figure 1.4. There are two main distinct groups in the pulsar population: normal "slow spinning" pulsars and recycled "highly rapidly spinning" pulsars

1.3.1 Young Pulsars

The discovery of the pulsar in the Crab Nebula was the first substantial clue in deciphering the birth of neutron stars. Many more pulsars have since been discovered to be associated with recent supernova remnants. These pulsars have small characteristic ages ($\tau_c \lesssim 100$ kyr) and are the light blue pentagon points located in the top of the $P-\dot{P}$ diagram in Figure 1.4.

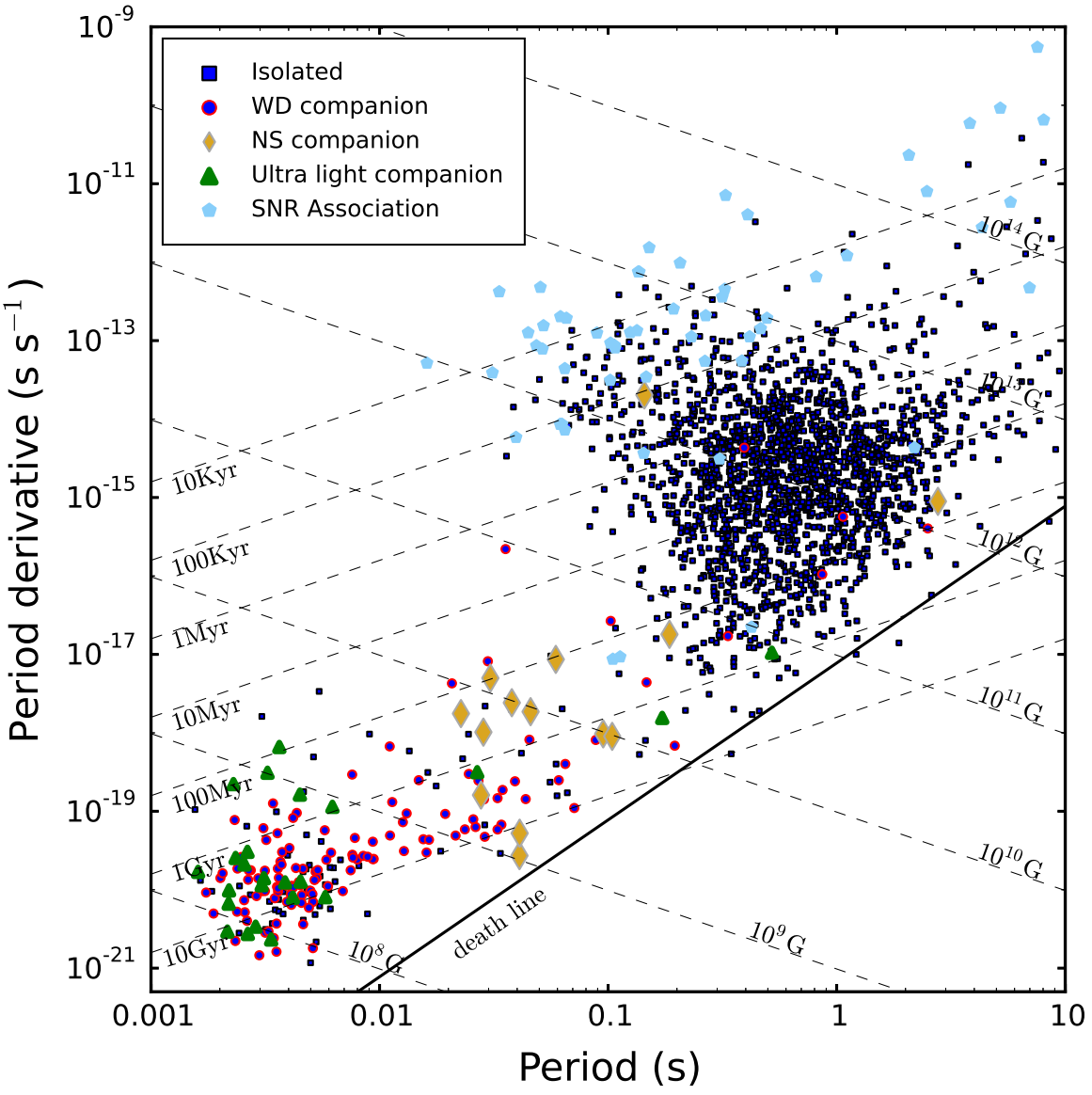

Figure 1.4. The spin period vs spin period derivative ($P - \dot{P}$) diagram for the currently 2627 known pulsars.

1.3.2 Normal Pulsars

"Normal" pulsars are shown in black points towards the top right of the $P-\dot{P}$ diagram, in Figure 1.4, they are the majority of the pulsar population. They have a spin period of $P \sim 0.1 - 10$s and a strong magnetic field of $B_s \sim 10^{10} - 10^{13}$ G. They come from a continuous evolution from the "young" pulsars. If these "normal" pulsars do not have any strong interaction with another celestial body, they continue to spin-down until they cross the death line in the $P-\dot{P}$ diagram. At this stage, the spin-down is so low that its magnetic field is no longer strong enough to maintain the mechanism that produces the radio emission active and the pulsar becomes undetectable (Chen & Ruderman, 1993).

1.3.3 Recycled Pulsars

Towards the lower left corner of the $P - \dot{P}$ diagram, there is a clearly separate population of pulsars with small spin periods and spin-downs compared to the normal and young pulsars population. These are known as recycled pulsars, and they have spin periods of $\sim 1 - 180$ ms and smaller magnetic field strength of $\sim 10^9 - 10^{11}$ G. Recycled pulsars represent the last phase of stellar evolution in close, interacting binary systems. Their observed orbital and astronomical properties are records of their evolutionary history (Bhattacharya & van den Heuvel, 1991; Tauris et al., 2011, 2012). They are generally the first formed neutron star in the binary system, which was spun up to a fast spin period via accretion of mass and angular momentum from the evolving secondary star (Alpar et al., 1982; Bhattacharya & van den Heuvel, 1991). In this process it loses magnetic field strength. This stage is seen as an X-ray binary (Archibald et al., 2009; Podsiadlowski et al., 2002; Tauris & van den Heuvel, 2006). Once accretion stops we observe a radio, slightly more massive, pulsar rotating to a much faster spin period and small spin period derivative (Radhakrishnan & Srinivasan, 1982). Over the last decades, the number of known recycled pulsars has reached more than 310 (Manchester et al., 2005), of which about 283 are in binaries. The remaining are isolated recycled pulsars that have either evaporated their companion (Fruchter et al., 1988), ran away in a the supernova explosion (Tauris & Takens, 1998), or lost it in an exchange encounter in a globular cluster (Freire et al., 2012; Verbunt & Freire, 2014).

Although all recycled pulsars share the features mentioned above, they are additionally divided into sub-classes. Of which the millisecond and mildly recycled pulsars is the most relevant subject for this thesis.

1.3.3.1 Millisecond Pulsars

Millisecond pulsars (MSPs) are defined by their exceedingly fast spin periods ($P \sim 1 \lesssim 20$ms) and magnetic fields strength of $\sim 10^8$ G. The first MSP PSR B1937+21, was discovered in 1982, a few degrees away from the first discovered pulsar (Backer et al., 1982). This pulsar has a spin period of 1.55ms, and for over 20 years it was the fastest spinning pulsar know. Now the record holder is PSR J1748−2446ad with a spin period of 1.39ms (Hessels et al., 2006).

The standard formation scenario for MSPs starts in a binary system consisting of a low mass ($\sim 1M_\odot$) star orbiting a higher mass ($\sim 8 - 10M_\odot$) star. The massive star will first evolve to become a pulsar, following the lifecycle as described in Section 1.1.1. If the binary system survives the supernova caused by the high mass star, the system will then consist of a pulsar and a low-mass companion. As the low mass companion slowly evolves along the main sequence into its red giant phase, it will expand and fill its Roche lobe (its outer layers become gravitationally

unbound from its core). Then a long accretion episode starts and may be seen as a low-mass X-ray binary, in some cases alternating with the radio stage (Archibald et al., 2009; Tauris & van den Heuvel, 2006). This recycling process results in the pulsar spin period reaching ultra fast rotational spin periods (a few milliseconds (Bhattacharya & van den Heuvel, 1991; Podsiadlowski et al., 2002)) and very low magnetic field strengths. Due to the long accretion episode, MSPs are found in the bottom left corner of the $P - \dot{P}$ diagram. The system generally then stabilizes as an MSP in an almost circular orbit with the remnant of the low-mass secondary companion, generally a He WD.

Because MSPs have a high angular momentum, they have extremely stable spin periods, making them extraordinary natural clocks. Due to this characteristic, a major effort is taking place to use an array of brightest MSPs across the sky to detect gravitational waves in the nanohertz regime. This Galaxy-sized detector is known as pulsar timing array (PTA) (e.g. Foster & Backer, 1990; Jenet et al., 2005; Verbiest et al., 2016). MSPs have also been used to measure independent masses of the planets within our Solar System (Champion et al., 2010), and, one day, could be instrumental in future spacecraft navigation systems as a galactic positioning system. How MSPs are used in this thesis, is that if the MSP is in a binary system, it allows for precise astronomical parameters of the pulsar and binary parameters, and most importantly (a possibility) their individual mass measurements (see Chapter 2).

1.3.3.2 Mildly Recycled Pulsars

If the initial binary is an intermediate or high mass binary systems, then it will evolve as a high-mass X-ray binary. The fast evolution of the companion star will imply a short accretion phase. Subsequently, the pulsar is then only partially spun-up, becoming a mildly recycled pulsar (MRP), with a spin period range of $\sim 20 - 200$ ms. Also because of a short accretion phase, the magnetic field strength of an MRP is between $\sim 10^9 - 10^{11}$ G, i.e., not as low as for MSPs.

If the companion is an intermediate mass ($\lesssim 8M_\odot$), it can end its life by ejecting its outer layers and leaving behind a massive carbon-oxygen white dwarf (CO WD) or oxygen-neon-magnesium white dwarf (ONeMg WD) companion (Tauris et al., 2000, 2011, 2012). These binary systems are characterized by low orbital eccentricities.

If the companion is a high mass ($\gtrsim 10M_\odot$) (Tauris & van den Heuvel, 2006) star and goes supernova, and if the binary system survives a second supernova explosion, the companion becomes second neutron star. This system is called a *double neutron star* (DNS) system, which is a rare system where two massive stars were bound for life and, even after death, they are still orbiting each other in an almost never ending eccentric cyclic dance. These systems are characterized by large eccentricity, caused by the second supernova explosion, with one older neutron star (a mildly recycled pulsar) orbiting a young neutron star (a normal slow pulsar). The discovery of these DNS systems has given pulsar astronomy some of its most monumental results. The discovery of the first DNS, B1913+16, the Hulse-Taylor pulsar (Hulse & Taylor, 1975) was awarded the Nobel Prize in Physics for measuring of the systems orbital decay due to the emission of gravitational waves as predicted by Albert Einstein's theory of General Relativity (GR). This was the first indirect detection of gravitational waves (GWs), and paved the way for the hunt for a direct detection of GWs. The first direct detection occurred in 2015, and that has recently now opened a new window of astronomy (Abbott et al., 2016). DNS systems are fantastic natural laboratory for tests of GR. This is extraordinary precision is especially true for the only double pulsar system, J0737-3039A/B (Burgay et al., 2003) & (Lyne et al.,

2004), a system in which both neutron stars are pulsars with their beams of radiation seen from Earth. This system provides one of the best available tests of GR with up to 0.05% precision and alternative theories of gravity in the strong-field regime (Kramer et al., 2006).

1.4 Pulsar Research

Pulsars have incredibly stable spin periods, especially the recycled pulsars, and this makes them ideal probes of a wide variety of astrophysical phenomena. They have been used to detect the first exoplants (Wolszczan & Frail, 1992), to test the accuracy of gravitational theories (Taylor & Weisberg, 1982; Kramer et al., 2006; Freire et al., 2012), and for the ongoing effort to detect low frequency gravitational waves using PTAs (Jenet et al., 2005; Verbiest et al., 2016). They also provide a window into stellar and binary evolution (Lorimer, 2008), assist in mapping the Galactic magnetic field on large scales (Han et al., 2018), and last but not least, determining an equation of state (EoS) for ultra-dense matter. The combination of massive neutron mass and tighter radius measurements of neutron stars lead to constraints of the properties of the EoS for ultra-dense matter, densities higher than that of the atomic nucleus (e.g. Özel & Freire, 2016). Pulsar astronomy has contributed to many areas of fundamental physics, and will keep going as more discoveries and sensitive telescopes are made in the future.

The key ingredient of so many successful pulsar studies is the incredible stability of the rotation of these neutron stars and the high accuracy we achieve in measuring the times of arrival of the pulses. After observing a pulsar regularly for a year or more, we can construct, in most cases, a close to accurate model of the pulsar system that is capable of keeping track of every single rotation of the pulsar. This technique of pulsar monitoring with high precision is called *pulsar timing* (see Chapter 2). We now highlight one of these applications.

1.4.1 Neutron Star Mass Measurements and Constraints on the Equation of State of Ultra Dense Matter

Neutron stars contain matter in one of the densest forms found in the Universe with central densities higher of an atomic nuclei. Our understanding of the composition and properties of cold nuclear matter at high densities is an unsolved problem in modern physics. With the observations and measurements of neutron star masses and their radius a mass versus radius relation has placed strong constraints on the EoS of dense matter. Precise mass measurements has resulted largely from radio observations of pulsars, while the radius measurements have been from X-ray observations of neutron stars in low mass X-ray binaries (LMXBs). Pulsar masses are only measured (at the moment) from binary systems, with the precise tracking of the orbital motions through pulsar timing (see Chapter 2), while neutron star radius measurements methods all rely on spectroscopy to detect thermal emission from the surface of the neutron star.

At the time of writing this thesis, we know of ∼32 precise neutron star masses spanning the range from 1.17 to $2.0 M_\odot$ (see Figure 1.5) and about a dozen neutron star radii measured from 10-11.5 km range (Özel & Freire, 2016). The heaviest neutron star known is J0348+0432 with a mass of $2.01 \pm 0.04 M_\odot$, and using this pulsar, scientists have ruled out many EoSs that have a maximum mass that fall below it (Antoniadis et al., 2013). The lightest precisely measured neutron star mass is $1.17 M_\odot$, which is a work done in this thesis, see Chapter 3. Pulsar astronomy has been pushing the limits on the EoS of ultra-dense matter. But with the

combined efforts of masses and radii measurements, one day this problem will be solved (see Figure 1.6 for how far we have come so far)

1.5 Thesis outline

The work of this thesis consists of current efforts to discover new pulsar systems with both the 305-m Arecibo Observatory and the 100-m Effelsberg radio telescope pulsar surveys. This thesis also presents the work on the scientific explorations of the pulsars discovered in the Arecibo survey, two new double neutron star systems, and other six recycled pulsars. The methods and techniques of pulsar searching and timing will be described in the following chapters.

- In **Chapter 2** we examine the techniques and methods of pulsar searching and timing.
- In **Chapter 3** we present "*Pulsar J0453+1559: A Double Neutron Star System with a Large Mass Asymmetry*", a new DNS system discovered and followed up with the Arecibo Observatory.
- In **Chapter 4** we present "*Pulsar J1411+2551: A Low Mass Double Neutron Star System*", a new DNS system discovered and followed up with the Arecibo Observatory.
- In **Chapter 5** we present "*The Discovery of Six Recycled Pulsars from Arecibo 327-MHz Drift-Scan Pulsar Survey*", five of which are in a binary system and the other one is an isolated MSPs, discovered and followed up with the Arecibo Observatory.
- In **Chapter 6** we present conclusion and future research plans.

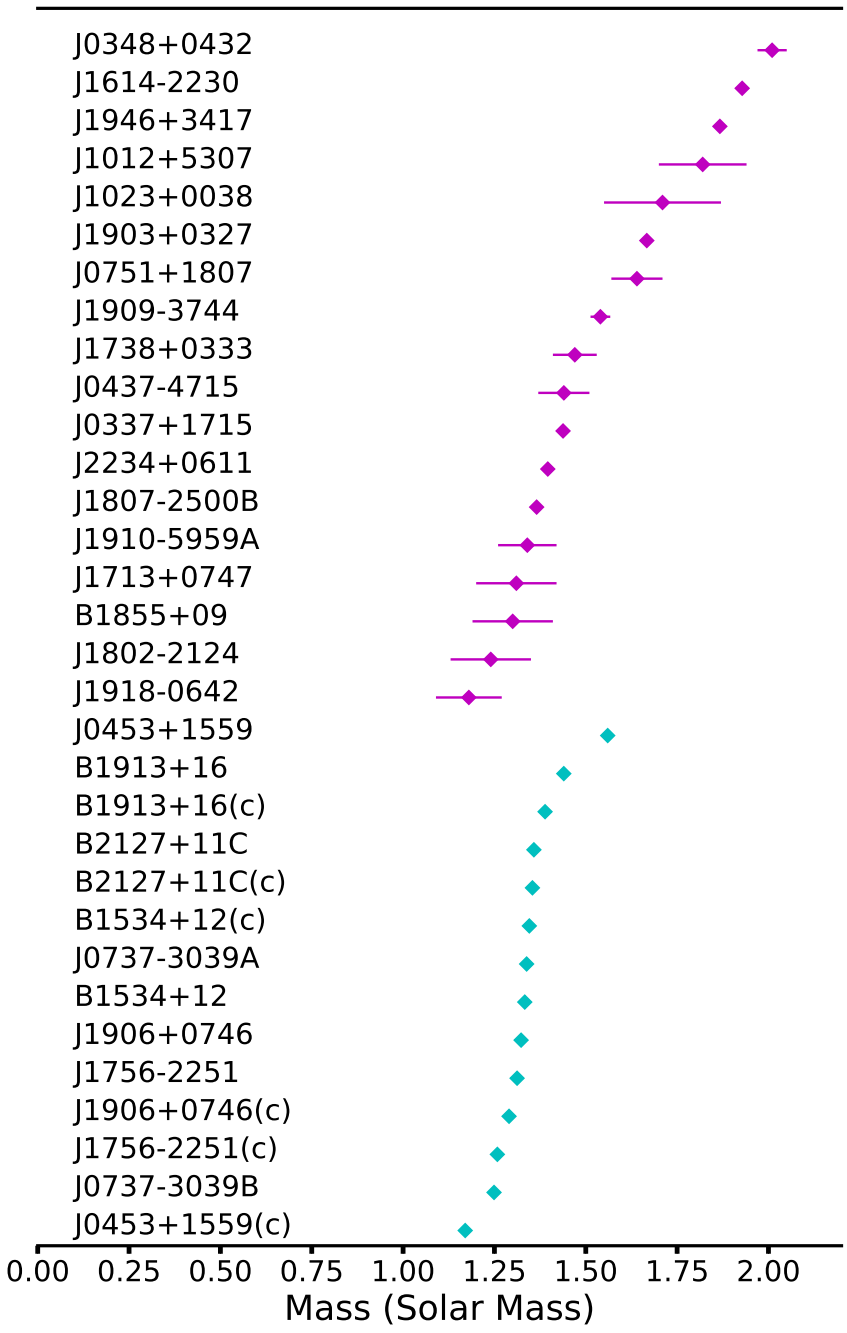

Figure 1.5. This figure shows the all the current masses measurements from pulsars. The magenta points are recycled pulsars, while the cyan points are DNS systems. This figure was provided by John Antoniadis.

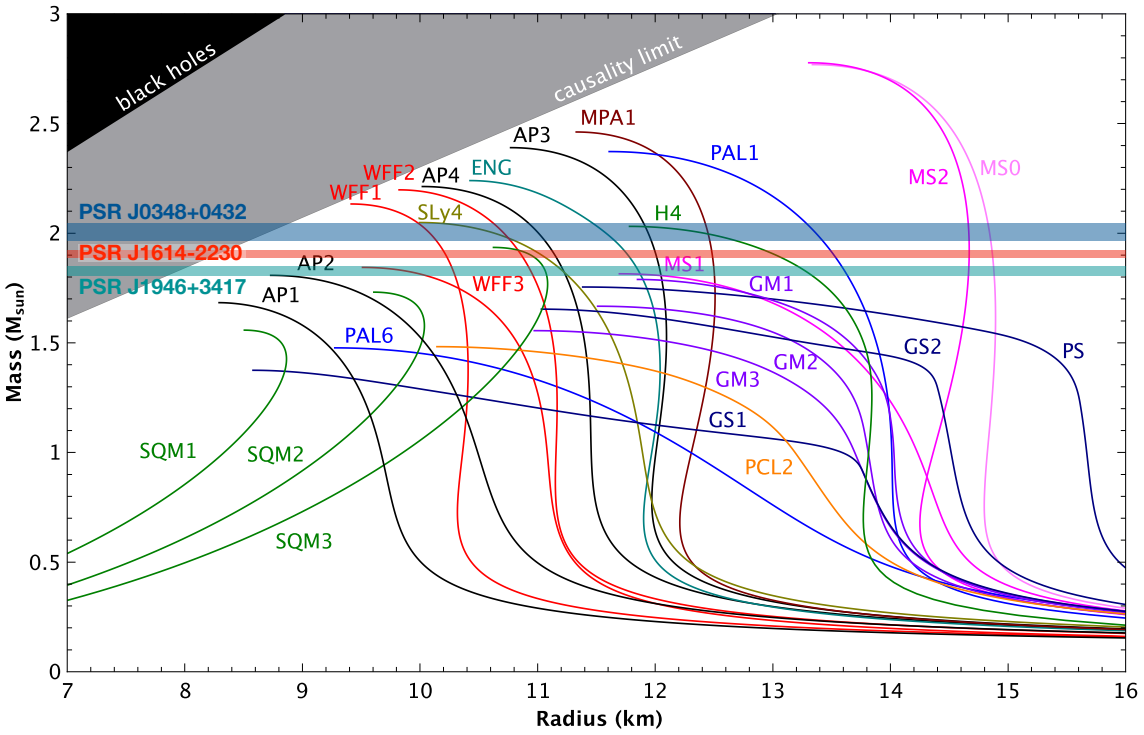

Figure 1.6. This figure shows the different EoS, which have a relation between mass and radius for all neutron stars indicated by its curve and also shows the impact of high mass neutron star measurements. Figure created by Norbert Wex and EoSs from (Lattimer & Prakash, 2001).

Chapter 2

Pulsar Searching and Timing Methods

This chapter gives an overview of pulsar searching and timing techniques, which are the fundamental pillars of pulsar astronomy. Pulsar searching has always had a significant role because as the number of new discoveries rises, so does the understanding of pulsar population and of characteristics of each system. Most of our understanding of individual sources come from pulsar timing. The continual search for new pulsars and their exploitation has led to, and could continue to contribute to, discoveries in astrophysics, stellar evolution, fundamental physics, gravity, and nuclear physics.

Contents

2.1 Pulsar Searching

The search for radio pulsars can be done in two forms: blind searches and targeted searches.

Pulsars are weak radio sources, with observed flux densities in the Jy to μJy range (Manchester et al., 2005). A blind search consists of uniformly surveying a large area of the sky with a radio telescope that have large collecting areas. Some notable large-scale surveys are the Parkes Multibeam Pulsar Survey (PMPS) (Manchester et al., 2001), which has discovered over ∼1000 pulsars; the Pulsar Arecibo L-band Feed Array (PALFA) searching for pulsars in the Galactic plane within Arecibo field of view (Cordes et al., 2006) discovering 188 pulsars and counting. Other successful surveys are the Arecibo 327 MHz Drift Pulsar survey (AO327) searching for pulsars and radio transient signals in the entire visible sky of the Arecibo Observatory (Deneva et al., 2013), which we will mention in more detail in thesis; the Green Bank Northern Celestial Cap Pulsar Survey searching for pulsars and radio transients signals in the entire sky visible of the Green Bank Telescope declination range of -46° to 90° (Stovall et al., 2014); and the High Time Resolution Universe North/South (HTRU-N/S) which uses the Parkes Radio Telescope in Australia and the Effelsberg Radio Telescope in Germany, searching for pulsars in the entire sky (Keith et al., 2010; Barr et al., 2013b). Every single pointing from these large-scale surveys is searched deeply for potential pulsars, across a broad range of parameters; since an undiscovered pulsar's parameters (e.g. position, spin period, DM and acceleration) are not known. These searches are computationally intensive, but over past decades, many instrumental and computational advancements have been made to allow modern pulsar searches to explore the sky at a much faster rate than before. Blind searches have been responsible for about ∼85% of our known pulsars population (Manchester et al., 2005).

The other ∼15% of the known pulsar population were discovered through targeted searches. This type of search involves a telescope being pointed at a specific region of the sky, a region where one or more pulsars are highly likely to exist. These targeted regions can be globular clusters (GC) (Lyne et al., 1987; Camilo & Rasio, 2005; Ransom, 2008; Freire, 2013), supernova remnants (Manchester, 1988; Lorimer et al., 1998), γ-ray point sources (Ransom et al., 2011; Cognard et al., 2011; Barr et al., 2013a), or binary WDs detected in optical (Athanasiadis in prep.). All of these regions provide some prior knowledge about the potential source (e.g. position, DM, and acceleration range) and have properties that usually indicate potential pulsars may be discovered. In the case of GC, which are a self gravitating group of stars with extreme high stellar densities, they have a known position and DM. By having both position and DM, this information can help aid to search for more pulsars in the GC. The fastest spinning pulsar, as of now, was discovered in a GC; the 716-Hz pulsar J1748-2446ad was discovered in Terzan 5 (Hessels et al., 2006).

Although the majority of pulsars are found in radio, their emission is not limited to these wavelengths. The Fermi Gamma-ray Space Telescope detected over 1000 γ-ray sources that were thought to host a neutron star. Most of these sources were followed up with radio and γ-ray telescopes, which led to the discovery of 234 pulsars[1]. A 100 of the pulsars are radio millisecond pulsars, which greatly increased the known MSP population (Ray et al., 2012).

In this thesis, we will only focus on blind large-scale pulsar searches done with the Arecibo and Effelsberg Radio Telescopes. Such a procedure is shown in Figure 2.1, a standard pulsar searching pipeline used for this thesis. There are seven key steps in searching for radio pulsars, all of which are summarized in this work:

[1] https://confluence.slac.stanford.edu/display/GLAMCOG/Public+List+of+LAT-Detected+Gamma-Ray+Pulsars

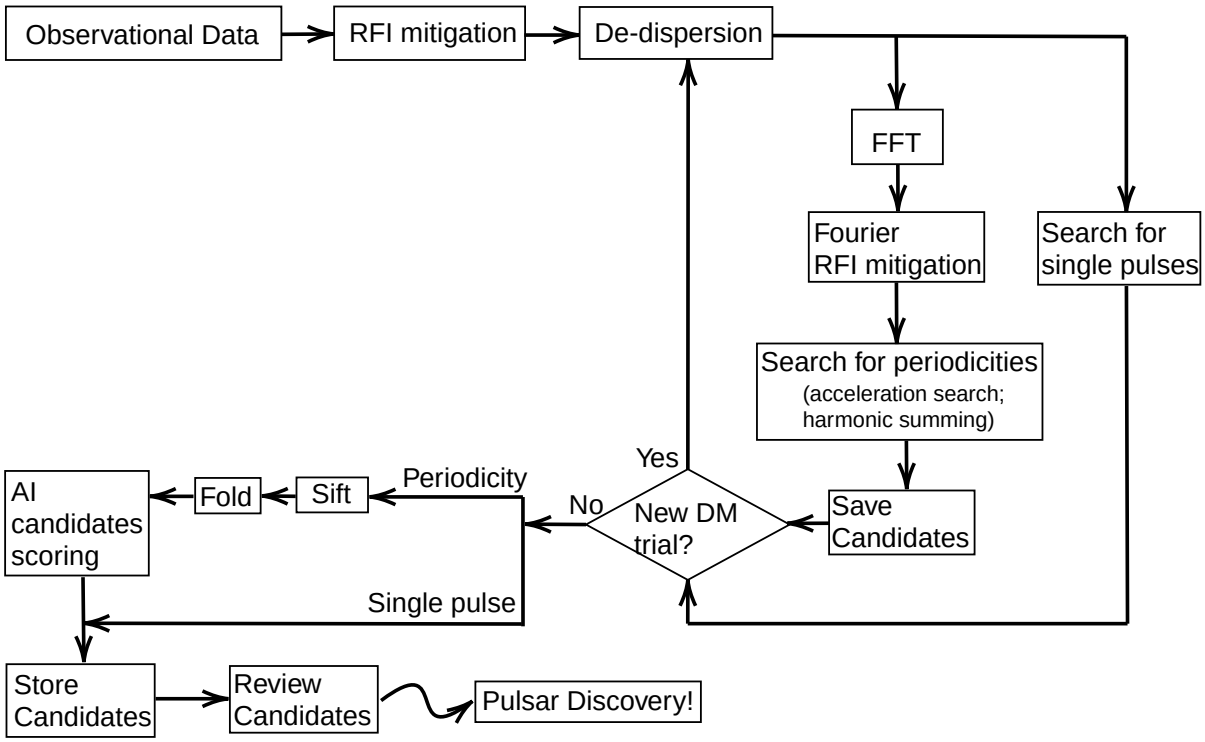

Figure 2.1. This is representation of a standard pulsar searching pipeline, showing the flow for processing a single observation.

1. Data acquisition
2. Removing radio frequency interference
3. Removing the effects of the ISM
4. Searching for periodic signals
5. Searching for single pulse signals
6. Identifying best candidates
7. Confirming candidates

We discuss each of these points in the following.

2.1.1 Data acquisition

The first pulsars were discovered by visual inspection of the total power output from a radio telescope (Hewish et al., 1968), but only a small fraction of pulsars are actually strong enough to be detected in this way. In order to maximize sensitivity, radio pulsar observations require telescopes to have large collecting areas, large observing bandwidths, and additionally high time and frequency resolution recording systems. A large observing bandwidth contributes to the search sensitivity and also distinguish a pulsar signal from radio frequency interference (RFI, see Section 2.1.2). Another complimentary way to increase sensitivity is to expand the integration time of an observation. However, this will require longer computationally effort for each pointing and extend the searching process. A balance must be meet between these two. The high time

resolution (∼50–100μs) is needed for searching for the fastest rotating pulsars, and the high frequency resolution (∼10–600kHz) is necessary to correct for dispersive smearing effects caused by the ISM (as mentioned in Section 1.2.1).

Modern observing systems can be divided into four main parts:

- The dish of the radio telescope that collects and focuses the incoming radio frequency (RF) signal at the primary or secondary focus.
- The *front-end*, also known as the *receiver*, is where the collected incoming RF signals get observed and amplified.
- The *down-conversion* takes the RF signal through a *mixer*, in order to down convert the signal to reduce cable transmission losses of the signal.
- The *back-end* is a combination of hardware and software responsible for the digitization of the RF signal, to be later used for further processing and final storage.

The RF signal goes through the *front-end*, where a feed horn channels it into the receiver and then converted to electric voltages separated into two orthogonal (linear or circular) polarization. The signal is then amplified with a Low-Noise Amplifier (LNA), which is cryogenically cooled to minimize the impact of thermal noise from the electronics of the receiver. This step is very important, as the additional noise at this point could have a large impact on the receiver's sensitivity. After the LNA, the RF signal continues to be filtered as it goes through a bandpass filter which removes unwanted frequencies outside the band of interest. After the filtering, additional amplification is done.

At this point in the signal path, the RF signal passes through a *mixer* in order to *down-convert* it to a lower intermediate frequency (IF) to reduce the cable transmission losses of the signal which are more prominent at higher frequencies. This is done by using the Local-Oscillator (LO), which produces a monochromatic sinusoidal wave of fixed frequency ν_{LO} for each polarizations. The RF signal is then taken by a mixer and multiplied by the LO wave. This mixing process produces a resulting IF at $\nu_{IF} = \nu_{RF} \pm \nu_{LO}$, which is then passed through another bandpass filter where only the signal at lower or high frequency is retained. Additional amplifiers are then used to achieve a stable amplification before transmitting it to the back-end.

The *back-end* is the end of the signal chain that is responsible for the signal to be digitized, processed, and stored. The sampling conversion of the IF signal into digital format is done by Analog-to-Digital converter (ADC), which has a sampling rate of twice the inverse of the observing bandwidth set by the Nyquist-Shannon theorem (Nyquist, 1928; Shannon, 1949). Then, for pulsar searching purposes, the digitized signal is processed by a polyphase filterbank (PFB) that splits the observing bandwidth into various frequency channels and lead to a type of observing mode called *incoherent dedispersion mode*. This mode allows for the individual frequency channels to be realigned to compensate for the effects of pulse dispersion. In the case of pulsar timing (see Section 2.2), for a pulsar whose parameters have been previously determined, this data can be processed in real time through an observing mode called *coherent dedispersion mode*. This mode is a powerful technique which completely eliminates the effects of dispersive smearing on pulsar profiles using its DM and resolves features of the pulse profile. This greatly increasing the precision of pulsar timing observations. This was first developed by Hankins & Rickett (1975), which requires access to the raw IF voltages as produced by the telescope frontend. It involves mixing the IF signal with a secondary LO, where it produces two mixed signals. The second signal having been mixed with the same LO signal, but with an

applied shift of 90°. Then combining these two signals allows for the digital sampling through additional ADC, which retain both the amplitude and phase of the original IF voltages. Then *coherent dedispersion mode* can be achieved by applying an inverse ISM transfer function to the voltages, where the transfer function being specific to the DM of the pulsar being observed.

2.1.1.1 Pulsar Survey Projects

The work from this thesis comes from the AO327 and HTRU-N surveys. I led the proposal writing for request of telescope time, observations and process of data searching for pulsars in the HTRU-N survey. I led discoveries and their follow-up of new recycled pulsars from the AO327 survey, resulting in two new double neutron star systems (Chapter 3 and 4) and six new recycled pulsars (Chapter 5). The following are brief descriptions of the surveys parameters.

The A0327 is a drift scan survey, where the telescope is parked at a fixed azimuth to survey the sky as it drifts through the stationary telescope beam at the sidereal rate. This survey uses the Arecibo 305-m single-dish radio telescope and has been ongoing since 2010. It takes data during the Arecibo telescope downtime, or unassigned time, and aims to search the entire Arecibo field of view (declination from $-1°$ to $38°$) for pulsars. This survey uses Arecibo's 327 MHz receiver that records data at a center frequency of 319 MHz with a bandwidth of 68 MHz that is split into 1024 channels with a time resolution of 125 μs. The drift scan pointings have an integration time of 60 s, which is the sidereal rate where a source passes along the full size of the beam of 15 arcminutes (Deneva et al., 2013).

The HTRU-N survey is the first major pulsar survey conducted with the Effelsberg 100-m single-dish radio telescope. It uses a 7-beam receiver system and it is the first L-band (center frequency at 1.36 GHz) survey of all northern sky (declination $\geq -31°$). This survey has a bandwidth of 240 MHz that is split into 512 channels with a time resolution of 54 μs. The survey is divided into three parts, that correspond to three ranges of Galactic latitude, each with a different integration time. The high latitude section covers the sky at Galactic latitude of $|b| > 15°$ with a short integration time of 90 s, the reason for a short integration time is because this section has been unsurveyed at high frequencies and many bright new radio pulsars are expected to be found. The mid-latitude section covers Galactic latitudes of $|b| < 15°$ and has an integration time of 180 s. The longer integration time is needed due to the mid-latitude section is the most populated region for pulsars in the Galaxy. Lastly, the low latitude section covers Galactic latitudes of $|b| < 3.5°$ with even longer integration time of 1500 s. The large integration times make this the deepest survey of the Galactic plane as seen from the Northern hemisphere, which is expected to house many faint pulsars (Barr et al., 2013b).

2.1.1.2 Pulsar Software

As of today, there are two main software packages that are used to search for radio pulsars; `PRESTO`[2] (Ransom, 2001) and `SIGPROC`[3] (Lorimer, 2011). In this chapter, since both pulsar searching pipelines for the Arecibo and Effelsberg surveys are `PRESTO` based, I will describe a `PRESTO` based pipeline.

[2] https://www.cv.nrao.edu/ sransom/presto/
[3] http://sigproc.sourceforge.net/

2.1.2 Radio Frequency Interference Mitigation (RFI)

A radio astronomer's worst enemy is radio frequency interference, known as RFI. RFI is unwanted non-astrophysical signals, which can hinder the quality of the data. The origins of these signals are from the advancement of telecommunication devices and electronics, such as communication satellites, mobile phones, wireless modems, bluetooth devices, to name just a few. Pulsar signals can be buried in RFI (see Figure 2.2). For this reason, it is a crucial to first mitigate RFI in the pulsar search data.

Unlike pulsar signals that travel long distances and are dispersed, significant amount of RFI signals have terrestrial origins. These signals are not dispersed by the ISM and therefore have a DM of 0 $\mathrm{pc\,cm^{-3}}$, which allows the separation of pulsar signals and RFI. One can then integrate all time samples across the observing bandwidth to obtain a time series at a DM of zero. Then perform a statistical analysis on this time series to identify signals generated by strong impulsive RFI to be clipped off in the data, this method is known as *zero-DM filtering*. Another useful tool in the pulsar data analysis software `PRESTO` called `rfifind`. This program analyses the pulsar search data in blocks, calculates statistics, and by comparing the data with the statistics; it creates a mask file to be used to remove the RFI in the data by replacing bad channels with median values of the data. This tool was used in both Arecibo and Effelsberg pulsar searching pipelines.

2.1.3 Dedispersion trials

Once the data has been cleaned of RFI, the next step in the pulsar searching pipeline is the removal of the dispersive delays caused by the ISM in each frequency channel. As described in Section 1.2.1, the broadband emission from pulsars is effected by dispersion as it travels through the ISM from the source to the telescope. If not corrected, a pulsar signal could be undetectable. When searching for new pulsars in a blind search, the DM is not known, therefore, many possible DM values are searched. Both Arecibo and Effelsberg pulsar searching pipelines search from a DM range of 0 to 2000 $\mathrm{pc\,cm^{-3}}$. For each DM trial, the frequency channels of the observation are shifted according to Equation 1.14 and then summed to produce a dedispersed time series. Each dedispersed time series is then searched for possible pulsar signals as in Section 2.1.4.

An optimal dedispersion plan must be made first in order to efficiently use computational time to process each observation. The most important parameter to determine is a DM step size, ΔDM. A small step size could lead to an increase in computational time without gaining sensitivity, and a large step size could have a pulsar signal to be smeared out and become undetectable. The optimal ΔDM depends on the observing frequency ν, total bandwidth $\Delta\nu$ and sampling time t_{samp}. In Lorimer & Kramer (2004), an approximate formula to calculate the ΔDM value as a function of observation parameters:

$$\Delta\mathrm{DM} = 1.205 \times 10^{-7}\, t_{\mathrm{samp}} \left(\frac{\nu^3}{\Delta\nu}\right) \mathrm{pc\ cm^{-3}} \tag{2.1}$$

where t_{samp} is in ms and ν and $\Delta\nu$ are in MHz.

The Arecibo and Effelsberg pulsar search pipelines use `PRESTO` pulsar software package, which has a useful tool called `DDplan.py`. This tool uses the observational parameters such as observing frequency, total bandwidth, number of channels and sampling time to calculate the smearing time for a range of DM. It then uses this information to calculate an optimal ΔDM and a downsampling factor given by the dispersion intra channels. Once a plan is obtained then

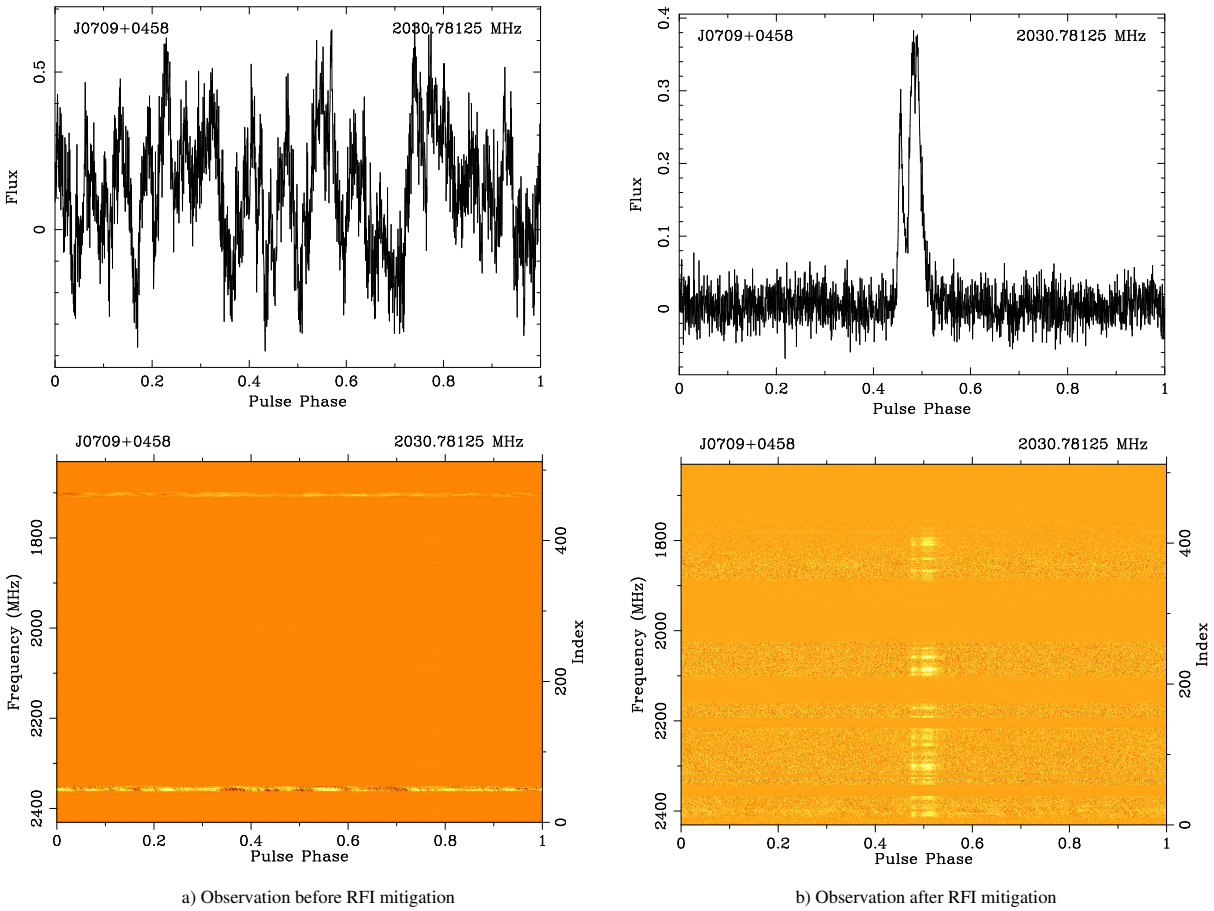

Figure 2.2. These plots are from the same observation of PSR J0709+0458, taken at 2030 MHz with the Arecibo Observatory. The top panels show the integrated pulse profile, after summing all the frequency channels and the bottom panels show the intensity as a function of observing frequency vs pulse phase. The left two panels show how prominent RFI can affect a pulsar signal if not cleaned. The right two panels show the same observation after being cleaned from RFI, where we can now clearly see the pulsar signal.

the pipeline will generate all the individual dedispersed time series for each of the DM in the dedispersion plan that will later be searched for possible pulsar signals.

2.1.4 Searching for Periodic Signals

The next step after dedispersion is to search for possible unknown spin periods of a pulsar. The most common method to search for periodic signals is by using Fourier Transform (FT):

$$F(\nu) = \int_{-\infty}^{\infty} f(t) e^{(-i2\pi\nu t)} dt. \tag{2.2}$$

Since the dedisperse time series generated in pulsar search data is a discrete uniformly sampled and finite data set. We must use the Discrete Fourier Transform (DFT) to convert the time series from time domain to Fourier domain.

For a time series, $\mathcal{T}_k$, the value of the j^{th} bin of its DFT is defined from Press et al. (1992):

$$\mathcal{F}_j = \frac{1}{N} \sum_{k=0}^{N-1} \mathcal{T}_k e^{\frac{-i2\pi jk}{N}} \tag{2.3}$$

where N is the number of sampled points. As $\mathcal{T}_k$ is uniformly sampled, by Nyquist sampling theory, the Fourier components are related to physical frequencies given by $\nu_j = j/(Nt_{\text{samp}}) = j/(t_{\text{obs}})$ with a maximum frequency $\nu_{\text{Nyquist}} = 1/(2t_{\text{samp}})$, where t_{obs} is the length of the observation and t_{samp} is the sampling interval. Each Fourier bin therefore has a width of $1/t_{\text{obs}}$.

An efficient algorithm for computing the DFT is the Fast Fourier Transform (FFT) (Cooley & Tukey, 1965), which requires $N \log_2 N$ operations to calculate as opposed to the brute force N^2 method. For this thesis we have used the Fastest Fourier Transform in the West (FFTW) library[4] used by `PRESTO` pulsar software package. `PRESTO` has a task called `realfft`, based on the FFTW library, which applies the FFT to a time series.

The majority of radio pulsars have non-sinusoidal pulse profiles with small duty cycles (δ), which is the ratio of the pulse width, W, to the spin period P. The pulse profiles are typically of only a few percent of the pulse phase (see for instance pulsar profiles in Figure 2.2). These sharp pulses can be translated in the Fourier domain where the spectral power is shared among the fundamental periodicity and its harmonics, (see Figure 2.3). To maximize sensitivity, it is common practice to do a *harmonic summing*, which adds the Fourier components of harmonics with that of the fundamental to increase the signal-to-noise (S/N) of the signal. The number of harmonics of the fundamental periodicity depends on the shape of the pulse profile, as this scales as $N_{\text{harm}} \sim P/W$. Pulsars with wide pulse profiles have their Fourier power spread in small N_{harm}, whereas pulsars with narrow profiles (is the case for the majority of pulsars) have more significant harmonics. Although, when searching for unknown pulsar signals in the data, neither the fundamental frequency or the number of significant harmonics are known. Therefore, harmonically summed spectra are computed for all frequency bins. This is done by a stretch-and-sum technique, where a spectrum consisting of the sum of the fundamental and second harmonic can be computed by stretching the power spectrum by a factor of two and adding it to the original spectrum. This technique is repeated to compute high-order harmonic spectra. Periodic signals in the observation are found by searching these harmonically summed spectra for peaks. In practice, it is common to search summed spectra consisting of 1, 2, 4, 8, and 16 harmonics.

Once the dataset has been transformed into the Fourier domain, it is necessary to determine which periodic signals are statistically significant by analyzing the statistical properties of the Fourier power spectrum. The standard method is to set a threshold in S/N over what is considered a significant detection. By using the statistics of the noise in the data, and assuming the noise is Gaussian, we can calculate a good threshold value. The power in an individual bin is the sum of the squares of the real and imaginary parts of the complex Fourier values, and when harmonic summing is applied, it will be the sum of the power in m harmonics. In this general case, the probability of a sum of m harmonics to be over a given threshold power $\mathcal{P}_{min}$ (also known as false alarm probability) (e.g. Ransom et al., 2002):

$$p(\mathcal{P} > \mathcal{P}_{min}) = \sum_{j=0}^{m-1} \frac{\mathcal{P}^j}{j!} e^{-\mathcal{P}_{min}} \tag{2.4}$$

[4] http://www.fftw.org

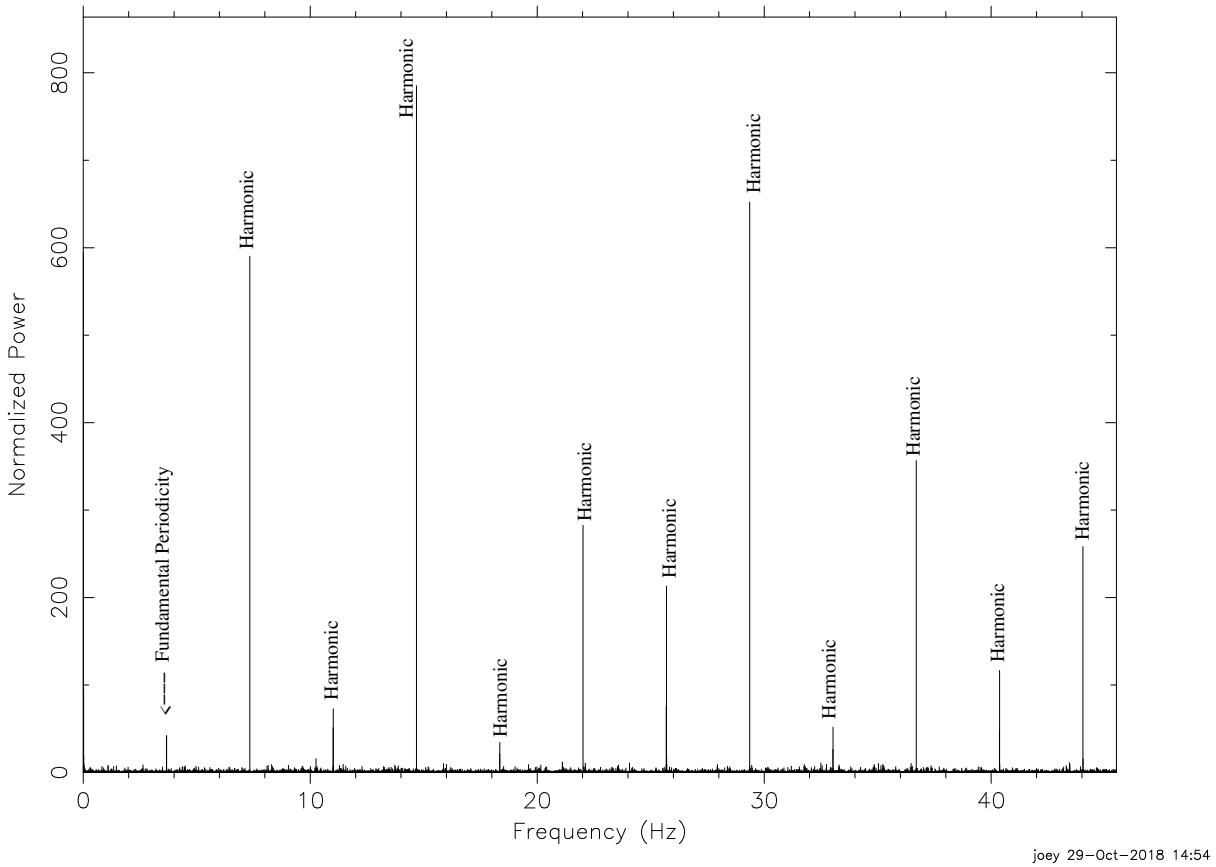

Figure 2.3. This is a power spectrum of a known re-detected PSR B0136+57 from HTRU-N data. This shows the important of *harmonic summing*, where we see the power of the signal is shared from fundamental periodicity and its harmonics. To maximize sensitivity to a pulsar, the power from all significant harmonics should be summed.

where $p(\mathcal{P} > \mathcal{P}_{min})$ is the probability that the power in a given Fourier bin exceeds $\mathcal{P}_{min}$ for m harmonics. By setting this probability such that it gives only a single false positive in number of trials independent Fourier trials, we may estimate a minimum significant power lever for a pulsar search. After all significant signals have been identified, they are all put into a candidate list for further analysis.

2.1.5 Acceleration Search

Thus far all the methods described to detect periodic signals in a time series have only considered signals which have approximately uniform frequency through the whole observation, as is the case for isolated pulsars. However, many of the most interesting pulsars are in binary systems, where the motion of the pulsar about its companion can cause the observed periodicity of the pulsar's signal to change over time due to Doppler shifts. This results in a time varying observed spin period ($P_{\rm obs}$) and its derivative ($\dot{P}_{\rm obs}$):

$$P_{\rm obs}(t) = P\Big[1 + \frac{v_l(t)}{c}\Big];\ \dot{P}_{\rm obs}(t) = P\frac{a_l(t)}{c}, \tag{2.5}$$

where P and $\dot{P}$ are the intrinsic spin period and spin period derivative, $v_l(t)$ and $a_l(t)$ are the pulsar velocity and acceleration component along the line of sight and c is the speed of light. The effect of a varying spin period during an observation will spread the power of the pulsar signal in several adjacent bins in the Fourier domain and reduce the chance of a detection. Fortunately, it is possible to recover some sensitivity to binary pulsars by doing *acceleration searches*. We use a matched filtering technique from `PRESTO` called `accelsearch`. The algorithm calculates how the power of a signal will spread for a given acceleration, a, which is assumed to be constant across the observation. This is true if the time segment that is being searched is less than 10% of the orbital period (Ransom et al., 2002). The value of maximum number, $z_{\rm max}$, of adjacent Fourier bins across which the power of the pulsar signal will be spread, can be calculated as:

$$z_{\rm max} = t_{\rm obs}^2 \frac{a}{cP} \tag{2.6}$$

where a is the acceleration of the pulsar, $t_{\rm obs}$ is the length of the observation, P is a potential fast pulsar's spin period, and c is the speed of light.

Large ranges of z can add to the already computational expensive pipeline, as it requires a number of operations that increase quickly with the number of acceleration trials. Nevertheless, it is a requirement to be sensitive to a pulsar in a exotic systems; such as double neutron star systems, undiscovered pulsar-black hole systems or pulsars in tight orbits. The discoveries of these type of systems led to studies of gravity, stellar evolution, neutron star mass measurements that impact the equation of state of dense matter. Discoveries of such exotic systems are the main drive of the surveys carried out in this thesis. In the AO327 survey, because of the small integration time of 60 s, this survey is sensitive to binary systems with orbital periods ∼10 min, or very accelerated systems with larger orbital periods.

2.1.6 Candidate selection, folding and confirmation

A list of potential significant periodic signals will be generated throughout the pipeline, after being searched at different trials of DM and acceleration values, all having different S/N values. The total number of candidates that pass the threshold for further analysis can reach up to several thousand in one observation. In order to lower the number of significant candidates it is necessary to sift through them using a `PRESTO` script called `sifting.py`, which checks for duplicate periodicities found at different DM and acceleration trials and keeps only one instance of each where the detection S/N is maximum. It also removes harmonically related candidates, rejects signals likely caused by RFI and periodicities too short or too long to be pulsars.

Once a final list of candidates has been compiled, the properties of the signal are evaluated by dedispersing and *folding* the raw data at each of the candidate's DM and period to form a *folded candidate diagnostic plot*. Folding uses the best estimate of a candidate's period and period derivative. It then slices the input data into individual pulses and aligning them in phase and finally averages them together to result in a folded candidate diagnostic plot, as seen in Figure 2.4. This process increases the S/N of the detected pulse profile, due to the individual pulses being aligned in phase and averaged coherently where the noise is uncorrelated. Since the S/N of a certain number of pulses, N, averaged together scales as S/N$\sim \sqrt{N}$, where the noise is assumed to be Gaussian distributed.

The folded candidate diagnostic plots are then inspected by eye to see if the candidate looks like a real pulsar, noise or RFI. A real pulsar looks like Figure 2.4: a periodic signal that is consistent over the time and bandwidth of the observation with a smooth DM curve that peaks at one point. In the end each observation pointing that has been searched, results in 150

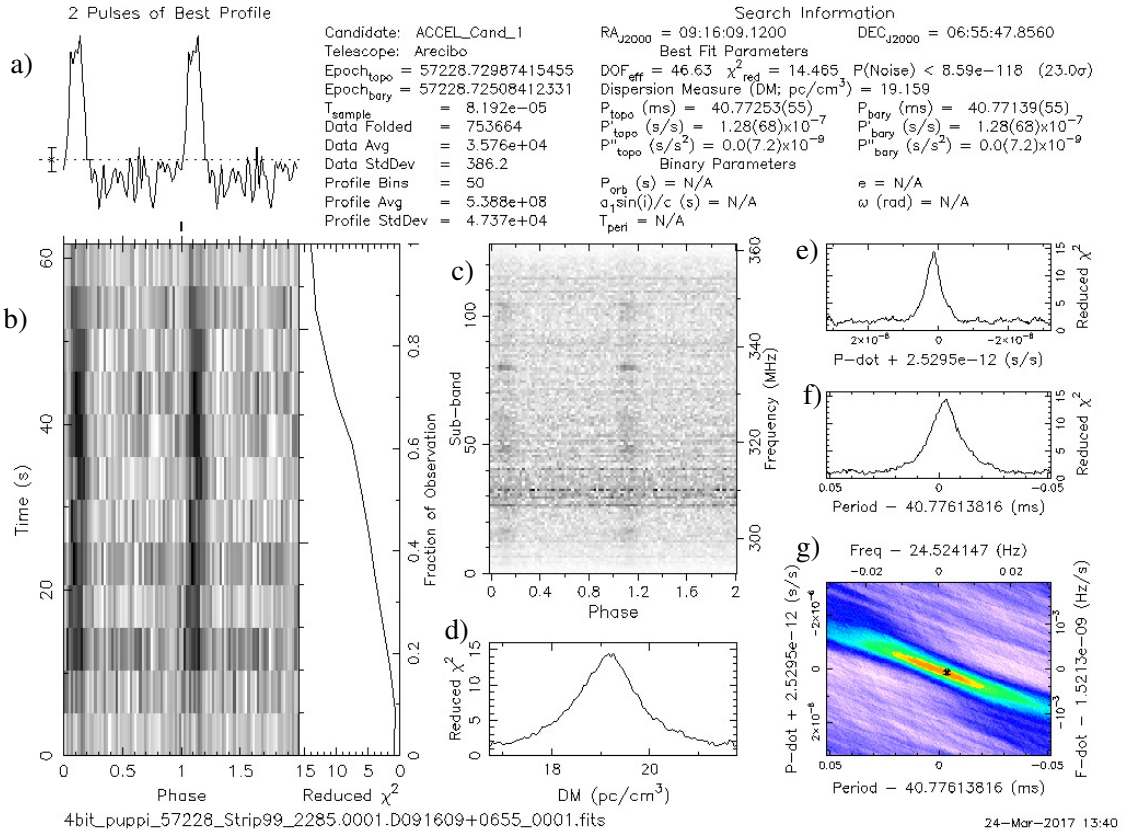

Figure 2.4. This is a PRESTO's folded candidate diagnostic plot of PSR J0916+06, a discovery I found in A0327 from June 22, 2017. This is a mildly recycled pulsar with a spin period of 40.77 ms, further observation revealed that this pulsar is isolated. The panels are a) are the pulses averaged together in the full observation resulting in an integrated pulse profile; b) time vs. phase plot, that helps determine the persistence of the signal in the observation; c) frequency vs. phase plot, showing how broadband the signal is in the full bandwidth of the receiver during the observation; d) Reduced χ^2 vs DM, showing where the pulsar's DM is measured the highest; e) and f) are the well measured spin period and period derivative of this pulsar; g) is a combination of panels e) and f) where the period and period derivative are well measured shown in red and lower values in purple, the used values intersect in the black cross. At the end of the pulsar searching pipeline, a plot like this will be created for every top periodic candidate found in an observation.

diagnostic plots to be inspected. Although, there are some machine-learning algorithms that evaluate the goodness of a candidate from their diagnostic plots (Eatough et al., 2010; Lee et al., 2013; Zhu et al., 2014). The top candidates that pass all the checks and final human inspection, can be re-observed at a later time for the final confirmation to realize if they are truly a new radio pulsar.

2.1.7 Search for Single Pulses

In addition to searching for periodic signals, most modern pulsar surveys also searched for astrophysical radio transient signals from either rotating radio transients (RRATs; Keane et al., 2011) and/or fast radio bursts (FRBs; Thornton et al., 2013). Objects known as RRATs first came to be when McLaughlin et al. (2006) found 11 transients in archival Parkes Multibeam Survey data. Further studies reveled that some RRATs are nulling pulsars that show sudden cessation of pulsed emission, and other RRATs are pulsars whose emission is below their luminosity cutoff (Keane et al., 2011). The searching for RRATs led to the discovery of FRBs. FRBs are a high energy astrophysical phenomenon of unknown origin, that are transient radio pulse lasting a few milliseconds. FRBs are astrophysical sources that come from extragalactic distances and the majority of them are single events, except for the repeater FRB 121102 (Spitler et al., 2016) and most recently FRB 180814 (The CHIME/FRB Collaboration et al., 2019). The number of FRB discoveries has increased by searching in pulsar survey archival data and the addition of new radio telescopes with large field of views, such as Australian Square Kilometer Array Pathfinder (ASKAP), the upgraded Molonglo Observatory Synthesis Telescope (UTMOST), and Canadian Hydrogen Intensity Mapping Experiment telescope (CHIME).

To detect these dispersed astrophysical pulse signals we use matched filtering algorithms. Given a time series of primarily of Gaussian noise, single pulses are individual events that deviate by several standard deviations from the mean. In order to detect these events, the dedispersed time series is smoothed by adding groups of neighboring time samples and then searched for statistically significant events. These dedispersed time series are convolved with boxcars of various widths. These convolved time series are then searched for significant peaks. A good threshold needs to be determined in order to avoid many false detections, a well known threshold for a standard single pulse is about $(\mathrm{S/N})_{\mathrm{thres}} \simeq 6$ (Lorimer & Kramer, 2004).

Throughout this thesis, a python routine from `PRESTO` called `single_pulse_search.py` and a new recent method called Clusterrank (Deneva et al., 2016) have been used for identifying dispersed astrophysical pulses. Some of the transient signals discovered by single-pulse searches are slow pulsars from surveys with short integration times where there are not enough pulses for a detection to be made via periodicity search. This is especially important for AO327, since the observing time for each pointing is 60 s. For example, Figure 2.5 shows a diagnostic plot from Clusterank single pulse search of a recent discovery a PSR J1917+31 with a spin period of 1.3 s.

2.1.8 Survey Sensitivity

The minimum detectable flux density of a pulsar search survey can be estimated by the radiometer equation for pulsars, as described in Lorimer & Kramer (2004). The S_{min} is the minimum detectable flux density in mJy corresponding to signal to noise threshold, S/N_{thres}. The radiometer equation for pulsars is:

$$S_{\mathrm{min}} = \beta \frac{(S/N_{\mathrm{thres}})T_{\mathrm{sys}}}{G\sqrt{n_{\mathrm{p}} t_{\mathrm{obs}} \Delta f}} \sqrt{\frac{W}{P-W}}. \tag{2.7}$$

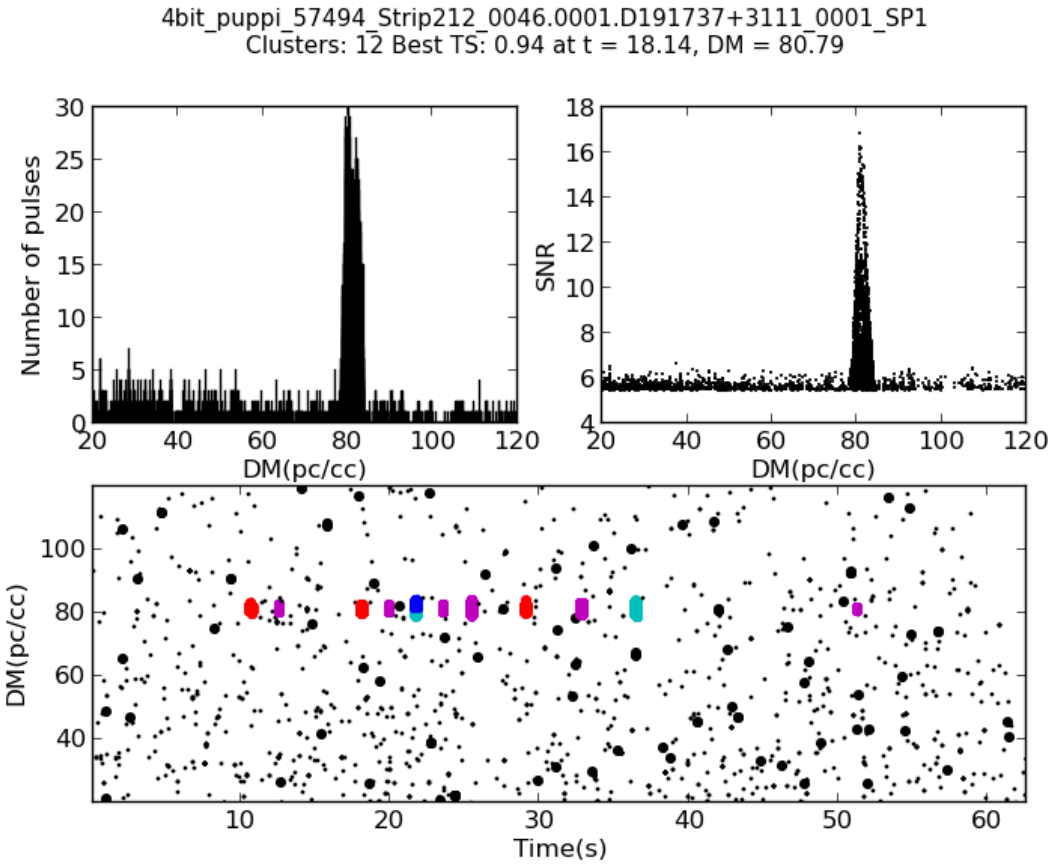

Figure 2.5. This an output from a single pulse search of data from the AO327 of a recent discovery of PSR J1917+31. The top panels are a Histogram of the number of events vs. DM (left) and event SNR vs. DM (rigth). The bottom panel is the events plotted in DM vs. time of the observation. The colored points are clusters identified by Clusterrank with from high SNR starting from the color red, follow by magenta, cyan, green, and blue being the lowest SNR.

Here, β is a correction factor accounting for losses during signal digitization, $T_{\rm sys} = T_{\rm rec} + T_{\rm sky}$ is the system noise temperature in Kelvin, consisting of receiver and sky temperatures, G is the gain of the telescope in KJy^{-1}, $n_{\rm p}$ is the number of polarizations, $t_{\rm obs}$ is the observation time in seconds, Δf is the observation bandwidth in MHz, P is the spin period of the pulsar that is observed and W is the width of the pulse profile. The observed pulse width W is a combination of many factors that contribute to evaluating the sensitivity of a survey, $W = \sqrt{W_{\rm int}^2 + \Delta t_{\rm DM,1ch}^2 + \Delta t_{\delta \rm DM}^2 + \Delta t_{\rm samp}^2 + \tau_{\rm s}^2}$. We assume an intrinsic pulse width $W_{int} = 0.1\,P$. In order to calculate the dispersion smearing over one channel ($\Delta t_{\rm DM,1ch}$) and the dispersion smearing due to DM error in the worst case, when the pulsar DM is halfway between two trial DMs ($\Delta t_{\delta \rm DM}$), we use the cold plasma dispersion relation from Equation 1.14. The term $\Delta t_{\rm samp}$ is the actual sampling time for the survey, and scattering time $\tau_{\rm s}$ can be calculated from an empirical fit of observed scattering versus DM from e.g. Bhat et al. (2004). Although Equation 2.7 takes account of many parameters, it fails to account for the influence of RFI, which can affect the detection of a pulsar signal as shown.

Table 2.1. Software packages and relative routines used in this thesis for pulsar timing.

Operation	Routine	Software Package
Dedispersion / Folding	`dspsr`	`DSPSR`
RFI removal	`pazi`	`PSRCHIVE`
Archive manipulation	`pam`	`PSRCHIVE`
Standard profile creation	`psradd`	`PSRCHIVE`
	`psrsmooth`	`PSRCHIVE`
ToA extraction	`pat`	`PSRCHIVE`
Timing Analysis	`tempo`	`TEMPO`
	`tempo2`	`TEMPO2`
Polarization calibration	`pac`	`PSRCHIVE`
RM measurement	`rmfit`	`PSRCHIVE`

2.2 Pulsar Timing

The full potential of a pulsar survey can only be realized through the follow-up of its discoveries. A follow-up of a pulsar needs to be repeatedly observed and analyzed using *pulsar timing* techniques. Pulsar timing is a process of regularly monitoring the rotation of the pulsar by tracking precisely the times of arrival of the radio pulses (TOAs) and comparing them to a model. This model, which is referred as a timing solution or ephemeris, contains the spin period, spin-down, astrometric and any potential binary motion parameters of the pulsar. Because pulsars are stable rotators, especially MSPs, it is possible to develop a phase-connected timing solution that accounts for every single rotation of the pulsar. The phase-connected model can be further refined with more observations to determine the pulsars parameters to a higher precision.

Several pulsar software packages have been developed to aid to obtain a timing solution. The data analysis and tools in order to reduce pulsar observations into a set of TOAs are carried out with `PSRCHIVE` software package (Hotan et al., 2004; van Straten et al., 2012). The timing analysis where the timing residuals are used to develop and refine a timing solution is done with `TEMPO`[5] and/or `TEMPO2`[6] (Edwards et al., 2006; Hobbs et al., 2006). A list of software packages and routines used in this thesis to do pulsar timing are in Table 2.1. The following sections will be an over view of the necessary steps in order to develop a timing solution for a pulsar.

2.2.1 Observations and data acquisition

The first observations are set up to observe the pulsar in such a way that we can take into account for every rotation of the pulsar from one observation to the next. It is common practice to take the first observations in *incoherent dedispersion mode*, since the pulsar's parameters are not known to a high precision. In order to build upon an initial model, more observations must be made, and sometimes more observations are needed for pulsars in binary with orbital periods longer than one month. After sufficient data is taken to produce an initial phase-connected solution, using the manual method described by Freire & Ridolfi (2018).

[5] http://tempo.sourceforge.net
[6] http://www.atnf.csiro.au/research/pulsar/tempo2/

In the case of an isolated pulsar, an initial model consists of the spin period, position and DM. If the pulsar is in a binary, an orbital solution for the pulsar must first be determined, see Section 2.2.3.4. Once an initial phase connected solution has been determined, the following observations can be taken in *coherent dedispersion mode* up to at minimum of one year. The reason for monitoring a pulsar for a minimum of one year is because the position of a pulsar is not precisely measured. By monitoring how the TOAs are altered by the Earth's motion around the Sun, we can obtain very accurate position for the pulsar, which can be later followed up at other frequencies (e.g. optical or γ regime). Also another reason is to measure the pulsar's spin-down rate, which allows us to get characteristic of the pulsar such as age, magnetic field strength and spin-down luminosity. For pulsars in binary systems it is important to have observations that cover its whole orbit. Good orbital coverage allows for an accurate measurement of the orbital parameters.

2.2.1.1 Polarization Calibration

Pulsars tend to be highly polarized sources, showing both circular and linear polarizations. Polarization measurements from pulsars can provide information of the pulsar emission process and about the medium through which it propagates. During a pulsar observation, the pulsar signal goes through transformations during the propagation and reception of the radio waves that act to change the state of polarized radiation, such as Faraday rotation through the ISM (see Section 1.2.2) and instrumental effects. Therefore, some systematic differences in the observed pulse total intensity profile can be introduced. Uncalibrated pulse profiles can yield inaccurate TOAs, which can cause trends in pulsar timing data that may lead to errors in the determination of timing parameters. For this reason, it is important to do polarization calibration in order to correct for instrumental effects and properly measure polarization properties of the pulsar. In order to do this, we express the instrumental effects as a interdependent Mueller matrix, M_{effects} which acts as a transfer function between the measured Stokes vector of the pulsar, S_{obs}, and true Stokes parameters, S_{int}, by:

$$S_{obs} = M_{\text{effects}} \times S_{int} \tag{2.8}$$

By calibrating the observing system, we can determine M_{effects} and solve for S_{int}, as done by Heiles et al. (2001). The most basic way to perform polarization calibration is done by the use of an artificial signal (known as noise diode) that is injected directly into the the receiver receptors, usually done prior to a pulsar observation. The relative gain and phase of the two polarization feeds are then adjusted following the method of Britton (2000). As a result, pulsar observations that have gone through polarization calibration yield more reliable to determine pulse profiles and accurate TOAs. The profiles can also be used for polarimetric studies (e.g. Everett & Weisberg, 2001; Manchester et al., 2010).

2.2.2 Determining the Times-of-Arrival

The main goal of each timing observation is the measurements of TOAs. These TOAs marks the arrival time of individual pulses. It is common to report a TOA as the *Modified Julian Date* (MJD) that corresponds to the chosen reference point of the pulse profile, that is known as the *fiducial point*. A TOA is calculated by determining the phase offset between the observed pulse profile and a reference profile that is known as a *template*. A template is a high S/N reference profile that consists of several high S/N observations coherently combined or a result of fitting

Gaussian's to a high S/N profile to create a smooth low-noise *analytical template*. In this thesis, tools from `PSRCHIVE` called `psrsmooth` were used to create an *analytical template*. The pulse profiles are then cross-correlated with the analytical template using the procedure described in Taylor (1992) and implemented with `PSRCHIVE` routine called `pat` to determine TOAs of an observation.

2.2.3 Timing Analysis

Once having generated TOAs from pulsar observations, the next step is to perform the timing analysis. This process requires an initial timing model that can predict the phase of each TOA, which are then compared to the measured phases. The model's parameters are iteratively refined to improve the predictions, which is minimizing the difference between the measured and predicted phases. In this thesis, public available software called `TEMPO` and `TEMPO2` (Edwards et al., 2006; Hobbs et al., 2006) was used to analyze timing data using the techniques as already mentioned above, details about this process are in the following subsections.

2.2.3.1 Timing Model

In order to extract the maximum information from pulsar timing observatins, the TOAs generated must be transformed to a corresponding proper time of emission in the pulsar frame. We must take into account of terms related to position, velocities, and masses within our solar system, propagation effects in the ISM, and for the case of pulsars in binary the orbital motion effects. As from Taylor (1992), the transformation of a measured TOA, $t_{\rm obs}$, to the pulsar's proper time, T, can be summarized as:

$$T = t_{\rm obs} + t_0 + \Delta_{\rm clk} - D/f^2 + [\Delta_{\rm R_\odot} + \Delta_{\rm E_\odot} - \Delta_{\rm S_\odot}] - [\Delta_{\rm R} + \Delta_{\rm E} + \Delta_{\rm S} + \Delta_{\rm A}]. \tag{2.9}$$

Here t_0 is a reference TOA; $\Delta_{\rm clk}$ represents any measured offsets between the local observatory clock and the terrestrial time standard; D/f^2 is the dispersion delay (where D is the DM of the pulsar) for propagation at frequency f over the path from pulsar to Earth; $\Delta_{\rm R_\odot}, \Delta_{\rm E_\odot}, \Delta_{\rm S_\odot}$ are propagation delays and relativistic time adjustments within the Solar System; the $\Delta_{\rm R}, \Delta_{\rm E}, \Delta_{\rm S}$ are equivalent corrections although for a pulsar in a binary; and $\Delta_{\rm A}$ is a term related to aberration effects in the pulsar orbit. All these terms are expressed with more detail in sections below. The pulsar's proper time, T, can then be related to the rotational phase of the pulsar, $\phi(T)$ expressed as a Taylor expansion:

$$\phi(T) = \nu T + \frac{1}{2}\dot{\nu}T^2 + \frac{1}{6}\ddot{\nu}T^3 + ... \tag{2.10}$$

where ν is the spin frequency of the pulsar, $\dot{\nu}$ and $\ddot{\nu}$ are its first and second time derivatives.

2.2.3.2 Barycentering terms

The TOAs measured at the radio telescope are *topocentric* and need to be corrected for Earth and Solar System effects. The terms $(\Delta_{\rm clk}, \Delta_{\rm R_\odot}, \Delta_{\rm E_\odot}, \Delta_{\rm S_\odot})$ from Eq 2.9 allow us to refer the topocentric TOA to the Solar System barycenter (SSB), a short description will be presented below of each term. `TEMPO` and `TEMPO2` use accurate models of the motion of the Earth and the other Solar System bodies produced by NASA's Jet Propulsion Laboratory (JPL). The models are Solar System ephemerides (SSEs).

Δ_{clk} This term refers to the local observaotry clock correction factor which takes into account any offsets in the observatory clock from a managed time standard such as International Atomic Time (TAI).

$\Delta_{\text{R}_\odot}$ The *Römer delay* within the Solar System, is the geometric delay caused by the annual motion of the Earth around the Sun and the daily spin of the Earth. This delay depends on the relative position of the Earth along its orbit, with respect to the pulsar. This can be expressed from Lorimer & Kramer (2004):

$$\Delta_{\text{R}_\odot} = -\frac{[(\vec{r}_{\text{SSB}} + \vec{r}_{\text{EO}}) \cdot \hat{s}]}{c} \tag{2.11}$$

where $\vec{r}_{\text{SSB}}$ is the position vector of the center of the Earth relative to the SSB, $\vec{r}_{\text{EO}}$ is the position of the phase center of the telescope with respect to the center of the Earth, $\hat{s}$ is the unit vector pointing in the direction of the pulsar, and c is the speed of light. Figure 2.6 shows this graphically.

$\Delta_{\text{E}_\odot}$ The *Einstein delay* within the Solar System, is the time dilation associated with the relativistic space-time coordinate frame transformation from the radio telescope site to the SSB.

$\Delta_{\text{S}_\odot}$ The *Shapiro delay* within the Solar System, is the time delay caused by the curvature of space-time due to massive bodies in the Solar System.

As descibed in Section 1.2, the pulsar's emitted signal is affected by dispersion delays from the ISM. However, due to the Doppler shift caused by the Earth's motion, the observed frequency in the telescope reference frame is different from the SSB. The barycentric frequencies of each TOA must be computed to accurately measure and remove the effect of the ISM. This can be done by using accurate SSE in order to calculate the velocity of the telescope to correct for Doppler shift the observed frequencies.

Furthermore, unmodeled DM variations can also cause delays in the TOAs. In order to correct for these variations the pulsar must be observed at different frequencies, since ISM effects are mostly frequency dependent (Keith et al., 2013). Once having multiple different frequency observations of the pulsar, DM variations are measured (e.g Figure 2.7). A DM model can be created and added in the pulsar ephemeris for TOAs to be free from DM variations.

2.2.3.3 Binary terms

In the case of an isolated pulsar, applying the correction terms described above in Section 2.2.3.2 is enough to determine the topocentric TOAs to the SSB. For a pulsar in a binary system, timing models must account for the last four terms ($\Delta_{\text{R}} + \Delta_{\text{E}} + \Delta_{\text{S}} + \Delta_{\text{A}}$) from Equation 2.9, which the basic principle are similar to the case of removing Solar System effects described above.

For a pulsar in a binary, the Keplerian parameters are necessary (for most binaries they are sufficient) to describe the orbital motion of the system. These parameters are:

- orbital period (P_b)
- eccentricity (e), where given a semi-major axis a_p and a semi-minor axis b_p as seen in

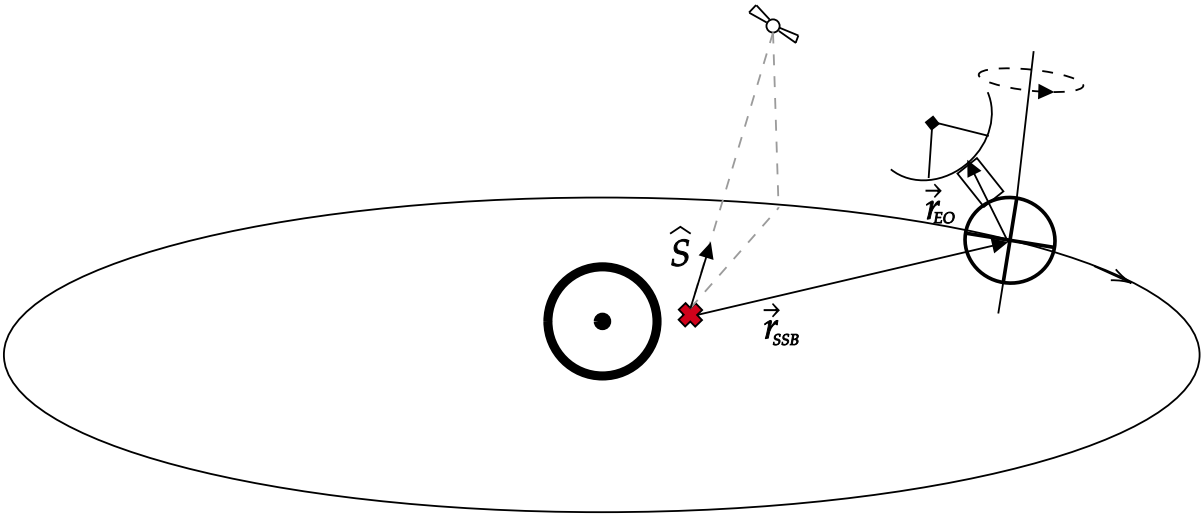

Figure 2.6. This is an illustration for correcting TOAs due to Römer delay, $\Delta_{R_\odot}$.

Figure 2.8, eccentricity is defined by

$$e = \sqrt{1 - \left(\frac{b_p}{a_p}\right)^2} \tag{2.12}$$

- longitude of periastron (ω), is the angle between the ascending node and periastron (the point of closest separation in a binary system) in the direction of motion of the pulsar, shown in Figure 2.8.

- epoch of periastron(T_0), a reference point in time when the pulsar passed through periastron (the point of closest separation in a binary system).

- projected semi-major axis, ($x = a_p \sin(i)$), where a_p is the semi-major axis of the pulsar's orbit along the line of sight and i is the orbital inclination as shown in Figure 2.8.

In the case for almost circular binaries from particularly MSPs, the eccentricities are very low and the epoch of periastron and the longitude of periastron are poorly defined. In such cases, eccentricity and the longitude of periastron are combined into the Laplace parameters $\epsilon_1 = e \sin(\omega)$ and $\epsilon_2 = e \cos(\omega)$ and the longitude of periastron becomes the epoch of ascending node, T_{asc} (Lange et al., 2001). The original Keplerian parameters can then be derived by:

$$e = \sqrt{\epsilon_1^2 + \epsilon_2^2}, \tag{2.13}$$

$$\omega = \arctan(\epsilon_1/\epsilon_2) \tag{2.14}$$

$$T_0 = T_{asc} + \frac{P_b}{2\pi} \arctan(\epsilon_1/\epsilon_2). \tag{2.15}$$

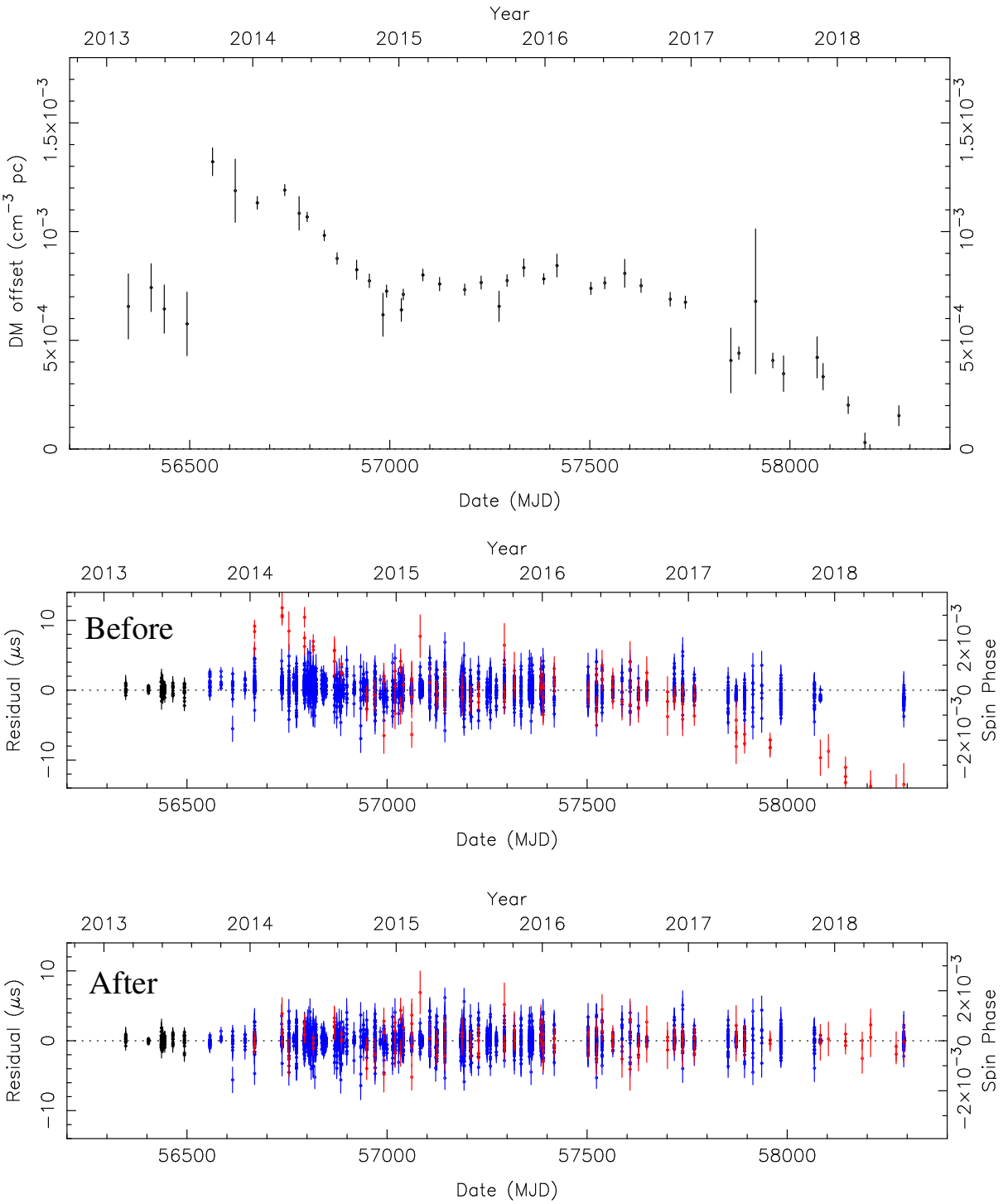

Figure 2.7. This figure shows DM variations of a PSR J2234+0611 at the top panel we show DM offsets as a function of time. Middle: We show the residuals affected by DM variations. Bottom: We show the residuals after a DMX model was created and implemented in its ephemeris to correct for TOAs that were affected by these variations. Black residuals are data from the initial incoherent observations at 1.5 GHz, blue data from the coherent dedispersed observations at 1.5 GHz, and red are the coherent dedispersed observations at 430 MHz. The red residuals are affected more by the DM variations, since this effect is strongest at lower frequencies. A five years of high precision timing of PSR J2234+0611 is presented in a publication, in which I was a part of, in (Stovall et al., 2019).

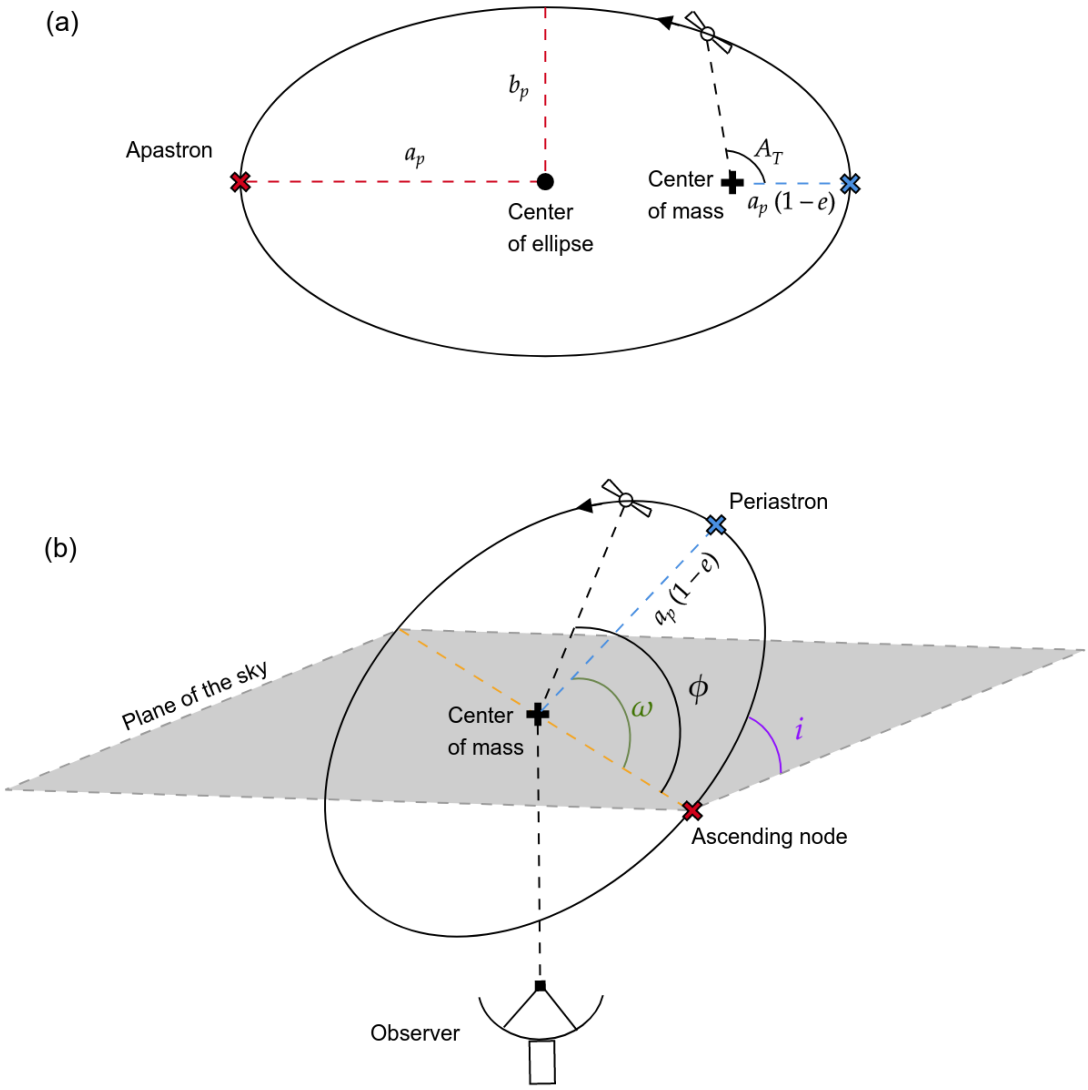

Figure 2.8. This is a schematic diagram representing the orbital elements in a Keplerian orbit and other associated quantities. (a) In this elliptical orbit, the *semi-major axis*, a_p, and the *semi-minor axis*, b_p, are displayed, where the *eccentricity* of an orbit is defined as $e = \sqrt{1-(b_p/a_p)^2}$. The closest approach of the pulsar to the center of mass of the binary system marks periastron, given by the longitude ω and a chosen epoch T_0 of its passage. The distance between center of mass and periastron is given by $a_p(1-e)$. (b) Illustration of a pulsar in an orbit as viewed by an observer in Earth. The plane of the sky is marked in gray which is perpendicular to the line of sight and is fixed to the center of mass of the orbit. The yellow dotted line is the intersection of the orbital plane with the plane of the sky at an inclination angle i. The ascending node is the point where the pulsar crosses the plane of the sky when traveling away from the observer. The orbital phase ϕ is the angle between the ascending node and the position of the pulsar, and the longitude of periastron ω is the angle between the ascending node and the position of periastron.

2.2.3.4 Determination of the Pulsars Orbits

In order to generate a phase-connected timing solution for a pulsar in a binary, we need to first develop good estimate of an orbital solution. As described in Section 2.1.5, the acceleration of the pulsar due to the gravitational pull of the companion will result in a Doppler shifted spin period of:

$$P_{obs}(t) = P\Big[1 + \frac{v_l(t)}{c}\Big]. \tag{2.16}$$

The velocity of the pulsar along the line of sight, v_l, of Eq. 2.16 can be expressed as a function of the system's orbital parameters from Lorimer & Kramer (2004):

$$v_\mathrm{l}(A_\mathrm{T}) = \frac{2\pi a_\mathrm{p} \sin i}{P_\mathrm{b}\sqrt{1-e^2}} \left[\cos(\omega + A_\mathrm{T}) + e\,\cos(\omega)\right] \tag{2.17}$$

where A_T is the true anomaly.

In order to determine the orbit, several observations of the pulsar must be obtained, that have a well measured spin period for the pulsar. The observed spin period of a binary system is modulated by Equation 2.16 and Equation 2.17. Fitting a Keplerian model to the observed points, using available software such as `FITORBIT` [7], you can determine the orbital parameters. By determining well fitted curve to the observed spin period as a function of time. In the case of a circular orbit, the observed spin period as a function of time will be a sinusoid type curve. In the case of an eccentric binary, the shape of the curve will be more complicated depending on the orientation and eccentricity of the orbit.

For pulsars with a lack of sufficient observation cadence, an alternate approach can be used to determine a pulsar's binary parameters. Freire et al. (2001) described a technique that only uses the changing apparent acceleration and spin period of the pulsar at sparse observations. The changing line of sight acceleration of a pulsar can be described as:

$$a_l(A_T) = -\Big(\frac{2\pi}{P_b}\Big)^2 \frac{x}{(1-e^2)^2}\,(1 + e\,\cos(A_T))^2\,\sin(\omega + A_T). \tag{2.18}$$

Then Equations 2.16 and 2.18 can be plotted parametrically to form a *period vs acceleration diagram*, that forms a closed loop over one orbital period of the pulsar. The measurements of the changing barycentric period and acceleration between observations can used to estimate the orbital parameters. This method works very well for circular binaries, which appear as perfect ellipses in the diagram and can easily determine the orbital parameters.

2.2.3.5 Mass Function and post-Keplerian parameters

The Keplerian parameters can be used to estimate the mass of the companion using the *mass function*. The *mass function* (e.g. Lorimer & Kramer, 2004) is:

$$f(m_p, m_c) = \frac{(M_c \sin i)^3}{(M_p + M_c)^2} = \frac{4\pi x^3}{T_\odot P_b^2}, \tag{2.19}$$

where m_p and m_c are the masses of the pulsar and its companion in units of solar mass ($M_\odot$), and $T_\odot = (GM_\odot/c^3) = 4.925490947\mu s$ is the solar mass ($M_\odot$) in time units (c is the speed of light and G is Newton's gravitational constant). If no other parameters are available, we can

[7] http://www.jb.man.ac.uk/pulsar/Resources/tools.html

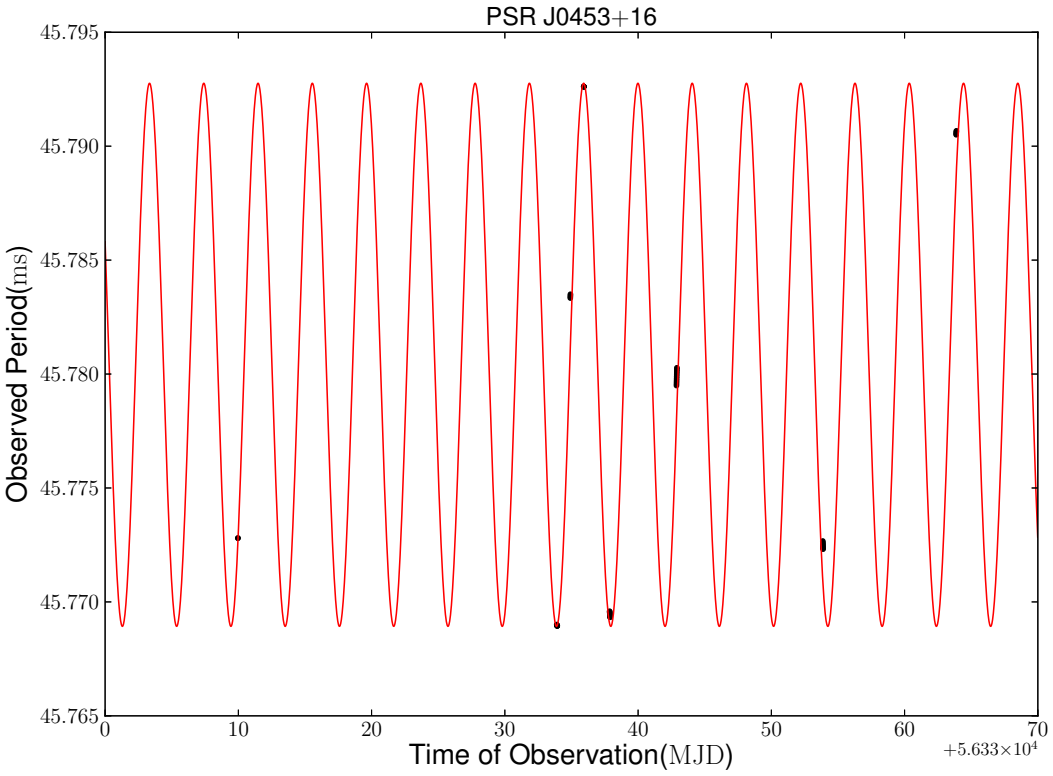

Figure 2.9. Observed Doppler-shifted spin period of newly discovered pulsar, now known as PSR J0453+1559, (black dots) are plotted against time with a fitted red line that best describes the orbit of the system.

assume a mass of a pulsar ($M_p = 1.35\ M_\odot$) and a maximum and median orbital inclinations ($i = 90°, 60°$). An estimation of the minimum and median companion masses can be obtained with the *mass function*. But we are still left with two unknowns in Equation 2.19, which can be determined by measuring two or more *post-Keplerian* (PK) parameters.

Unfortunately, precise mass measurements in general are hard to achieve because suitable systems are rare. Up to now, only 41 pulsars have precise estimates of their neutron star mass[8]. One way to directly measure the masses of a pulsar in a binary is by measuring two or more PK parameters, which describe relativistic corrections. Each of the PK parameters produce their own characteristic timing residual signatures (Damour & Deruelle, 1986), for that reason it can be taken into account by the process of pulsar timing. In GR and other gravity theories (e.g. Blandford & Teukolsky, 1976; Damour & Deruelle, 1985, 1986), the five important PK parameters are as described by Lorimer & Kramer (2004):

- The rate of advance of periastron, $\dot{\omega}$, is the rate which the orientation of the orbit rotates through space, in GR, this is given by

$$\dot{\omega} = 3T_\odot^{2/3}\left(\frac{P_b}{2\pi}\right)^{-5/3}\frac{1}{1-e^2}(M_p + M_c)^{2/3}. \tag{2.20}$$

[8] https://www3.mpifr-bonn.mpg.de/staff/pfreire/NS_masses.html

- The time dilation and gravitational redshift parameter, γ, referred as the Einstein delay, which describes the relativistic dilation experienced by the pulsar signal as it traverses the gravitational potential of the binary system:

$$\gamma = T_{\odot}^{2/3}\Big(\frac{P_b}{2\pi}\Big)^{1/3} e\,\frac{M_c(M_p+2M_c)}{(M_p+M_c)^{4/3}}. \tag{2.21}$$

- The orbital period decay, $\dot{P}_b$, is the rate at which the orbital period decreases due to the emission of GWs, given in GR by:

$$\dot{P}_b = -\frac{192\pi}{5}T_{\odot}^{2/3}\Big[\frac{1+(73/24)e^2+(37/96e^4)}{(1-e^2)^{7/2}}\Big]\frac{M_pM_c}{(M_p+M_c)^{1/3}}. \tag{2.22}$$

- The Shapiro delay has two parameters, the range, r, and shape, s, which describe the extra time required by the pulsar signal to travel through the curved space-time containing the companion, given in GR by:

$$r = T_{\odot}M_c,\ s = \sin(i) = T_{\odot}^{-1/3}\Big(\frac{P_b}{2\pi}\Big)x_p\frac{(M_p+M_c)^{2/3}}{M_c}. \tag{2.23}$$

The relativistic effects described by these PK parameters depend on the Keplerian parameters and the masses of the pulsar and companion. Measuring two of these effects provides two more equations which together with *mass function* allows a solution of the 3 unknowns (i, M_p, M_c). This process can be visualized by plotting them in a *mass-mass diagram*, where two or more of these PK parameters intersect, which result in measuring of individual masses for the pulsar and the companion. The degree of how precisely these PK parameters are measurable varies depending upon the binary system itself. For example, a pulsar in a circular orbit will make the measurement of $\dot{\omega}$ more difficult due to the low precision available on both ω and T_0. Also, the measurement of the Shapiro delay parameters r and s depends upon the binary being close to edge on in its inclination for the binary companion to pass close to the line of sight during *superior conjunction*. In the following Chapters 3, 4, 5, there will be *mass-mass diagrams* of pulsar in binary systems that have mass measurements.

The pulsar timing software analysis `TEMPO`[9] has many timing models used to describe the binary motion and relativistic corrections for any type of binary system. The models used throughout this thesis are the DD model, DDGR model, DDH model and ELL1 model. The DD model described by (Damour & Deruelle, 1985, 1986), incorporates the required relativistic corrections for all the PK parameters presented in this thesis in a theory-independent fashion, which allows for tests of multiple gravitational theories to be conducted. The DDGR model described by (Taylor, 1987; Taylor & Weisberg, 1989), assumes the correctness of GR and ensures consistency between the PK parameters according to their GR definitions, only fitting for individual masses of the pulsar and the companion. The DDH model described by Freire & Wex (2010), was designed to allow for easier separation and constraint of the Shapiro delay by re-parameterizing it as the orthometric amplitude h_3 and orthometric ratio ς. These orthometric parameters relate to the standard Shapiro parameters r and s by:

$$\varsigma = \sqrt{\frac{1-\bar{c}}{1+\bar{c}}} \tag{2.24}$$

[9] http://tempo.sourceforge.net

where

$$\bar{c} = \sqrt{1 - s^2} = \cos(i), \tag{2.25}$$

and

$$h_3 = r\varsigma^3. \tag{2.26}$$

Finally, the ELL1 model described by (Lange et al., 2001), parameterizes the pulsar's binary motion in a way that is particularly well suited to describe orbits with small eccentricities; it uses the Laplace parameters described in Section 2.2.3.3. A summary of these and other binary models can be found in the literature (e.g. Damour & Taylor, 1992; Edwards et al., 2006, and references therein).

2.2.4 Residuals

Once the timing formula Equation 2.9 has been used to derive the pulsar proper time of emission and have generated topocentric TOAs. They can now be used into Equation 2.10 to calculate the associated rotational phase of the pulsar. The observed phases are then compared with the theoretical values predicted by the timing model, to generate the *timing residuals*. These residuals are the basis of pulsar timing. The quality of a timing model is then measured by the reduced χ^2 of the *timing residuals*. The reduced χ^2 is expressed as:

$$\chi^2 = \sum_i \left(\frac{N(t_\mathrm{i}) - n_\mathrm{i}}{\sigma_\mathrm{i}} \right)^2 \tag{2.27}$$

where $N(t_\mathrm{i})$ represents each measured arrival time in units of rotational phase, n_i is the nearest integer to each $N(t_\mathrm{i})$ and σ_i is the TOA uncertainty in units of rotational phase. If the timing model is good enough to predict, on average, the TOAs within the uncertainties, we get a reduced $\chi^2 \sim 1$. `TEMPO` and `TEMPO2` always attempts to minimize the χ^2 of the residuals by varying the timing parameters. This is how timing solution is determined. The *timing residuals* will then be Gaussianly distributed around zero and with no trends. Conversely, if some effects are not correctly taken into account, this will result in the reduced $\chi^2 > 1$ and the residuals will show clear trends (some examples are shown in Lorimer & Kramer (2004) Figure 8.2).

2.2.5 Summary

We will see in the next chapters how searching for new discoveries can lead to further our understanding about pulsars. We focus on the study of recycled pulsars, which are descendants from a close, interacting stellar systems. They are mainly characterized by their spin periods, magnetic field strengths and masses; which all these quantities are the result of previous binary interactions. Therefore, we can use these quantities as fossil records and learn about binary evolution (Bhattacharya & van den Heuvel, 1991; Tauris et al., 2011, 2012).

Chapter 3

Pulsar J0453+1559: A Double Neutron Star System with a Large Mass Asymmetry

---

This chapter is based on an article published in the Astrophysical Journal (Martinez et al., 2015). The article can be found online at: https://iopscience.iop.org/article/10.1088/0004-637X/812/2/143

The first initial orbital parameters and initial mass estimates were first presented in my masters thesis. The final timing analysis and orbital observation campaigns of two full orbits, which led to the precise mass estimates, and the writing of this paper was done during my doctoral studies. I am the lead author of the article. My main contributions include the discovery and the follow-up of this PSR J0453+1559. I performed all of the observations, processed the data, and performed the timing analysis. The text, figures, and tables have only been modified to match the style and format of this thesis.

The full list of authors is:
J.G. Martinez, K. Stovall, P.C.C. Freire, J.S. Deneva, F.A. Jenet, M.A. McLaughlin, M.Bagchi, S.D. Bates, A. Ridolfi

Abstract

To understand the nature of supernovae and neutron star (NS) formation, as well as binary stellar evolution and their interactions, it is important to probe the distribution of NS masses. Until now, all double NS (DNS) systems have been measured to have a mass ratio close to unity ($q \geq 0.91$). Here, we report the measurement of the individual masses of the 4.07-day binary pulsar J0453+1559 from measurements of the rate of advance of periastron and Shapiro delay: the mass of the pulsar is $M_p = 1.559 \pm 0.005\,M_\odot$ and that of its companion is $M_c = 1.174 \pm 0.004\,M_\odot$; $q = 0.75$. If this companion is also a NS, as indicated by the orbital eccentricity of the system ($e = 0.11$), then its mass is the smallest precisely measured for any such object. The pulsar has a spin period of 45.7 ms and a spin period derivative of $\dot{P} = (1.8616 \pm 0.0007) \times 10^{-19}$ s s^{-1}; from these we derive a characteristic age of $\sim 4.1 \times 10^9$ years and a magnetic field of $\sim 2.9 \times 10^9$ G, i.e, this pulsar was mildly recycled by the accretion of matter from the progenitor of the companion star. This suggests that it was formed with (very approximately) its current mass. Thus, NSs form with a wide range of masses, which is important for understanding their formation in supernovae. It is also important for the search for gravitational waves released during a NS-NS merger: it is now evident that we should not assume all DNS systems are symmetric.

3.1 Introduction

Double neutron star (DNS) systems are rare and valuable physical laboratories that can be used to precisely test gravity theories. The first such system, PSR B1913+16, provided evidence for orbital decay due to the emission of gravitational waves, as predicted by general relativity (GR; Hulse & Taylor 1975 and Taylor & Weisberg 1982). Since the discovery of PSR B1913+16, nine additional DNS systems have been discovered in the Galaxy (see Table 3.1), including one such system in which both neutron stars (NSs) have been detected as radio pulsars, PSRs J0737−3039A and B (Burgay et al., 2003; Lyne et al., 2004). This system provides one of the best available tests of GR and alternative theories of gravity in the strong-field regime (Kramer et al., 2006).

DNS systems begin as two high-mass stars. The higher-mass star will undergo a supernova explosion resulting in a NS and a high-mass companion. Prior to the supernova of the companion, there is typically a period of mass transfer from the companion to the NS and the system can be detected as a high-mass X-ray binary. Eventually, the companion will undergo a supernova explosion, leaving behind two NSs: the older might be detected as a mildly recycled pulsar which was spun up by accretion from the progenitor of the younger star, and the younger might be detected as a normal pulsar. In the rare case that the system survives both supernovae, the result is a DNS (see Lorimer 2008 and references therein).

In this letter, we report the timing solution for PSR J0453+1559, a pulsar discovered in the Arecibo 327 MHz Drift Pulsar Survey (Deneva et al., 2013). At the time of writing has discovered this survey has discovered a total of 62 pulsars and rotating radio transients. As reported by Deneva et al. (2013), PSR J0453+1559 has a spin period of 45.7 ms, a dispersion measure (DM) of 30.3 pc cm^{-3}, an orbital period of 4.07 days and a massive companion.

In Section 3.2, we describe the observations, data reduction, and the derivation of the timing solution. In Section 3.3, we present the timing parameters of this new system. In Section 3.4, we conclude with a discussion of the significance of the timing parameters.

Table 3.1. Double neutron star systems known in the Galaxy

Pulsar	Period (ms)	P_b (days)	x (lt-s)	e	M_T ($M_\odot$)	M_p ($M_\odot$)	M_c ($M_\odot$)	References
J0737−3039A	22.699	0.102	1.415	0.0877775(9)	2.58708(16)	1.3381(7)	1.2489(7)	1
J0737−3039B	2773.461	...	1.516	...	...	...	...	...
J1518+4904	40.935	8.634	20.044	0.24948451(3)	2.7183(7)	...	...	2
B1534+12	37.904	0.421	3.729	0.27367740(4)	2.678463(4)	1.3330(2)	1.3454(2)	3
J1753−2240	95.138	13.638	18.115	0.303582(10)	...	...	...	4
J1756−2251	28.462	0.320	2.756	0.1805694(2)	2.56999(6)	1.341(7)	1.230(7)	5
J1811−1736	104.1	18.779	34.783	0.82802(2)	2.57(10)	...	...	6
J1829+2456	41.009	1.760	7.236	0.13914(4)	2.59(2)	...	...	7
J1906+0746*	144.073	0.166	1.420	0.0852996(6)	2.6134(3)	1.291(11)	1.322(11)	8
B1913+16	59.031	0.323	2.342	0.6171334(5)	2.8284(1)	1.4398(2)	1.3886(2)	9
J1930−1852	185.520	45.060	86.890	0.39886340(17)	2.59(4)	...	...	10
J0453+1559	45.782	4.072	14.467	0.11251832(4)	2.734(3)	1.559(5)	1.174(4)	This letter
Globular cluster systems								
J1807−2500B*	4.186	9.957	28.920	0.747033198(40)	2.57190(73)	1.3655(21)	1.2064(20)	12
B2127+11C	30.529	0.335	2.518	0.681395(2)	2.71279(13)	1.358(10)	1.354(10)	13

Refrecenes: (1) Burgay et al. (2003) and Kramer et al. (2006), (2) Janssen et al. (2008), (3) Wolszczan (1991) and Fonseca et al. (2014), (4) Keith et al. (2009), (5) Faulkner et al. (2005) and Ferdman et al. (2014), (6) Corongiu et al. (2007), (7) Champion et al. (2004) and Champion et al. (2005), (8) Lorimer et al. (2006) and van Leeuwen et al. (2015), (9) Hulse & Taylor (1975) and Weisberg et al. (2010) (10)Swiggum et al. (2015), 12: Lynch et al. (2012), 13: Anderson et al. (1989) and Jacoby et al. (2006) * Note. There is some uncertainty on whether these systems are DNSs.

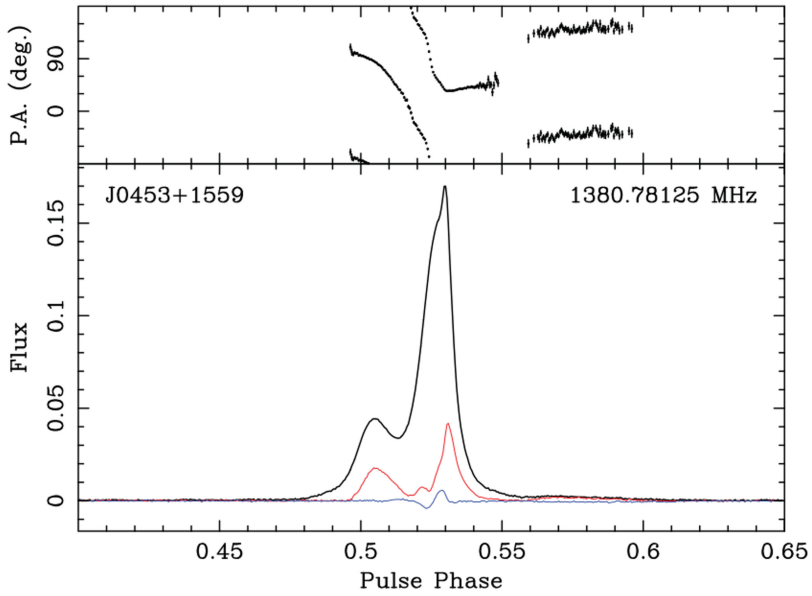

Figure 3.1. Pulse profile for PSR J0453+1559 at L-band (1170-1730 MHz), obtained by averaging the best detections of the pulsar. The black line indicates total intensity, the red line is the amplitude of linear polarization and the blue line is the amplitude of the circular polarization. In the top panel, we depict the position angle of the linear polarization, where a clear polarization swing and a sudden jump between orthogonal modes is clearly visible.

3.2 Observations and Data Reduction

PSR J0453+1559 was observed with the L-wide receiver of the 305-m Arecibo radio telescope 45 times over 2.5 years using the Puerto Rico Ultimate Pulsar Processing Instrument (PUPPI, a clone of the Green Bank Ultimate Pulsar Processing Instrument, GUPPI)[1] as a back-end, which allows simultaneous processing of the $\Delta f = 600$ MHz bandwidth provided by the receiver (from 1130 to 1730 MHz) with a system temperature $T_{\rm sys} = 30$ K and a gain $G = 10$ K/Jy. The first six months' observations were taken in search mode with 2048 channels, a time resolution $T_{\rm res}$ of 40.96 μs, two polarizations ($n_p = 2$) and basically no sensitivity degradation due to digitization ($\beta \simeq 1$), since PUPPI digitizes the antenna voltages with 8 bits. After derivation of a phase-connected timing solution, these were dedispersed and folded using `DSPSR`[2], (van Straten & Bailes 2011), producing 1024-bin profiles.

This initial timing ephemeris made it possible to conduct all of the subsequent observations in coherent fold mode (with 512 channels, 2048 phase bins, and 4 Stokes parameters), which coherently dedisperses and folds the data online, optimally removing the dispersive effects of the interstellar medium. These observations have improved the signal-to-noise ratio (S/N) because they benefit from the better pointing position derived from the timing solution. The pulse profile is displayed in Figure 3.1. The main pulse has a sharp feature that contributes significantly to the good timing precision of this pulsar discussed in Section 3.3.

The dedispersed pulse profiles obtained when averaging the 11-minute blocks of timing data

[1] http://safe.nrao.edu/wiki/bin/view/CICADA/GUPPISupportGuide
[2] http://dspsr.sourceforge.net/

produced by PUPPI are then calibrated using the noise diode observations that are taken with (almost) every single observation. The resulting calibrated pulse profiles are then cross-correlated with the low-noise template displayed in Fig. 3.1 using the procedure described in Taylor (1992) and implemented in the `PSRCHIVE` software (Hotan et al. 2004; van Straten et al. 2012). This resulted in 868 usable topocentric pulse times of arrival (TOAs).

We then used `TEMPO`[3] to correct the TOAs using the Arecibo telescope's clock corrections and to convert them to the Solar System barycenter. To do this, the motion of the radio telescope relative to the Earth was calculated using the data from the International Earth Rotation Service, and to the barycenter using the DE421 solar system ephemeris[4]. Finally, the difference between the measured TOAs and those predicted by a model of the spin and the orbit of the pulsar is minimized by `TEMPO`, by varying the parameters in the model. The parameters that best fit the data are presented in the first column of Table 3.2. To model the orbit, we used the DDGR model described by Damour & Deruelle (1985) and Damour & Deruelle (1986), which assumes the validity of GR in the description of the orbital motion of the system and uses as parameters the total mass of the system M and the companion mass M_c.

The residuals (TOAs minus model predictions) associated with this DDGR model are displayed in Figure 3.2. There are some short-term trends in the residuals that point toward unmodeled systematics. For this reason, we added 2.5 μs (the approximate amplitude of these systematics) in quadrature to the TOA uncertainties, and this way the reduced χ^2 is close to 1.0 both for TOAs with large and small uncertainties. The amplitude of the systematics is smaller for the data with polarization calibration, which suggests imperfect polarization calibration might be a cause of the systematics in the uncalibrated data. The residual root mean square is 4 μs, which represents a fraction of 8.7×10^{-5} of the spin period.

In order to double check the results, we used `TEMPO2` (Hobbs et al. 2006 & Edwards et al. 2006) and the DDH model described by Freire & Wex (2010), which like the DD (but unlike the DDGR model) allows a theory-independent fit for the detectable post-Keplerian (PK) parameters: in this case, the rate of advance of periastron ($\dot{\omega}$) and two parameters that provide an optimized description of the Shapiro delay, the orthometric amplitude (h_3) and the orthometric ratio (ς). As we will see, the measurement of the PK parameters is important because it allows an understanding of the precision of the mass measurements derived from the DDGR model and also a double check on its accuracy.

3.3 Results

The pulsar's ephemeris in Table 3.2 includes a precise position in the sky, which allows for optical follow-up. No optical counterpart to the system is detectable in the online DSS2 optical survey, either in the red or blue filters, or in the 2MASS survey.

We can detect the proper motion in RA, and have useful limits for the proper motion in Declination. We can derive a total proper motion $\mu = (7.0 \pm 2.5)\,\mathrm{mas\,yr^{-1}}$. The ephemeris also includes the pulsar's spin period (P) and its derivative ($\dot{P}$). Taking into account the effect of the proper motion (Shklovskii 1970) and Galactic acceleration (Damour & Taylor 1991) on $\dot{P}$ at the DM-derived distance of ~1.1 kpc, we obtain an intrinsic $\dot{P}$ of $1.77(2)\times10^{-19}$ s s^{-1}. From this, we derive a characteristic age of 4.1×10^9 years and a surface inferred magnetic field of 2.9×10^9 G. These numbers are similar to what we observe for other recycled pulsars with

[3] http://tempo.sourceforge.net/

[4] ftp://ssd.jpl.nasa.gov/pub/eph/planets/ioms/de421.iom.v1.pdf

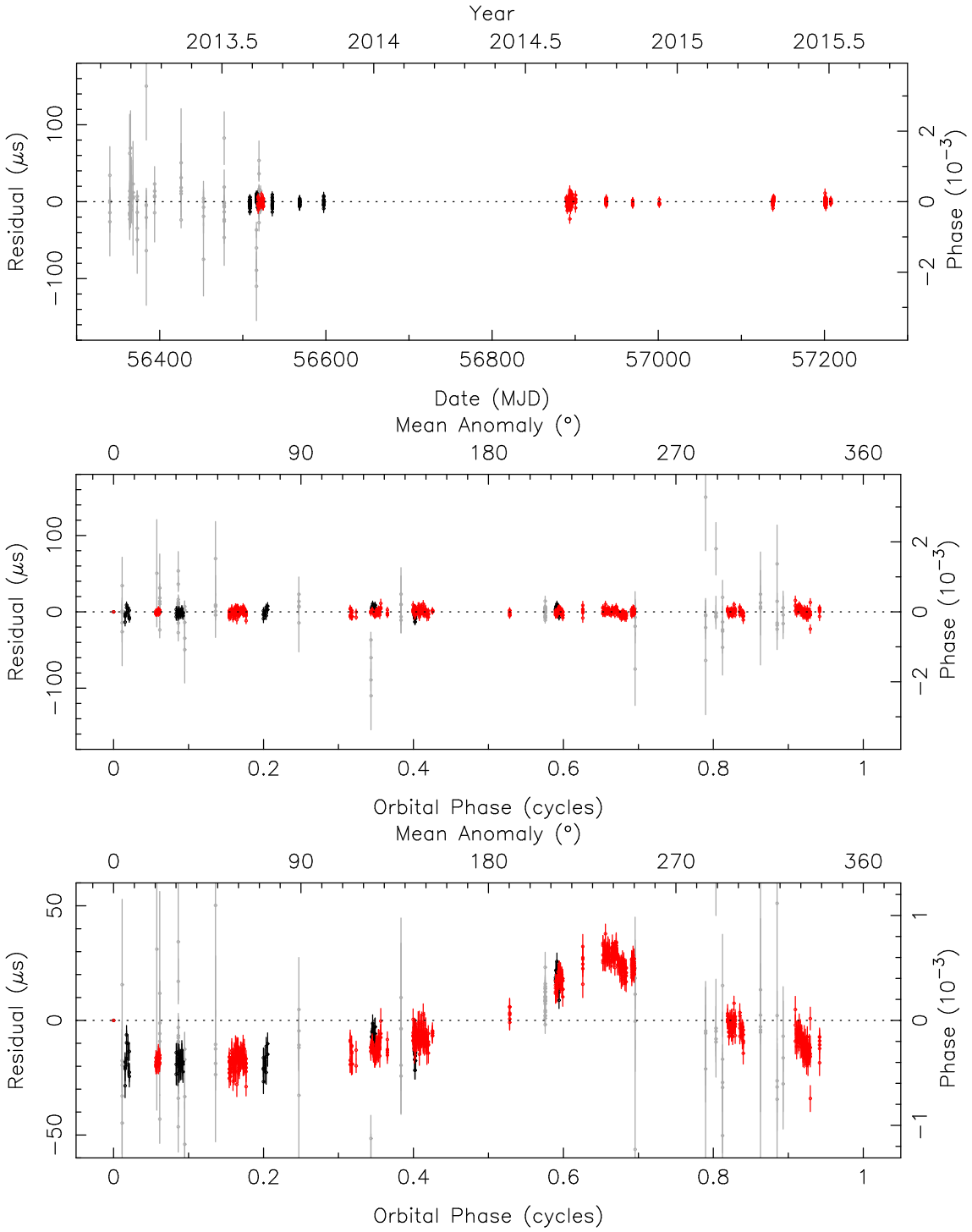

Figure 3.2. The top plot is the timing solution for PSR J0453+1559, timing residuals (measured pulse arrival times - model pulse arrival times) as a function of MJD. The middle and bottom plot show the timing residuals versus orbital phase of the J0453+1559 system. The bottom plot shows the magnitude of the Shapiro Delay as a function of orbital phase, derived with the same Keplerian orbital parameters from the DDGR ephemeris in Table 3.2. The color of the timing residuals are categorized by: gray is search mode data, black is coherent fold mode that is not calibrated data, and red is coherent fold mode calibrated data.

Table 3.2. Timing Solution for PSR J0453+1559

Timing Parameters for PSR J0453+1559		
Fitting program	TEMPO	TEMPO2
Time units	TDB	TCB
Solar system ephemeris	DE421	DE421
Reference epoch (MJD)	56400	56400
Span of timing data (MJD)	56339-57207	56339-57207
Number of TOAs	868	868
rms residual (μs)	3.96	3.88
Solar n_0 (cm^{-3})	0.0	0.0
Right Ascension (RA), α (J2000)	04:53:45.41372(4)	04:53:45.41368(5)
Declination, δ (J2000)	+15:59:21.3055(50)	+15:59:21.3063(59)
Proper motion in RA, μ_α (mas yr^{-1})	−5.4(4)	−5.5(5)
Proper motion in DEC, μ_δ (mas yr^{-1})	−5.3(3.6)	−6.0(4.2)
Pulsar period, P (s)	0.045781816163093(3)	0.0457818168729515(33)
Period derivative, $\dot{P}$ ($10^{-18}\mathrm{ss}^{-1}$)	0.18616(7)	1.8612(8)
Dispersion measure, DM ($\mathrm{pc\ cm}^{-3}$)	30.30527(26)	30.3053(3)
Binary Parameters		
Orbital model	DDGR	DDH
Orbital period, P_b (days)	4.072468588(4)	4.072468649(4)
Projected semi-major axis of the pulsar orbit, x (lt-s)	14.466798(5)	14.4667896(42)
Epoch of periastron, T_0 (MJD)	56344.0029907(6)	56344.0031965(9)
Orbital eccentricity, e	0.11251832(4)	0.11251844(8)
Longitude of periastron, ω (°)	223.06953(6)	223.06965(8)
Relativistic Parameters and Masses		
Rate of advance of periastron, $\dot{\omega}$ ($^\circ\mathrm{yr}^{-1}$)	0.0379412 (d)	0.03793(3)
Orthometric amplitude, h_3 (μs)	-	3.07(25)
Orthometric ratio, ς	-	0.709(40)
Total mass, M ($\mathrm{M}_\odot$)	2.734(4)	2.733(4) (d)
Companion mass, M_c ($\mathrm{M}_\odot$)	1.174(4)	1.172(4) (m)
Derived Parameters		
Mass function, f ($\mathrm{M}_\odot$)	0.19601284(22)	0.19601248(4)
Pulsar mass, M_p ($\mathrm{M}_\odot$)	1.559(5)	1.560(5) (m)
Orbital inclination, i (°)	75.2699	$75.7^{+0.7}_{-0.8}$ (m)
Galactic longitude, l	184.1245	
Galactic latitude, b	−17.1369	
DM-derived distance, d (kpc)	1.1	
Galactic height, z (kpc)	−0.29	
Transversal velocity, $v_\perp$ ($\mathrm{km\ s}^{-1}$)	40	
Kinematic correction to $\dot{P}$, ($10^{-18}\mathrm{ss}^{-1}$)	0.0089	
Intrinsic $\dot{P}$, ($10^{-18}\mathrm{ss}^{-1}$)	$\simeq$0.177(2)	
Surface magnetic field strength, B_0 (10^9 Gauss) ..	2.9	
Characteristic age, τ_c (Gyr)	4.1	

Notes. Numbers in parentheses represent 1-σ uncertainties in the last digits as determined by `TEMPO`, scaled such that the reduced $\chi^2 = 1$. Note that the timing parameters are given in two different timescales, TDB and TCB. (d) indicates a parameter that is derived in one model, but fitted directly in the other. (m) parameter derived from the Bayesian analysis described in the text. The distance is derived from the DM using the Cordes & Lazio (2002) model of the Galactic electron density with a ∼25% uncertainty.

massive companions, and they indicate that this pulsar was mildly recycled by the accretion of matter from the progenitor of the current companion star (Tauris et al. 2012).

The ephemeris also includes very precise orbital parameters. The orbital period P_b is 4.07 days, i.e., this is not a tight system where we might be able to measure the remaining PK parameters precisely: the Einstein delay (γ) will take a long time to measure and it will correlate strongly with the kinematic $\dot{x}$ term that arises from the proper motion (Arzoumanian et al. 1996 & Kopeikin 1996); the orbital decay due to the emission of gravitational waves ($\dot{P}_{\rm b}$) will be extremely small and masked by much larger kinematic contributions (Shklovskii 1970 & Damour & Taylor 1991). The projected semi-major axis of the pulsar's orbit x is 14.5 lt-s; from this, we can derive the Keplerian mass function:

$$f(M_p, M_c) = \frac{(M_c \sin i)^3}{(M_p + M_c)^2} = \frac{4\pi^2 x^3}{T_\odot P_b^2} = 0.1960128(2)\,{\rm M}_\odot, \tag{3.1}$$

where $T_\odot = G{\rm M}_\odot {\rm c}^{-3} = 4.925490947\mu$s is a solar mass ($\rm M_\odot$) in time units ($c$ is the speed of light and G is Newton's gravitational constant), i is the angle between the plane of the orbit and the plane of the sky, and the pulsar and companion masses M_p and M_c, are in solar masses. If we assume a mass of 1.4 $\rm M_\odot$ for the pulsar and maximum and median orbital inclinations ($i = 90°, 60°$), then we obtain minimum and median companion masses of 1.05 and 1.30 $\rm M_\odot$, i.e., the companion is relatively massive.

Given the orbital eccentricity ($e = 0.11$), the companion is very likely to be an NS – if it had evolved into a massive white dwarf star, then there would be no sudden mass loss associated with a supernova explosion and the system would have retained the circular orbit that is characteristic of compact accreting systems. This is consistent with the non-detection of an optical counterpart of the system in any of the optical catalogs. However, the high eccentricity does not entirely settle the matter: the recent discovery of a recycled pulsar with a massive ($\sim 1{\rm M}_\odot$) companion PSR J1727−2946 Lorimer et al. (2015) and an orbital eccentricity of 0.0456 bridges the previously observed eccentricity gap between systems with NS and massive WD companions. In the remainder of this paper, we will assume, with caution, that the companion is an NS.

The pulsar's orbital eccentricity allows a detection of the advance of periastron, $\dot{\omega}$. If both components are compact, as is implied by the optical non-detection, then this is given by

$$\dot{\omega} = \dot{\omega}_{\rm GR} + \dot{\omega}_{\rm K}. \tag{3.2}$$

The second term $\dot{\omega_{\rm K}}$ is caused by the change in viewing geometry due to the proper motion μ (Damour & Taylor 1991):

$$|\dot{\omega}_{\rm K}| = \left| \frac{\mu}{\sin i} \cos(\Theta_\mu - \Omega) \right| \leq 3.65 \times 10^{-6}\,{\rm deg\ yr}^{-1}, \tag{3.3}$$

where Θ_μ is the position angle (PA) of the proper motion and Ω is the PA of the line of nodes (the intersection of the orbital plane with the plane of the sky). This term is currently one order of magnitude smaller than the experimental uncertainty in the measurement of $\dot{\omega}$. Thus $\dot{\omega}_{\rm GR} \simeq \dot{\omega}$.

The first term depends only on the Keplerian orbital parameters, which are already known precisely, and the total mass of the binary M. Thus, M can be derived from a measurement of

$\dot{\omega}_{\rm GR}$ (Weisberg et al. 1981):

$$M = \frac{1}{T_\odot}\left[\frac{\dot{\omega}_{\rm GR}}{3}(1-e^2)\right]^{\frac{3}{2}}\left(\frac{P_{\rm b}}{2\pi}\right)^{\frac{5}{2}}. \tag{3.4}$$

This yields $M = 2.734 \pm 0.003\,{\rm M}_\odot$. As we can see in Table 3.1, this is within the mass range of currently known DNS systems.

We also measure the Shapiro delay with some precision. In the DDH solution, h_3 and ς are measured with 10 and 17σ significance. This in principle allows a measurement of the system masses using the Shapiro delay alone.

In order to estimate the masses from the Shapiro delay, we sampled the quality of the fit for a wide region in the $M_c - \cos i$ plane, depicted in the left panel of Figure 3.3. For each point in this plane, we calculate the Shapiro delay parameters assuming GR to be the correct theory of gravity and then introduce them into the timing solution, keeping them fixed and fitting for all other timing parameters. The quality of the fit is quantified by the χ^2 of the resulting solution; the lower this is, the better the fit. From this χ^2 map, we derive a two-dimensional (2D) probability distribution function (pdf) using the Bayesian specification in Splaver et al. (2002). This is then converted to a similar 2D pdf in the $M_c - M_p$ plane (right panel) using eq. 3.1. The black contours of both panels include 68.27% and 95.45% of the total probability of each pdf. We then marginalize the 2D pdfs to derive one-dimensional (1D) pdfs for M_c, $\cos i$ and M_p, the latter are presented in the top and right panels in black. They allow for a wide (and rather un-interesting) range of masses for the pulsar and the companion, i.e., just by itself, the Shapiro delay does not provide useful mass constraints.

The precision of these mass estimates increases by two orders of magnitude if for each point in the $M_c - \cos i$ plane we fix the Shapiro delay parameters *and* assume that $\dot{\omega}$ is due only to the effects of GR (using eq. 3.4). As before, we then fit for all other timing parameters, store the values of χ^2, and calculate a second 2D pdf. The latter is illustrated in Figure 3.3 by the red regions, which include 95.4% of its total probability. Marginalizing this second pdf along the different axes, we obtain for the medians and 1σ percentiles the following values: $M_p = 1.559 \pm 0.005\,{\rm M}_\odot$, $M_c = 1.172 \pm 0.004\,{\rm M}_\odot$ and $i = 75.7^{+0.7}_{-0.8}$ °, respectively. This is consistent with the masses provided by the DDGR model in `TEMPO`.

3.3.1 Search for the Companion as a Radio Pulsar

In order to search for radio pulsations from the companion, we used the early observations, which were taken in search mode. The precise measurement of the masses of the two NSs in the system allows us to derive a complete ephemeris for the companion NS, except for the spin parameters and ω, to which we add 180°. This ephemeris was used to resample the time series (dedispersed at the DM of the known pulsar) for the reference frame of the companion. This way, we removed any possible losses in sensitivity due to the companion acceleration. We then used the PRESTO pulsar search code[5] to search for periodic signals in the resampled time series, and used it to fold all of the candidates, which were then inspected visually. No pulsations coming from the companion were detected.

To estimate the upper limit on the companion's pulsed mean flux density in our line of sight, $S_{\rm max}$, we used the radiometer equation (Lorimer & Kramer 2004), using the parameters of

[5] http://www.cv.nrao.edu/∼sransom/presto/

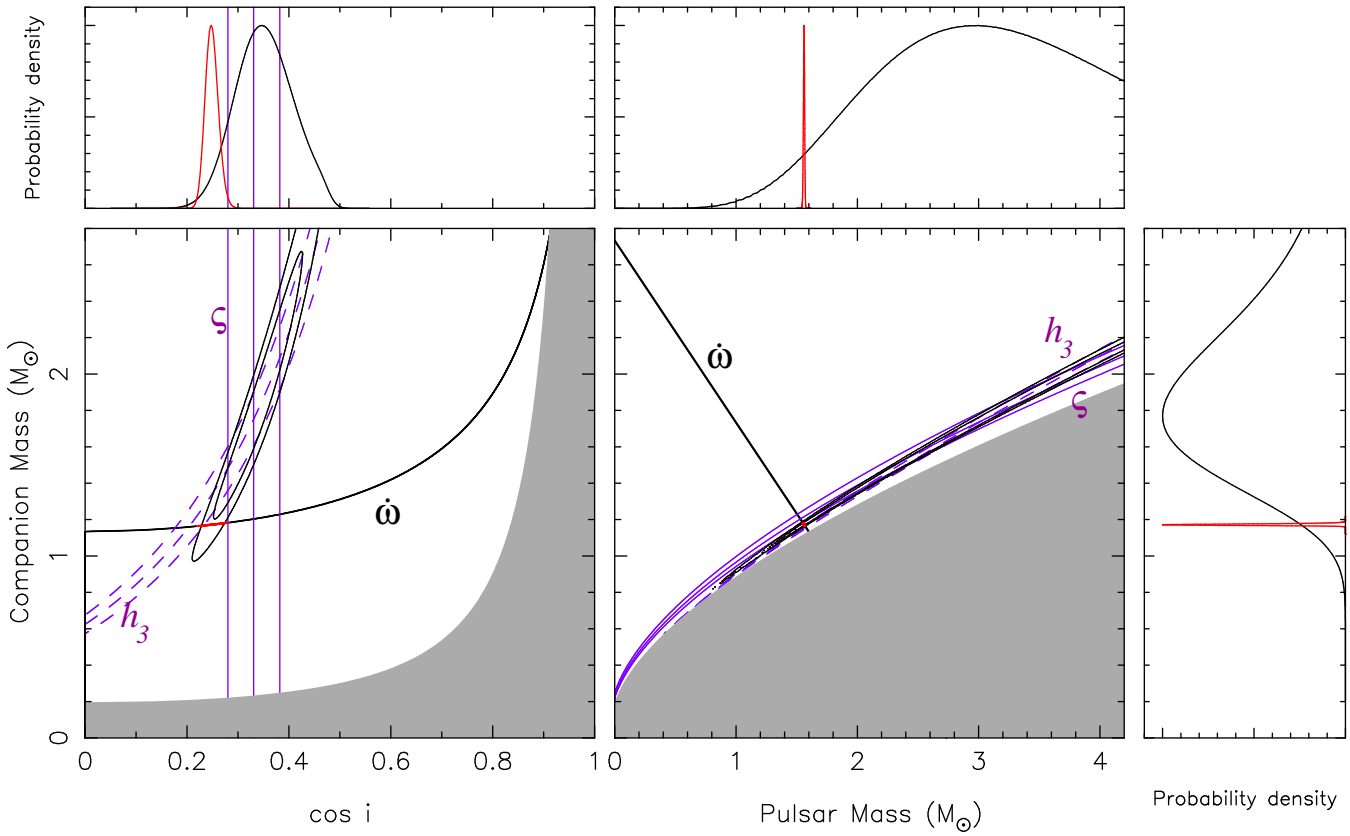

Figure 3.3. Current constraints from the timing of PSR J0453+1559. Each triplet of lines corresponds to the nominal and $\pm 1\sigma$ uncertainties of the post-Keplerian parameters measured using the DDH model in TEMPO2 (see Table 3.2), which are the rate of advance of periastron $\dot{\omega}$, the orthometric ratio of the Shapiro delay ς, and the orthometric amplitude of the Shapiro delay, h_3 (Freire & Wex, 2010). The contour levels contain 68.27% and 95.45% of the 2D probability density functions (pdfs) derived from the quality of the timing solution at each point of the $M_c - \cos i$ plane using only the Shapiro delay (black) and Shapiro delay plus the assumption that the $\dot{\omega}$ is due only to the effects of GR (red). *Left*: $M_c - \cos i$ plane. The gray region is excluded by the physical constraint $M_p > 0$. *Right*: $M_c - M_p$ plane. The gray region is excluded by the mathematical constraint $\sin i \leq 1$. *Top and right panels*: pdfs for $\cos i$, M_p and (on the right) M_c, derived from marginalizing the 2D pdf in the main panel for these quantities. When $\dot{\omega}$ is taken into account (red), the precision of the mass estimates improves by two orders of magnitude.

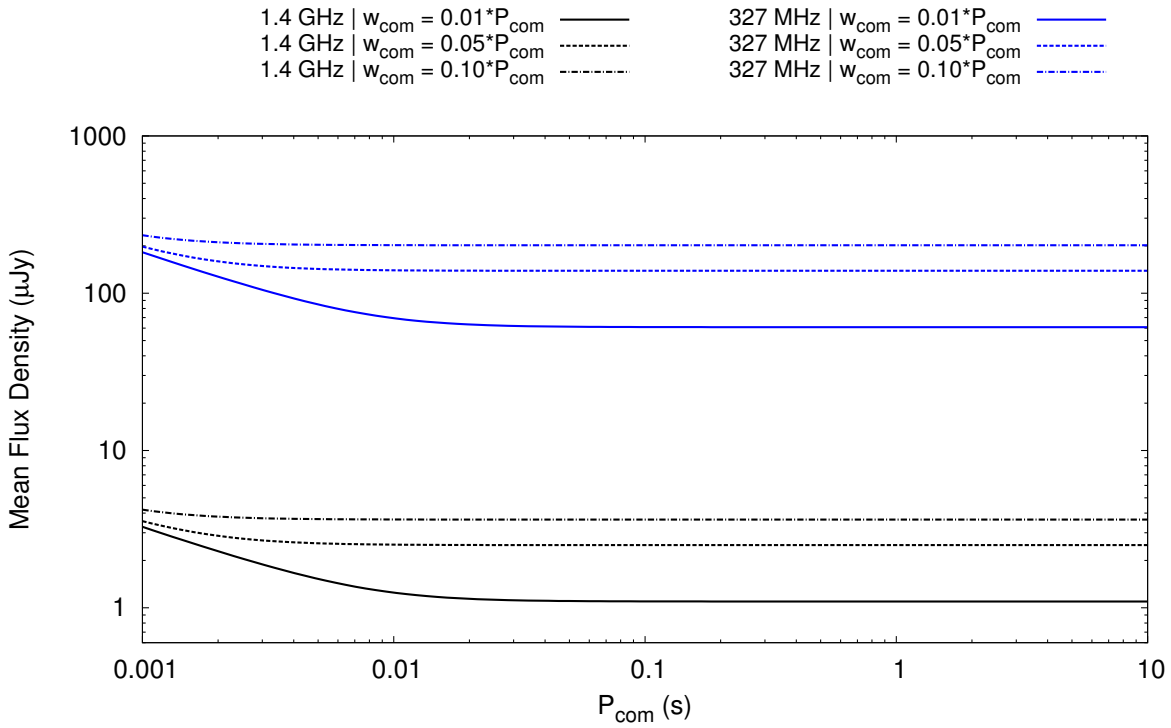

Figure 3.4. Estimated minimum mean flux density of the companion if detectable with an S/N = 10, as a function of its spin period $P_{\rm com}$ at 1.4 GHz (black lines) and 327 MHz (blue lines). For each frequency, the cases of an intrinsic duty cycle $w_{\rm com}$ of 1% (solid line), 5% (dashed line), and 10% (dotted dashed line) of $P_{\rm com}$ are shown. In L-band, the parameters used were $t_{\rm obs} = 6300$ s, $T_{\rm sys} = 30$ K, $G = 10$ K/Jy, $\Delta f = 600$ MHz; at 327 MHz they were $t_{\rm obs} = 240$ s, $T_{\rm sys} = 113$ K, $G = 11$ K/Jy, $\Delta f = 60$ MHz; at both frequencies $\beta = 1$ and $n_p = 2$. Because the companion was not detected, its mean flux density must be towards out of our line of sight.

the search observations and accounting for dispersive smearing at the DM of the system and a minimum S/N of 10. For L-band observations, the parameters are those reported in Section 3.2, whereas at 327 MHz we have $T_{\rm sys} = 113$ K, $G = 11$ K/Jy, and $\Delta f = 60$ MHz. In the L-band, the longest observation had a length of $t_{\rm obs} = 6300$ s, whereas for only the 327 MHz observation available to us $t_{\rm obs} = 240$ s.

Figure 3.4 shows $S_{\rm max}$ as a function of the unknown companion spin period, $P_{\rm com}$, for intrinsic duty cycles of 1%, 5% and 10%. For the range of expected spin periods of the companion ($P_{\rm com} \gtrsim 0.1$ s), $S_{\rm max,1400} \lesssim 4\,\mu$Jy, and $S_{\rm max,327} \lesssim 202\,\mu$Jy. Given the estimated distance of 1.0 kpc, these translate into pseudo-luminosities of $L_{\rm max,1400} \lesssim 4\,\mu$Jy kpc^2 and $L_{\rm max,327} \lesssim 202\,\mu$Jy kpc^2, respectively. No pulsar in the ATNF catalog[6] has an estimated L_{1400} as low as this.

3.4 Discussion and Conclusions

The accretion episode in DNS systems is very short-lived and therefore the mass of the recycled pulsar is only slightly larger than its mass at birth (Tauris et al. 2015). Until now, most well-measured NS masses in DNS systems fell in a narrow range between 1.23 and 1.44 $M_\odot$

[6] http://www.atnf.csiro.au/people/pulsar/psrcat/

(Weisberg et al. 2010 and Faulkner et al. 2005, see Table 3.1). This has led to speculation that all NSs might be born within this narrow band, and that the large masses observed in some MSPs like PSR J1903+0327 (Freire et al. 2011), PSR J1614−2230 (Demorest et al. 2010), and PSR J0348+0432 (Antoniadis et al. 2012) are due to accretion. However, from an analysis of the evolution of PSR J1614−2230, Tauris et al. (2011) had already suggested that at least some NSs must be born more massive than 1.44 $M_\odot$. The mass of PSR J0453+1559 - the largest ever measured in a DNS system (see Table 3.1) - and that of its companion − the smallest precisely measured for *any* NS − shows that the range of NS birth masses is indeed substantially wider than earlier studies indicated (Thorsett et al. 1999 & Özel et al. 2012).

It is interesting to speculate on how the companion might have formed. Its mass is lower than the 1.24 $M_\odot$ measured for the companion of J1756−2251 (Ferdman et al. 2014) and PSRs J1802−2124 (Ferdman et al. 2010) and J0737−3039B (Kramer et al. 2006) that are thought to have formed in electron capture supernovae (ECSN). It is possible that the companion formed instead in an iron core collapse SN, where the core of the progenitor of the companion was stripped of its envelope (Tauris et al., 2015).

The relatively small eccentricity of the system compared to other DNS systems (see Table 3.1) suggests a relatively small SN kick velocity at birth, which is consistent both with formation via ECSN and an ultra-stripped iron core SN. In this case, the three-dimensional (3D) velocity of the system in the Galaxy should be small in comparison with the general pulsar population. This is consistent with the inferred transverse velocity of ~ 40 km s^{-1} and the relatively small Galactic height of the system, 0.29 kpc.

The mass asymmetry is also important because it leads to a peculiar behavior during NS−NS mergers, particularly if the mass ratio is less than 0.8. During the merger, the lighter (and larger) NS is tidally disrupted by the smaller, more massive NS. According to recent simulations (Rezzolla et al. 2010, Hotokezaka et al. 2013, and Rosswog (2013)), such mergers result in a much larger release of heavy r-process elements into space (Just et al. 2015), possibly explaining the heavy element abundances in our Galaxy. However, asymmetric DNSs can explain heavy element abundances if they form with an orbital period that is small enough for them to merge well within a Hubble time. Pulsar J0453+1559 has a very large merger time, 1.43 Tyr. However, the mass asymmetry measured in this system opens up the possibility that similar asymmetries might eventually be measured for compact DNSs in the future.

This result is also important for searches of gravitational wave emission from NS−NS mergers using ground-based GW detectors (Abbott et al. 2009 and Abadie et al. 2012) − it shows that we should not assume that the components of DNS systems have similar masses. This result justifies particularly searching for DNS systems with lighter NSs, where more computational effort is required, since in this case the inspiral episodes leading to the merger are significantly longer.

In asymmetric DNSs, dipolar gravitational wave emission could theoretically become important at the later stages of the merger; however, this possibility is already significantly constrained by the measurement of the orbital decay of PSR J1738+0333 (Freire et al. 2012) and J0348+0432 (Antoniadis et al. 2013), at least in the framework of Scalar-Tensor theories of gravity. Therefore, GR-derived templates should be a satisfactory approximation to the merger signal of asymmetric DNSs.

Chapter 4

Pulsar J1411+2551: A Low Mass Double Neutron Star System

This chapter is based on an article published in the Astrophysical Journal (Martinez et al., 2017). The article can be found online at: https://iopscience.iop.org/article/10.3847/2041-8213/aa9d87/meta

I am the lead author of the article. My main contributions include the follow-up of this PSR J1411+2551. I performed the observations, processed the data, and performed the timing analysis. The text, figures, and tables have only been modified to match the style and format of this thesis.

The full list of authors is:
J.G. Martinez, K. Stovall, P.C.C. Freire, J.S. Deneva, T.M. Tauris, A. Ridolfi, N. Wex, F.A. Jenet, M.A. McLaughlin, M.Bagchi

Abstract

In this chapter, we report the discovery and characterization of PSR J1411+2551, a new binary pulsar discovered in the Arecibo 327 MHz Drift Pulsar Survey. Our timing observations of the radio pulsar in the system span a period of about 2.5 years. This timing campaign allowed a precise measurement of its spin period (62.4 ms) and its derivative $(9.6 \pm 0.7) \times 10^{-20}\,\mathrm{s\,s^{-1}}$; from these we derive a characteristic age of $> 9.1\,\mathrm{Gyr}$ and a surface magnetic field strength of $< 2.6 \times 10^9$ G. These numbers indicate that this pulsar was mildly recycled by accretion of matter from the progenitor of the companion star. The system has an eccentric ($e = 0.17$) 2.61 day orbit. This eccentricity allows a highly significant measurement of the rate of advance of periastron, $\dot{\omega} = 0.07686 \pm 0.00046^\circ\ \mathrm{yr}^{-1}$. Assuming general relativity accurately models the orbital motion, this implies a total system mass $M = 2.538 \pm 0.022\,\mathrm{M}_\odot$. The minimum companion mass is $0.92\,\mathrm{M}_\odot$ and the maximum pulsar mass is $1.62\,\mathrm{M}_\odot$. The large companion mass and the orbital eccentricity suggest that PSR J1411+2551 is a double neutron star system; the lightest known to date including the DNS merger GW170817. Furthermore, the relatively low orbital eccentricity and small proper motion limits suggest the second supernova had a relatively small associated kick; this and the low system mass suggest it was an ultra-stripped supernova.

4.1 Introduction

The first double neutron star (DNS) system, PSR B1913+16, was discovered in 1974 by Hulse & Taylor (1975). Continued timing of this system resulted in a measurement of the orbital decay due to the emission of gravitational waves as predicted by general relativity (GR). This was the

first detection (albeit an indirect one) of gravitational waves, almost 40 years before LIGO's direct detection (Abbott et al., 2016).

Since then, 16 additional DNS systems have been discovered in the Galaxy (Tauris et al., 2017), including one system in which both neutron stars (NSs) have been detected as radio pulsars, PSRs J0737−3039A and B (Burgay et al., 2003; Lyne et al., 2004). This system has an orbital period of only 2.4 hr and with the presence of two radio pulsed signals, it is a unique laboratory for tests of GR and alternative theories of gravity in the strong-field regime (Kramer et al., 2006). The discovery of DNS systems stimulated the construction of ground-based interferometric detectors of gravitational waves sources and helped in statistical predictions of the collision rate of DNS systems (e.g. Kim et al., 2015, and references therein), many years prior to the recent detection of GW170817 (Abbott et al., 2017).

DNSs are fossils, preserving the endpoints of an exotic long journey of stellar evolution and binary interactions. By probing the distribution of NS masses, proper motions, orbital periods, and eccentricities of DNSs and even, in some cases, the misalignment angle between the NS and the orbital angular momentum (e.g., Ferdman et al. 2013), we can obtain crucial information from their past evolution; this provides important clues on the nature of supernovae and NS formation, as well as binary star interactions (Tauris et al., 2017).

These systems begin as binaries consisting of two massive main-sequence (MS) stars. In time, the more massive star will undergo dramatic envelope expansion and eventually a supernova (SN) explosion. This results in a system consisting of a NS and a high-mass MS companion. As the companion evolves and extends its envelope, there will be a phase of mass transfer onto the NS; binaries in this evolutionary stage can be detected as high-mass X-ray binaries (HMXBs; Casares et al., 2017). At this stage, the orbit is circularized by tidal forces. Eventually, following a common-envelope in-spiral and a new mass-transfer phase, the companion undergoes a SN explosion as well, forming a second NS (see, e.g., Tauris & van den Heuvel, 2006; Lorimer, 2008). DNS systems that have a relatively small measured eccentricity ($e < 0.2$) are presumed to have underwent an ultra-stripped SN with small ejecta mass and often small kicks (Tauris et al., 2017).

In such a system, the older NS might be detected as a mildly recycled pulsar (spin periods of tens of ms and relatively small magnetic field $10^9 - 10^{10}$ G) which was spun up by accretion from the progenitor of the younger NS. The younger NS itself might be detected as a normal pulsar, with a high magnetic field ($10^{10} - 10^{13}$ G) and, in most cases, a much slower rotation. If the two NSs remain bound after the second SN, they form a DNS. The system's orbit will almost inevitably be eccentric, given the mass loss and the SN kick and the impossibility of tidal circularization after formation of two compact objects.

Despite their importance for tests of gravity theories and NS mass measurements, the 16 DNSs currently known represent a tiny fraction of the more than 2600 pulsars currently known (Manchester et al., 2005). With such a small sample, the statistical properties of this population are still relatively poorly known. It is therefore important to find more of these systems. Finding new DNSs is among the top priorities of many recent pulsar surveys, like the Arecibo ALFA pulsar survey (Cordes et al., 2006), Green Bank North Celestial Cap (GBNCC) survey (Stovall et al., 2014), the HTRU-N (Barr et al., 2013b) and HTRU-S (Keith et al., 2010) surveys, the latter has been superseded by the SUPERB survey (Keane et al., 2017). All of these employ specialized acceleration search algorithms in an attempt to detect tight DNSs.

In this chapter, we report the discovery of PSR J1411+2551, a 62-ms pulsar found in data from another of these surveys, the Arecibo 327 MHz Drift Pulsar Survey, or AO327 (Deneva et al., 2013). At the time of writing, this survey has discovered a total of 75 pulsars and transients,

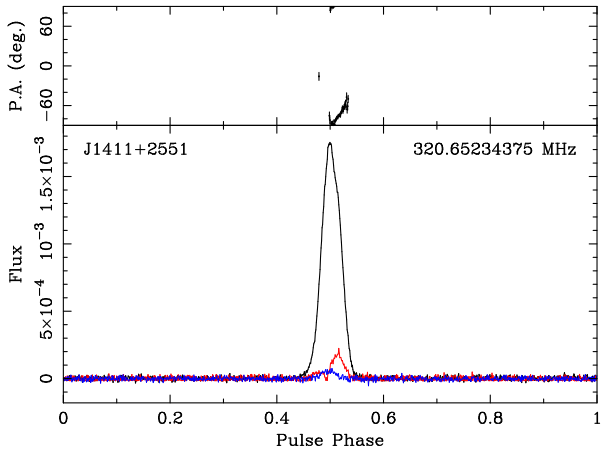

Figure 4.1. Polarimetric pulse profile for PSR J1411+2551 at the frequency of 327 MHz, for a total bandwidth of 50 MHz; this was obtained by averaging the best detections of the pulsar at this frequency. The black line indicates total intensity in arbitrary units, the red line is the amplitude of linear polarization and the blue line is the amplitude of the circular polarization, all displayed as a function of spin phase. In the top panel we display the position angle of the linearly polarized component.

which include PSR J2234+0611, a millisecond pulsar (MSP) with an eccentric orbit (Deneva et al., 2013; Antoniadis et al., 2016). Among the transients discovered are several rotating radio transients, but thus far no fast radio bursts (Deneva et al., 2016). One of the pulsars found in this survey, PSR J0453+1559, is a member of a DNS; this is currently the DNS with the largest mass asymmetry known (Martinez et al., 2015). As we will see below, PSR J1411+2551 is also a member of a DNS system; this is the second such system found by AO327.

The remainder of this paper follows as such: in Section 4.2 we describe the observations. In Section 4.3, we describe the derivation of the timing solution for this pulsar. We end in the conclusion (Section 4.4) with a discussion of our findings.

4.2 Timing Observations

PSR J1411+2551 was discovered on 2014 September 9 by one of us (KS) in data from the AO327 taken with the Puerto Rico Ultimate Pulsar Processing Instrument (PUPPI, a clone of the Green Bank Ultimate Pulsar Processing Instrument)[1]. These observations were done in the incoherent search mode with a bandwidth of $\Delta f = 50$ MHz (from 302 to 352 MHz), 512 channels, a sampling time of 64 μs and two polarizations, with only the total power from these being recorded. After the discovery and until 2015 October 18, the pulsar was reobserved regularly with the incoherent search mode with the same time and spectral resolution as in the discovery observation; however instead of just total intensity we recorded the four Stokes parameters.

After a gap of several months, we continued observing the pulsar from 2016 July 5 until 2017 June 11. These observations were taken in coherently dedispersed search mode, with a sampling time of 10 μs, as described by Martinez et al. (2015). Like the original search data, these data retain sensitivity to a possible pulsar signal from the companion NS and allow post-processing removal of radio frequency interference (RFI), but with much improved time resolution.

[1] http://safe.nrao.edu/wiki/bin/view/CICADA/GUPPISupportGuide

The subsequent analysis is also similar to that described in detail in Martinez et al. (2015). First, we fold all the data to obtain pulse profiles. These are then calibrated using the noise diode observations taken before each observation. Each profile is then corrected for the Faraday effect, which requires the measurement of the rotation measure (RM). This is obtained by using the `rmfit` routine of the `PSRCHIVE` software (Hotan et al., 2004; van Straten et al., 2012), which looks for the best-fitting RM value by maximizing the linearly polarized intensity of the frequency-averaged profile. In Figure 4.1 we show the result of the sum of the coherently dedispersed, Faraday-corrected profiles.

For each calibrated profiles, the individual pulse profiles are then cross-correlated with the template of Figure 4.1 using the procedure described in Taylor (1992) and implemented the `PSRCHIVE`. This produced 660 topocentric pulse times of arrival (TOAs). We then used `TEMPO`[2] to estimate the barycentric TOAs and then to estimate the pulsar model parameters by minimizing the root mean square (rms) of the timing residuals (calculated as the difference between the measured TOA and the model prediction for the same pulse). These parameters are presented in Table 4.1. We used the theory-independent DD binary model (Damour & Deruelle, 1985, 1986) to describe the orbital motion.

The TOAs were split into two subsets. The first set is the incoherent search mode observations and the second set are the coherently dedispersed search mode observations. Each sub-set of the TOA uncertainties were scaled using an EFAC parameter of 0.94 and 1.06 such that the reduced $\chi^2 = 1$ when each subset was fit independently of the others. The timing residuals are displayed in Figure 4.2. Their rms is 33 μs; this is a fraction of 5.2×10^{-4} of the spin period. No significant trends are detectable in the residuals, showing that the ephemeris in Table 4.1 provides a good description of the TOAs.

4.3 Results

The pulsar's ephemeris in Table 4.1 includes a precise sky position, which allows for optical follow-up. No optical counterpart to the system is detectable in the online DSS2 optical survey, either in the red or blue filters, nor in the 2MASS survey.

The ephemeris also includes precise measurements of the pulsar's spin period (P) and its derivative ($\dot{P}$). From $\dot{P}$, we subtract the term due to the difference in Galactic acceleration between the PSR J1411+2551 and the Solar System, $-1.3 \times 10^{-20}\,\mathrm{s\,s^{-1}}$ (McMillan, 2017), to derive a maximum intrinsic $\dot{P}_{\rm int} = 10.9 \times 10^{-20}\,\mathrm{s\,s^{-1}}$. From this we derive a minimum characteristic age $\tau_c = 9.1 \times 10^9$ years and a maximum surface inferred magnetic field of $B_0 = 2.6 \times 10^9$ G. These values can change significantly if we add the effects of the proper motion (Shklovskii, 1970): for a proper motion of 20 mas yr^{-1} (close to our upper limit), we would have $\dot{P}_{\rm int} = 4.9 \times 10^{-20}\,\mathrm{s\,s^{-1}}$, $\tau_c = 20 \times 10^9\,\mathrm{yr}$, and $B_0 = 1.8 \times 10^9$ G. This indicates that PSR J1411+2551 was recycled by accretion of mass from the progenitor of its companion (Tauris et al. 2012).

From the orbital period P_b (2.6 days) and the projected semi-major axis x (9.20 light seconds), we obtain the mass function:

$$f(M_p, M_c) = \frac{(M_c \sin i)^3}{M^2} = \frac{4\pi^2 x^3}{T_\odot P_b^2} = 0.1223893(9)\,\mathrm{M_\odot}, \tag{4.1}$$

where $T_\odot = G\mathrm{M_\odot c^{-3}} = 4.925490947\mu$s is the solar mass times Newton's gravitational constant

[2] `http://tempo.sourceforge.net/`

($GM_\odot$, a quantity known much more precisely than either G or $M_\odot$) divided by the cube of the speed of light c, i is the angle between the line of sight and the orbital angular momentum, and M is the total mass of the system. This quantity and the individual NS masses, M_p and M_c, are here expressed in solar masses.

The orbital eccentricity of the system ($e = 0.17$) allows a detection of one post-Keplerian (PK) parameter, the rate of advance of periastron ($\dot{\omega}$). If we assume this to be purely relativistic, then it depends only on the total mass of the system M and Keplerian orbital parameters, which are already known precisely (Robertson, 1938; Taylor & Weisberg, 1982):

$$M = \frac{1}{T_\odot}\left[\frac{\dot{\omega}}{3}(1-e^2)\right]^{\frac{3}{2}}\left(\frac{P_\mathrm{b}}{2\pi}\right)^{\frac{5}{2}}. \tag{4.2}$$

Our measurement of $\dot{\omega}$ yields $M = 2.538 \pm 0.022\,M_\odot$. This could be the lightest DNS known, but this is not clear yet: the previous lightest DNS, PSR J1756−2251, has a total mass of $2.56999(6)\,M_\odot$ (Ferdman et al., 2014), the difference in mass between the two systems, $0.032\,M_\odot$, is only 1.45 times the 1σ uncertainty on the mass of the PSR J1411+2551 system.

From the total mass and the Keplerian mass function, we can obtain a lower limit for M_c (assuming $i = 90°$):

$$M_c > \sqrt[3]{M^2 f(M_p, M_c)} \approx 0.92 M_\odot. \tag{4.3}$$

Given the value of M, this implies $M_p < 1.62\,M_\odot$. The remaining PK parameters are, for the time being, not measurable in this system.

We have searched for radio pulsations from the companion in observations which were taken in coherently dedispersed search mode. These observations were first dedispersed at the nominal DM of PSR J1411+2551. After that, we removed the orbital modulation due to the putative companion orbit with a code already used in Martinez et al. (2015), making the companion appear as if it were isolated, and thus maximizing our search sensitivity. This technique, however, requires the knowledge of the system mass ratio, $q = M_\mathrm{p}/M_\mathrm{c}$, which is unknown. Nevertheless, assuming a conservative minimum mass for a NS of $0.8\ M_\odot$, and using the total system mass and the limits on M_p and M_c reported above, we find that the value of q must be between $\sim (0.46 - 1.76)$. Hence, we treated q as a free parameter and let it vary within this range, with a sensible choice of the step size. Each de-modulated time series produced was then searched with the `PRESTO` pulsar search code[3]. No pulsations coming from the companion NS were found.

4.3.1 Formation of the PSR J1411+2551

Following the reasoning presented in the introduction, the recycled nature of PSR J1411+2551 and its eccentric orbit, indicate it is a member of a DNS system. If the companion had slowly evolved into a massive white dwarf (WD) no supernova event (with associated kick and mass loss) would occur, and the orbit would still be (nearly) circular. The measured basic properties of the system ($P = 62$ ms, $P_b = 2.62$ days and $e = 0.17$) match very well that of other DNS systems. For example, the spin period of 62 ms fits nicely with the observed (P_b, P) relation for recycled pulsars in similar systems (Tauris et al., 2017):

$$P \approx 44 \text{ ms } (P_b/\text{days})^{0.26}. \tag{4.4}$$

[3] http://www.cv.nrao.edu/~sransom/presto/

Table 4.1. PSR J1411+2551: Timing Solution

PSR	J1411+2551
Fitting program	TEMPO
Time Units	TDB
Solar system ephemeris	DE421
Reference Epoch (MJD)	57617
Span of Timing Data (MJD)	57049-57915
Number of TOAs	660
RMS Residual (μs)	32.77
Solar n_0 (cm^{-3})	10.0
Right Ascension, α (J2000)	14:11:18.866(3)
Declination, δ (J2000)	+25:51:08.39(7)
Proper motion in α, μ_α (mas yr^{-1})	$-3(12)$
Proper motion in δ, μ_δ (mas yr^{-1})	$-4(9)$
Pulsar Period, P (s)	0.062452895517590(2)
Period Derivative, $\dot{P}$ (10^{-20} ss^{-1})	9.56(51)
Dispersion Measure, DM (pc cm^{-3})	12.3737(3)
Rotation Measure, (rad m^{-2})	7.6(7)
Binary Parameters	
Orbital model	DD
Orbital Period, P_b (days)	2.61585677939(8)
Projected Semi-major Axis, x (lt-s)	9.205135(2)
Epoch of Periastron, T_0 (MJD)	57617.04513(1)
Orbital Eccentricity, e	0.1699308(4)
Longitude of Periastron, ω ($^\circ$)	81.5413(2)
Rate of advance of Periastron, $\dot{\omega}$ ($^\circ$yr^{-1}) ..	0.0768(4)
Derived parameters	
Mass function, f ($M_\odot$)	0.1223898(9)
Total Mass, M ($M_\odot$)	2.538(22)
Pulsar Mass, M_p ($M_\odot$)	< 1.62
Companion Mass, M_c ($M_\odot$)	> 0.92
Galactic Longitude, l	33.3789
Galactic Latitude, b	72.1009
DM Derived Distance, d (kpc)	0.977
Galactic height, z (kpc)	0.93
Surface Magnetic Field Strength, B_0 (10^9 G)	$\sim$ 1.8 - 2.6
Characteristic Age, τ_c (Gyr)	9.1 - $\sim$20

Notes. The distance is derived from the DM using the Cordes & Lazio (2002) model of the Galactic electron density with a $\sim$25% uncertainty.

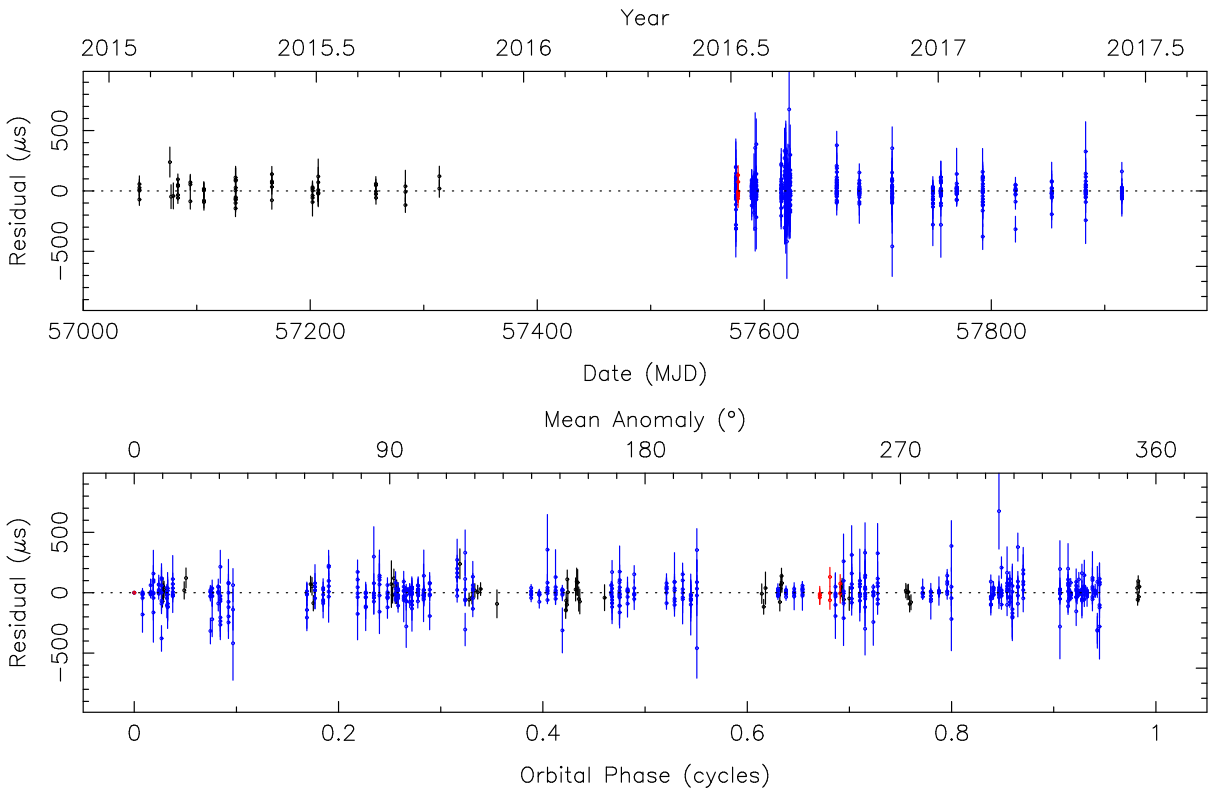

Figure 4.2. Post-fit residuals (time of arrival − best-fit model) for the TOAs and timing solution of PSR J1411+2551. *Top*: Residuals displayed versus epoch. *Bottom*: Residuals versus orbital phase. The black residuals correspond to the incoherent search mode data at 327 MHz, the blue ones to the coherently dedispersed data at 327 MHz and the red to the coherently dedispersed data at L-band. All data were taken with PUPPI. No significant trends are detectable in the residuals, showing that the ephemeris in Table 4.1 provides a good description of the data.

This is seen in Figure 4.3. Also the relatively small measured eccentricity of PSR J1411+2551 is a typical value of the subgroup of DNS systems that are thought to have undergone an ultra-stripped SN with small ejecta mass and often small kicks (Tauris et al., 2013, 2015, 2017).

We have simulated the kinematic effects of 200 million SN explosions in order to reproduce the measured orbital parameters of the PSR J1411+2551 system, following the method applied in Tauris et al. (2017). As in that paper, in our Monte Carlo simulations, we assume that M_c falls within the range of masses measured for young NS in other DNS systems ($1.17 - 1.39$ M$_\odot$) with a flat probability distribution. M_p is then obtained from $M - M_c$.

The simulated solutions for the pre-SN binary show an enhanced probability for a small mass of the exploding star (i.e. < 2.5 M$_\odot$) and a small associated kick of < 100 km s^{-1}, as expected for ultra-stripped star progenitors (the kick value distribution peaks near 50 km s^{-1}, although solutions are found up to almost 200 km s^{-1}). The pre-SN orbital period was somewhere in the interval $1.4 - 3.3$ days.

Finally, we notice that the merger time of PSR J1411+2551 is ~ 460 Gyr, given its relatively wide orbit. Therefore, despite its potentially large true age inferred from a small value of $\dot{P}$, there have been no changes in its orbital parameters at any significant level since its formation.

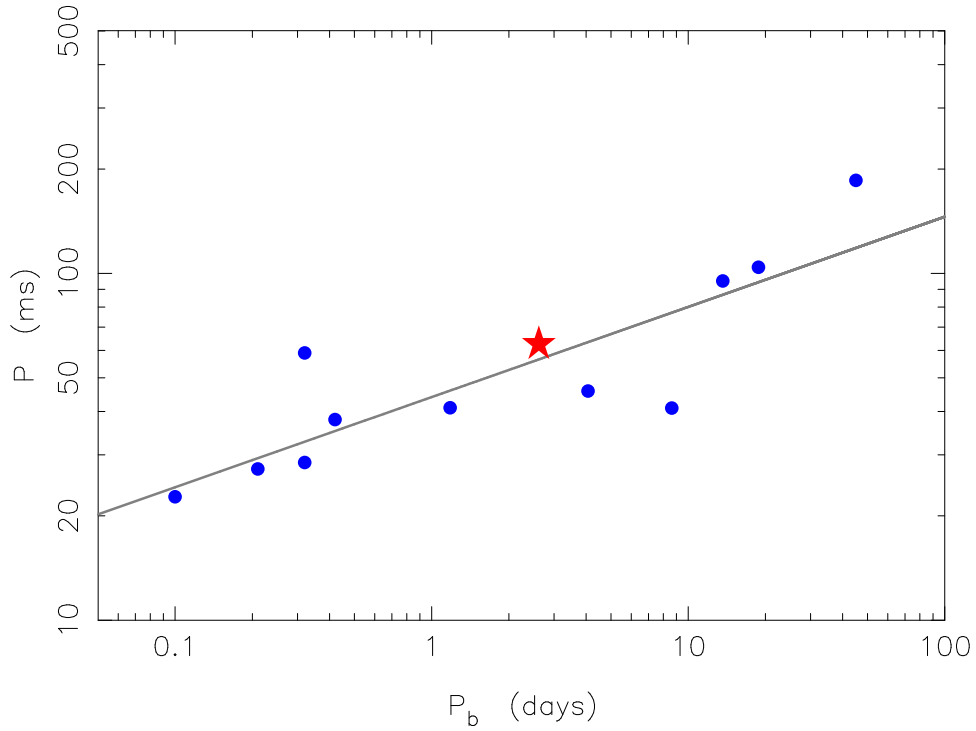

Figure 4.3. The blue points represent the spin period of the recycled pulsars in DNS sytems as a function of their orbital period. PSR J1411+2551 is represented by the red star. The grey line represents Eq. 4.4. For a detailed discussion, see Tauris et al. (2017).

4.4 Discussions and Conclusions

We have presented the discovery and timing solution of PSR J1411+2551, a 62.4-ms pulsar in an eccentric binary orbit with a NS found in the Arecibo 327 MHz Drift Pulsar Survey. We searched for the companion NS as a radio pulsar, but the search did not result in a detection. The 2.5 years of timing observations provided the detection of the rate of advance of periastron for the orbit. Assuming GR, it resulted in the measurement of a total mass for the system of M $= 2.538 \pm 0.022$ $M_\odot$, making it the lightest total mass measurement for a known DNS system, to date.

Because of PSR J1411+2551 long orbital period, it is unlikely that we will be able to measure other PK parameters. As in the case of J0453+1559 (Martinez et al., 2015), the Einstein delay (γ) will be strongly correlated with the kinematic $\dot{x}$ induced by the proper motion (Arzoumanian et al. 1996 and Kopeikin 1996). The variation of the orbital period caused by the emission of gravitational waves ($\dot{P}_{\rm b,predicted} \simeq -6.24 \times 10^{-15}\,{\rm s\,s^{-1}}$ for nearly equal NS masses) will likely be undetectable given the likely much larger kinematic contributions: $\dot{P}_{\rm b,k} = -4.70 \times 10^{-14}\,{\rm s\,s^{-1}}$ from the Galactic acceleration (McMillan, 2017) and $\dot{P}_{\rm b,k} = 2.14 \times 10^{-13}\,{\rm s\,s^{-1}}$ for proper motions of up to $\sim 20\,{\rm mas\,yr^{-1}}$ (Shklovskii, 1970). The Shapiro delay was not detectable for this system; this implies that it does not have a high orbital inclination. Without any other PK parameters we cannot measure the individual masses of the two NSs in the system.

For investigating the destiny of merging DNS systems, it is of utmost importance to probe the possible final masses of the DNS merger products. If the merger product is less massive than some critical value then, rather than forming a black hole directly, it may provide a long-lived

central engine in terms of a proto-magnetar (i.e., a fast rotating object emitting strong magneto-dipole radiation) that powers the extended X-ray emission observed in a large fraction of short gamma-ray bursts (e.g., Zhang & Mészáros, 2001; Metzger et al., 2011; Rowlinson et al., 2013; Rezzolla & Kumar, 2015, and references therein). However, the existence of such meta-stable NSs depends on both the NS equation-of-state (EoS) and the possible masses of the DNS merger products.

The DNS system J1411+2551 provides the smallest total mass (2.54 $M_\odot$) of any DNS system found so far, including the total mass estimated for the DNS merger event GW170817 detected recently by LIGO-Virgo collaboration (Abbott et al., 2017). In Figure 4.4, we demonstrate that the resulting remnant mass of a DNS merger from an equivalent system would yield a total gravitational mass of about 2.30 $M_\odot$ using some of the EoS from Lattimer & Prakash (2001). This is even a conservative upper limit since an outflow of baryonic matter from the collision will remove up to $\sim$ 0.05 $M_\odot$ as inferred from GW170817 (Drout et al., 2017). Thus, the final compact object left behind is only some 0.25 $M_\odot$ heavier than the current record holder for a massive NS, PSR J0348+0432, which has a mass of 2.01 ± 0.04 $M_\odot$ (Antoniadis et al., 2013). Note that, among the different EoS models we used, AP3, MPA1 and PAL1 are able to leave behind a stable NS in this case. This result would be interesting to compare with the constraints of EoS coming from NICER (Neutron star Interior Composition Explorer) and further LIGO-Virgo detections in the near future.

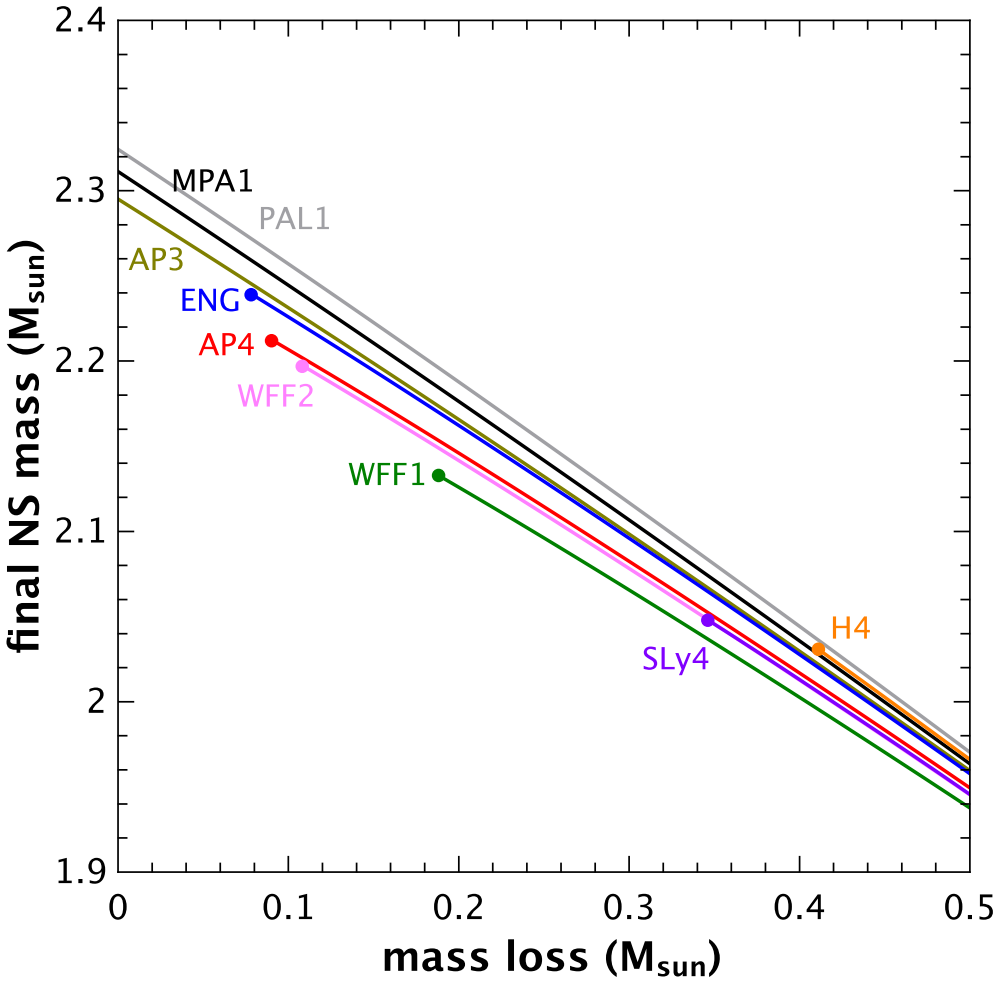

Figure 4.4. Final NS mass for various EoS as a function of baryonic mass loss in a DNS merger event for a system similar to PSR J1411+2551. Only the AP3, MPA1 and PAL1 EoS models are able to leave behind a stable (slowly rotating) NS if the baryonic mass loss is less than about 0.05 $M_{\odot}$. For the different EoS see Lattimer & Prakash (2001). Note, the EoS models H4 and PAL1 correspond to rather large neutron stars (typical radii ∼14 km) and are therefore disfavored by the GW170817 merger event (Abbott et al., 2017).

Chapter 5

Discovery of Six Recycled Pulsars from the Arecibo 327-MHz Drift-Scan Pulsar Survey

This chapter is based on an article submitted to the Astrophysical Journal (Martinez et al., 2019, submitted March 6, 2019).

I am the lead author of the article. My main contributions include the follow-up of the six recycled pulsars presented in this chapter. I performed some of the observations, processed the data, and performed the timing analysis. The text, figures, and tables have only been modified to match the style and format of this thesis.

The full list of authors is:
J.G. Martinez, P. Gentile, P.C.C. Freire, K. Stovall, J.S. Deneva, G. Desvignes, F.A. Jenet, M.A. McLaughlin, M.Bagchi, T. Devine

Abstract

Recycled pulsars are old ($\gtrsim 10^8$ yr) neutron stars that are descendants from close, interacting stellar systems. In order to understand their evolution and population, we must find and study the largest number possible of recycled pulsars in a way that is as unbiased as possible. In this work, we present the discovery and timing solutions of five recycled pulsars in binary systems (PSRs J0509+0856, J0709+0458, J0732+2314, J0824+0028, J2204+2700) and one isolated millisecond pulsar (PSR J0154+1833). These were found in data from the Arecibo 327-MHz Drift-Scan Pulsar Survey (AO327). All these pulsars have a low dispersion measure (DM) ($\lesssim 45\,\mathrm{pc\,cm^{-3}}$), and have a DM-determined distance of $\lesssim 3$ kpc. Their timing solutions, which have data spans ranging from 1 to ~ 7 years, include precise estimates of their spin and astrometric parameters, and for the binaries, precise estimates of their Keplerian binary parameters. Their orbital periods range from about 4 to 815 days and the minimum companion masses (assuming a pulsar mass of 1.4 $M_\odot$) range from ~ 0.06–1.11 $M_\odot$. For two of the binaries we detect post-Keplerian parameters; in the case of PSR J0709+0458 we measure the component masses but with a low precision, in the not too distant future the measurement of the rate of advance of periastron and the Shapiro delay will allow very precise mass measurements for this system. Like several other systems found in the AO327 data, PSRs J0509+0854, J0709+0458 and J0732+2314 are now part of the NANOGrav timing array for gravitational wave detection.

5.1 Introduction

5.1.1 Recycled Pulsars

Pulsars that have undergone a binary interaction history are known as "recycled pulsars". They are the first formed compact object in the current observed binary system. They have been spun to high spin frequencies via accretion of mass and angular momentum from the secondary star (Alpar et al., 1982); during this phase these systems are observable as X-ray binaries (Tauris & van den Heuvel, 2006).

Recycling seems to decrease the surface dipolar magnetic fields of these neutron stars to relatively low values ($B \sim 10^8 - 10^{10}$ G). These low values of B result in very small spin-down rates and, consequently, large ($\gtrsim 10^8$ yr) characteristic ages.

Recycled pulsars can be further divided into two subclasses, millisecond pulsars (MSPs), which we define here as having spin periods smaller than that of the fastest-spinning pulsar in a double neutron star system, 16.7 ms (Stovall et al., 2018), and mildly recycled pulsars (MRPs), which have larger spin periods. The reason for the slower spin periods of MRPs is that (generally) the progenitors of their companions were massive stars with faster evolution; for such systems the recycling phase is short-lived (Tauris et al., 2015); these systems have smaller decreases in B.

In contrast, the companions to MSPs had lower mass progenitors, which evolve much more slowly. In such cases, the recycling process is longer, which allows for greater amounts of mass and angular momentum to be accreted onto the NS (Tauris et al., 2011, 2012) and a more extensive reduction of the magnetic field. All recycled pulsars are relics of the evolution of close, interacting binary systems, and their observed properties are ancient records of their evolutionary history.

5.1.2 Applications

Recycled pulsars are stable rotators and can be timed very precisely. This property allows many applications: using them as key probes of stellar astrophysics (Bhattacharya & van den Heuvel, 1991; Tauris et al., 2011, 2012), tests of General Relativity (GR) using double neutron star (DNS) systems, such as PSR J0737−3039 (Kramer et al., 2006), PSR B1913+16 (Weisberg & Huang, 2016), PSR J1946+2052 (Stovall et al., 2018) and PSR J1757−1854 (Cameron et al., 2018); tests of alternate theories of gravity using the orbital decay of MSP-white dwarf systems such as PSRs J1738+0333 and J0348+0432 (Freire et al., 2012; Antoniadis et al., 2013) and the universality of free fall in the triple system PSR J0337+1715 (Ransom et al., 2014; Archibald et al., 2018). They have set strong constrains on the equation of state of dense matter by extending the known mass limits of a neutron star from systems like PSR J0348+0432 (Antoniadis et al., 2013). Last but foremost, recycled pulsars, more specifically MSPs, have helped set limits on the low-frequency gravitational wave background in the Universe by using pulsar timing arrays (PTAs)(Arzoumanian et al., 2018; Shannon et al., 2015; Lentati et al., 2015), with sensitivities expected to grow in time.

5.1.3 The Arecibo 327-MHz Drift-Scan Pulsar Survey

Given this vast range of applications, many ongoing large scale pulsar surveys are currently being undertaken with the objective of finding new millisecond pulsars. The Arecibo 327-MHz Drift-Scan Pulsar Survey (AO327) is searching the entire Arecibo sky (declination range from

$-1°$ to $38°$) (Deneva et al., 2013) in drift-scan mode at a center frequency of 327-MHz. The survey began in 2010 and since then it has a running total of 85 discoveries, including 16 new recycled pulsars, 10 of which are MSPs, and 16 rotating radio transients (RRATs). This includes some noteworthy discoveries of two DNS systems: PSR J0453+1559, is the first asymmetric DNS with the smallest precisely measured mass of any neutron star (Martinez et al., 2015) and PSR J1411+2551, one of the lowest total mass DNSs known (Martinez et al., 2017). This survey also discovered PSR J2234+0611, a millisecond pulsar (MSP) with an eccentric orbit with high timing precision and optical spectroscopic measurements of the He white dwarf (WD) companion, which make this binary system a great laboratory for studying stellar evolution (Deneva et al., 2013; Antoniadis et al., 2016; Stovall et al., 2019).

5.1.4 Motivation and Structure of the Paper

In this letter, we present the discovery and follow-up timing of six recycled pulsars found in AO327 data: four MSPs (PSRs J0154+1833, J0509+0856, J0732+2314, and J0824+0028) and two MRPs (PSRs J0709+0458 and J2204+2700). In Section 5.2, we describe the observations used to discover and time these systems. In Section 5.3, we describe the details of each pulsar and the nature of binary companions. In Section 5.4, we describe the measurements of Post-Keplerian parameters and their implications. We summarize our findings in Section 5.5.

5.2 Timing Observations

The observations and the initial follow up of each pulsar were made with the Arecibo 305-m radio telescope and the 327-MHz receiver, with the Puerto Rico Ultimate Pulsar Processing Instrument (PUPPI) as a back-end. After the discovery of each pulsar (which is listed almost immediately on the AO327 website[1]) we begin regular timing observations. For the initial timing, PUPPI is used in incoherent search mode with a bandwidth of 68.7 MHz that is split in 2816 channels with a sample time of 82 μs. These are processed with the `PRESTO`[2] pulsar software, first to remove radio frequency interference in the data, and then to dedisperse and fold the data at optimal spin periods and DMs.

When a pulsar is in a binary system, there is a Doppler modulation of the observed spin period that is sinusoidal in the case for almost circular orbits. Once having fitted a sinusoidal curve to the spin period modulations over time with sufficient data with available public software `FITORBIT` [3]. We determined the binary parameters and incorporate them in our initial timing model.

We then determine the phase coherent timing solutions for the pulsars. With these solutions, we can account for every single rotation of the pulsar for the whole observational data span. In the case of PSR J0732+2314, we had to use the algorithm described by Freire & Ridolfi (2018) to obtain phase connection. After obtaining these solutions we can use PUPPI in coherent folding mode, this mode coherently dedisperses and folds the data online, which removes dispersive effects of the interstellar medium. The observations in this mode results in much higher time resolution and lower data rates. The precise position contained in the timing solution also means that we can use receivers other than the 327-MHz that have smaller beams, in particular the 430-MHz, L-wide and S-low. The 327-MHz and 430-MHz receivers have a total bandwidth of

[1] http://naic.edu/ deneva/drift-search/
[2] https://www.cv.nrao.edu/ sransom/presto/
[3] http://www.jb.man.ac.uk/pulsar/Resources/tools.html

87.5 MHz (each have a visible bandwidth of 50 MHz and 25 MHz respectively) that is split in 56 channels. The L-wide and S-low receivers both have a bandwidth of 800 MHz that is split in 512 channels.

Most of the pulsars were observed at these 4 frequencies to determine an optimal timing frequency where they have the highest signal-to-noise in an observing time of 10 min and sharp profile features. The frequency where each pulsar has the most optimal timing then becomes the main frequency for observations of that pulsar. These multi-frequency observations were also made in order to measure the polarimetric properties of the emission of these pulsars at a range of frequencies; these are shown in Figures 5.1 to 5.3. Figure 5.1, additionally contains the total intensity, single frequency profile of PSR J2204+2700. Three of the pulsars presented in this work have broad, complex profiles with many different components and emission from most of the spin cycle; the components have vary in shapes and intensities at different frequencies, particularly for PSRs J0509+0856 (Figure 5.1), J0732+2314 (Figure 5.2) and J0824+0028 (Figure 5.3). All of the coherent folding mode observations made it possible to determine at a high precision each pulsar's rotational, astrometric, and if in a binary, orbital parameters.

We calculated the pulsar's pulse times of arrival (TOAs) via Fourier-domain cross-correlation of a noise-free template and the observed pulse profile (Taylor, 1992), after the data has been calibrated. The data was calibrated using the noise diode observations taken before each observation. Each observation is then corrected for the Faraday effect, which requires the measurement of the rotation measure (RM) by using `rmfit` from `PSRCHIVE` software (Hotan et al., 2004; van Straten et al., 2012). The templates were created by fitting one or more Gaussians to the pulse profiles. At each epoch we generally split the data into four sub-integrations and eight frequency sub-bands, sometimes less due to short observations. Then we averaged the data in time and frequency, calculating an average of TOAs per epoch.

We then used the `TEMPO`[4], a pulsar timing program, to fit a timing model to the observed TOAs. The initial model consists of spin frequency and its derivative, position, and dispersion measure (DM). In binary systems, we also fit for Keplerian and post-Keplerian orbital parameters using timing models based on the Damour & Deruelle (1986) model (DD): these are the DDGR model, which assumes the validity of GR to fit for the masses directly, the DDH model, which is a theory-independent model that uses a new parameterization of the Shapiro delay (Freire & Wex, 2010) and ELL1 model, another theory-independent model developed specifically for low-eccentricity binaries (Lange et al., 2001). We used the DE421 solar system ephemeris in all of the pulsar's timing models. There are newer solar system ephemerides, however, detailed analyses by the NANOGrav consortium reveal that no Solar System ephemeris is completely satisfactory(Arzoumanian et al., 2018). However, the differences between the Solar System ephemerides are very small, resulting in differences in the timing parameters of the pulsars that are much smaller than their estimated uncertainties.

Several of the systems presented here were timed by the NANOGrav, with the idea of verifying their timing stability and suitability for pulsar timing arrays. For this reason, a significant amount of the timing data presented here was taken by the NANOGrav collaboration, who share such data with the discoverers.

All the final measured parameters of the pulsar's spin frequency and its derivative, position, DM and, when appropriate, binary parameters are presented in Table 5.1. We also present in this table some derived quantities. First, we derived the Galactic coordinates (l and b); then from these and the DMs we estimate the distances (d) using NE2001 (Cordes & Lazio, 2002)

[4] `http://tempo.sourceforge.net`

and YMW (Yao et al., 2016) models for the Galactic distribution of free electrons. We also fit for the total proper motion, μ. Then, using the NE2001 distances we estimate the value of the intrinsic spin period derivative ($\dot{P}_{\rm int}$) using

$$\dot{P}_{\rm int} = \dot{P} - \frac{P}{c}\left(\mu^2 d + a_l\right), \tag{5.1}$$

where the first term in parentheses consist of the Shklovskii effect (Shklovskii, 1970), which is caused by the proper motion, and the second term is the effect of the difference in the Galactic accelerations of the pulsar's system and the Solar System projected along the direction from the pulsar to the Earth (Damour & Taylor, 1991). In order to estimate a_l, we use the expressions presented by Lazaridis et al. (2009), as the equation for the vertical acceleration should be valid to a Galactic height of $\sim \pm 1.5$ kpc, which is certainly the case for all the new systems presented here. Additionally, for the acceleration parallel to the Galactic plane, we use the distance to the center of the Galaxy measured by the GRAVITY experiment (Gravity Collaboration et al., 2018), $r_0 = 8.122(31)$ kpc and a revised value for the rotational velocity of the Galaxy derived using the latter r_0 (McGaugh, 2018), $v_{\rm Gal} = 233.3$ km s^{-1}.

Finally, from $\dot{P}_{\rm int}$ we derive the characteristic ages, τ_c, inferred surface magnetic field strengths, B, and spin-down energy loss rates, $\dot{E}$. All these derived parameters are also presented in Table 5.1.

5.3 Results

5.3.1 PSR J0154+1833

PSR J0154+1833 is isolated and the most rapidly rotating of the six recycled pulsars, with a spin period of 2.36 ms and a DM of 19.79 pc cm^{-3}. Our timing solution has a root mean square (RMS) residual of 1.23 μs and spans about 3 years. This pulsar's optimal timing frequency is at 327-MHz. Since most of the data for this pulsar was taken at 327-MHz, we retained great sensitivity to DM variations. This is important because this pulsar has a low ecliptic latitude, which means that once a year it has a small angular separation with the Sun, and during this time the effects of the solar wind produce important deviations in the TOAs. We do not have enough data to model the effect of the solar wind in detail. A DMX model has been used to fit for these DM variations leaving our timing model with a reduced χ^2 of 1.

5.3.2 PSR J0509+0856

PSR J0509+0856 is an MSP with a spin period of 4.05 ms and a DM of 38.25 pc cm^{-3}. It is in a 4.90 day almost circular ($e = 0.000023$) orbit. The minimum and median mass of the companion can be calculated from the measured mass function for this system. If we assume an orbital inclination of $i = 90°$ and a pulsar mass of $1.4 M_\odot$, we get a minimum companion mass of 0.11 $M_\odot$ and a median companion mass (i.e. $i = 60$) of 0.13 $M_\odot$.

The minimum companion mass is much lower than the prediction of the Tauris & Savonije (1999) and Tauris et al. (2012) models for the mass of a Helium WD companion for the orbital period of this pulsar, which is of the order of 0.22 $M_\odot$. This suggests that, if the companion is a He WD (the spin period of the pulsar and the orbital eccentricity of the system certainly are compatible with those of other MSP - He WD systems with similar orbital periods), then either the system has a low orbital inclination (the inclination will be even lower if the companion is a

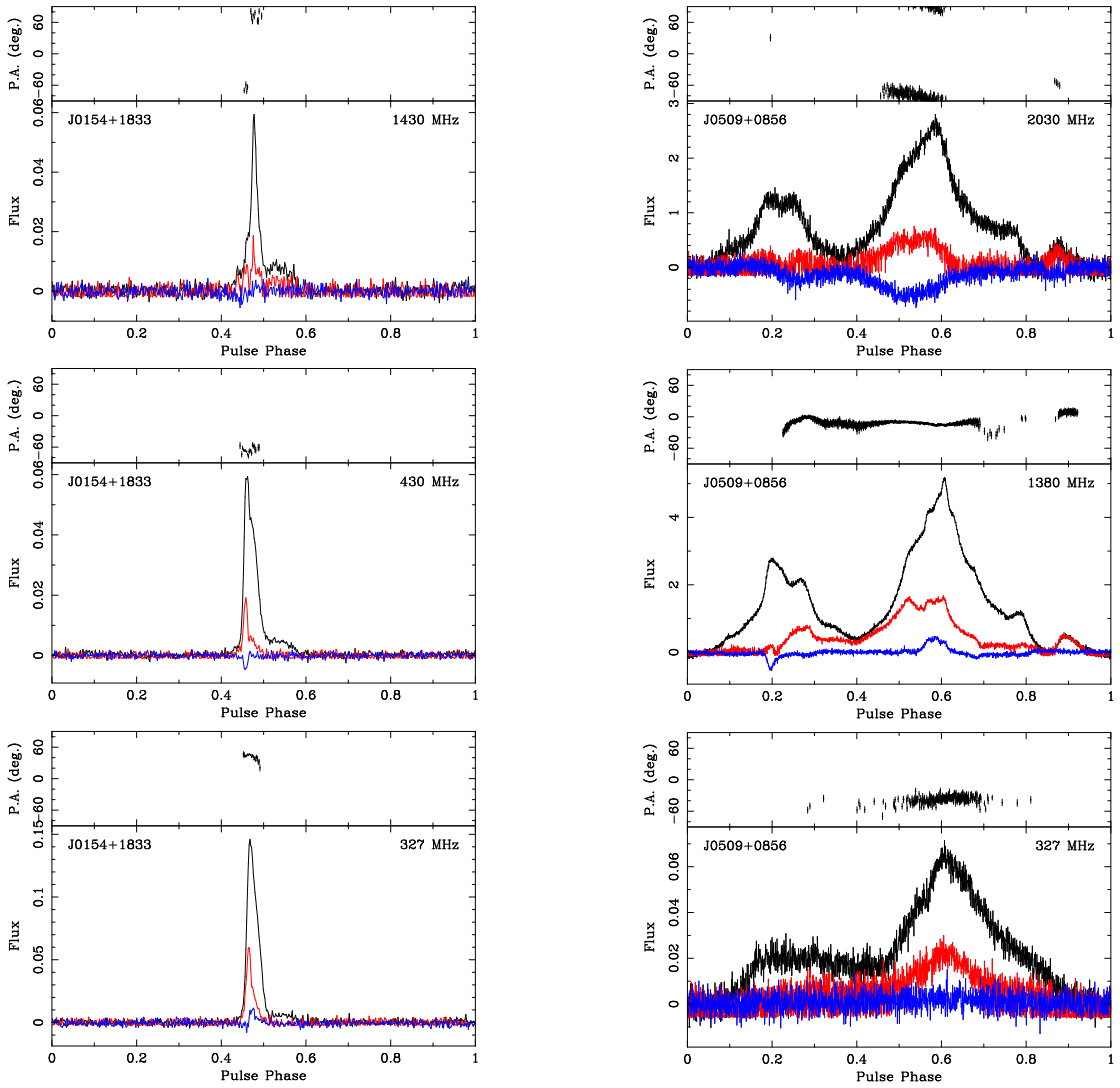

a) J0154+1833

b) J0509+0856

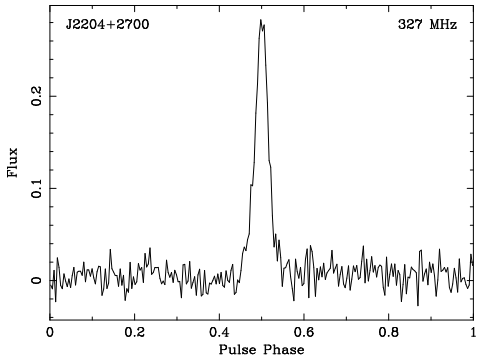

c) J2204+2700

Figure 5.1. Polarization calibrated pulse profiles for PSRs J0154+1833 and J0509+0856, based on full Stokes data taken at the radio frequencies shown on the right of each profile. They are obtained by averaging the best detections; the black line indicates the total intensity, the red line is the amplitude of linear polarization, and the blue line is the amplitude of the circular polarization. At the top of each polarization calibrated pulse profile, we show the position angle of the linear polarization. At the bottom of this figure we show a pulse profile of PSR J2204+2700 showing only the total intensity in black. This pulsar is only strongly detected at 327-MHz but was observed for short observations due to its low timing precision, therefore we did not have enough signal to noise for polarization calibration. The pulse profile flux is in arbitrary units.

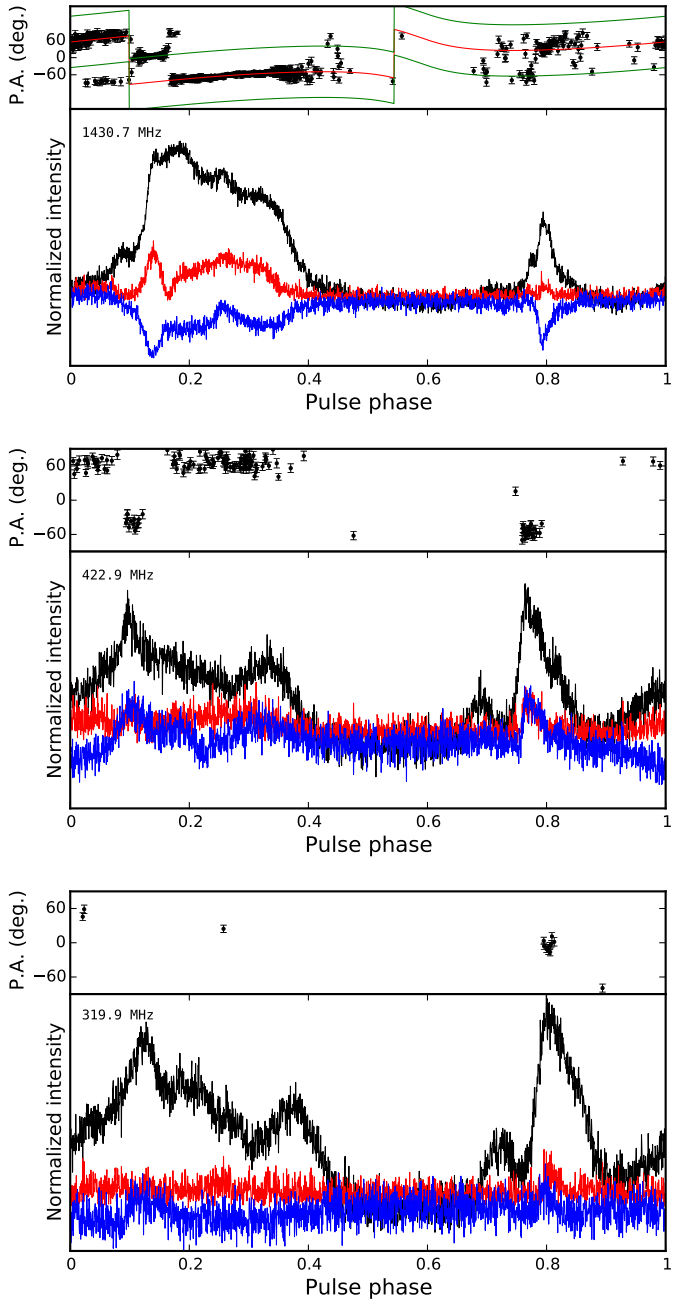

Figure 5.2. Same as Figure 5.1, this time for PSR J0732+2314. For this pulsar, we also display a rotating vector model at the top panel, which is based on the L-band data (more details are in Section **??**). The red line is the rotating vector model fit to the position angle measurements of this pulsar, while the green lines are a 90° orthogonal mode transitions.

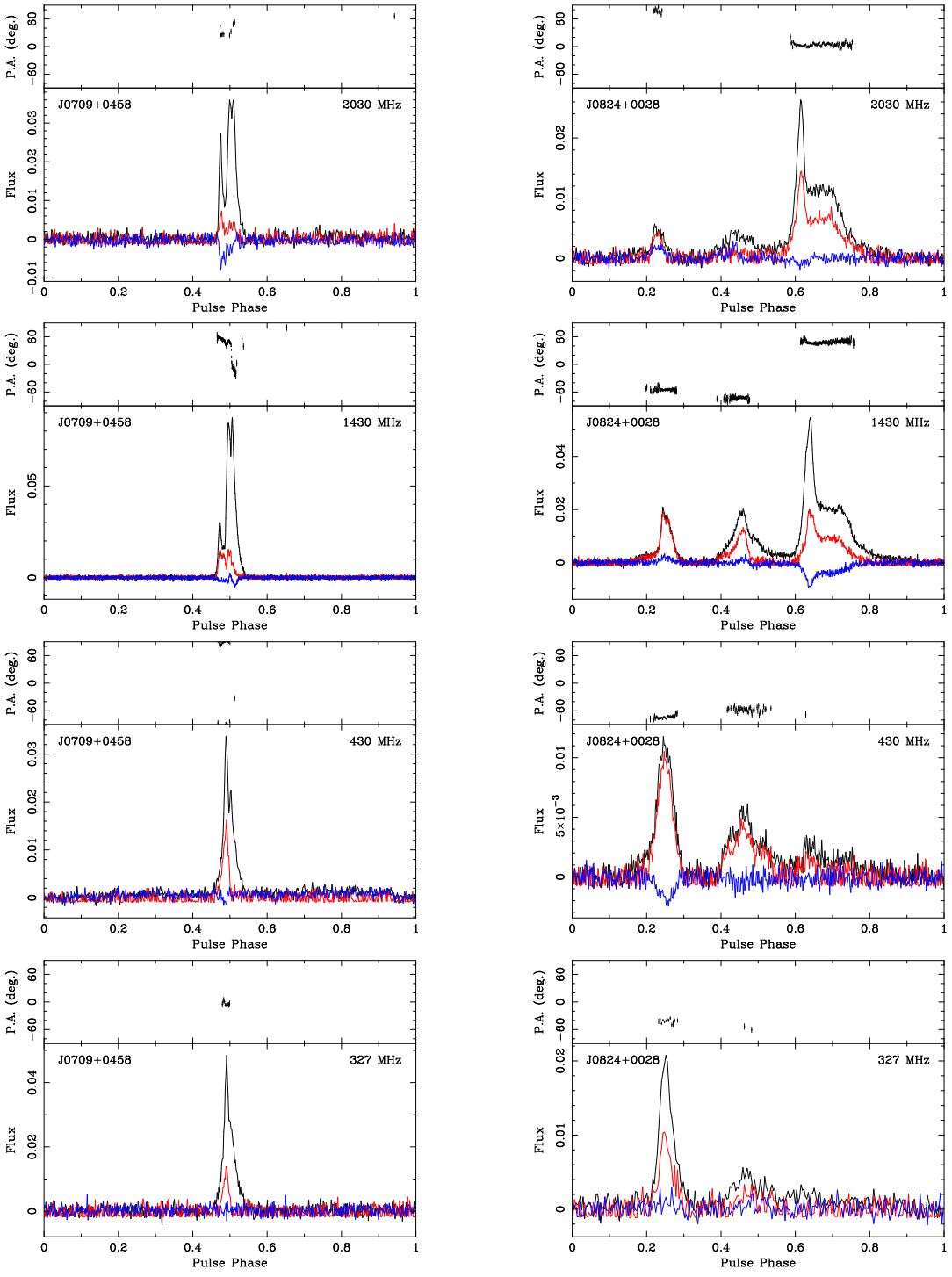

a) J0709+0458 b) J0824+0028

Figure 5.3. Polarization calibrated pulse profiles for PSRs J0709+0458 and J0824+0028, based on full Stokes data taken at frequencies shown on the right of each profile. They are obtain by averaging the best detections; the black line indicates the total intensity, the red line is the amplitude of linear polarization, and the blue line is the amplitude of the circular polarization. In the top of each polarization calibrated pulse profile, we show the position angle of the linear polarization. The pulse profile flux is in arbitrary units.

CO WD), or, if orbital inclination is high, then the pulsar mass is also high. The non-detection of the Shapiro delay in this system suggests the first possibility. The polarimetric properties seem to confirm this: since the spin axis of the pulsar is nearly aligned with the orbital plane, a face-on configuration should be one where the spin axis of the pulsar is nearly aligned with the Earth. In such a case, we should see a very broad profile, which we do observe in this system; indeed we observe radio emission throughout nearly the full spin cycle. Also, the position angle of the linear polarization of the system should vary slowly with spin phase, which is also observed in this system at the three radio frequencies where we have measurements (Figure 5.1).

Our timing solution has an RMS residual of 3.64 μs and spans 4.8 years. This pulsar has very good timing precision and has been regularly observed to determine its suitability for inclusion in the timing campaign being carried out by NANOGrav, which took most of the data used in this work for this pulsar.

5.3.3 PSR J0709+0458

PSR J0709+0458 is a MRP that has a spin period of 34.42 ms and a DM of 44.26 $\mathrm{pc\,cm^{-3}}$. It is in a 4.36-day binary orbit with an eccentricity of 0.000225. This system has a measurement, of the rate of advance of periastron, $\dot{\omega} = 0.032 \pm 0.012^\circ\ \mathrm{yr}^{-1}$, and the orthometric Shapiro delay parameters $h_3 = 2.06(0.27)$ and $\varsigma = 0.64(0.13)$; the consequences of these measurements are discussed in detail in Section **??**; clearly the companion is a massive WD, likely a ONeMg WD.

The relatively high orbital inclination determined in section 5.4, $i \sim 73.3^\circ$, implies that the pulse profile should be relatively narrow. This is indeed observed (Figure 5.3). This narrow profile yields precise timing. We measure a RMS residual of 5.18 μs; for this reason the pulsar has been added to the NANOGrav PTA, which took a significant part of the data used in this work.

5.3.4 PSR J0732+2314

PSR J0732+2314 is an MSP with a spin period of 4.09 ms and a DM of 44.67 $\mathrm{pc\,cm^{-3}}$. It is in a 30.23-day ($e = 0.000010$) orbit around a companion with a minimum companion mass of 0.15 $\mathrm{M_\odot}$ and a median companion mass of 0.18 $\mathrm{M_\odot}$. Again, as in the case of PSR J0509+0456, the minimum companion mass is low compared to the Tauris & Savonije (1999) prediction of $\sim 0.3\,\mathrm{M_\odot}$ for the mass of a He WD that one should expect for this orbital period; as for PSR J0509+0456 this suggests that either the system is being observed at a low orbital inclination, or, if it is being observed at a higher orbital inclination, the pulsar mass is large. Similarly to PSR J0509+0856, the lack of a detection of the Shapiro delay and the characteristics of the pulse profile (Figure 5.2), suggest a low inclination angle. A low inclination angle is consistent with our results from Radhakrishnan & Cooke (1969) 'rotating vector model' (RVM) on the L-band data for this pulsar. The RVM fit yields the following parameters, the magnetic inclination angle $\alpha = 36.6^\circ\ ^{+1.1}_{-1.3}$ and the impact angle $\beta = 16.7^\circ\ ^{+2.2}_{-2.3}$. For the angle between the line of sight and the spin axis ($\zeta = \alpha + \beta$) we get $\zeta = 53.3^\circ\ ^{+2.4}_{-2.5}$. Since this is likely aligned with the orbital angular momentum (Manchester et al., 2010), then it indicates $i \sim 53.3^\circ\ ^{+2.4}_{-2.5}$.

Our timing solution has an RMS residual of 4.69 μs and spans about 1.5 years. This pulsar follows the (Phinney, 1992) relationship between eccentricity and orbital period (P_b) evolution, see Figure 5.4. It fills a noticeable gap within the range of $P_b \sim 22-32$ days where the population is dominated by eccentric binaries which have He WD companions (Knispel et al., 2015; Camilo et al., 2015; Barr et al., 2017a; Octau et al., 2018; Stovall et al., 2019). If we assume the same for

PSR J0732+2314, this would mean that not all such systems in this interval of orbital periods become eccentric. This pulsar has also been included in the NANOGrav PTA.

5.3.5 PSR J0824+0028

PSR J0824+0028 is an MSP with a spin period of 9.86 ms and a DM of 34.55 $\mathrm{pc\,cm^{-3}}$. It is in a 23.20-day, ($e = 0.000230$) orbit around a companion with a minimum mass of 0.34 $M_\odot$ and a median mass of 0.41 $M_\odot$. Our timing observations span about 4.5 years and have a RMS residuals of 4.66 μs. A hint of Shapiro delay has been detected, with orthometric parameters $h_3 = 0.50(0.25)$ and $\varsigma = 0.85(0.11)$. There is no detection of the rate of advance of periastron, $\dot{\omega}$. Even though there is no $\dot{\omega}$, more observations at superior conjunction could lead to mass measurements from Shapiro delay alone. The mass of the companion is too large for a He WD; it is therefore more likely a CO WD. The orbital eccentricity of the system and the spin period of the pulsar match well the characteristics of other systems with CO WD companions; these have a wider range of eccentricities (generally they are more eccentric) than predicted by Phinney (1992).

Similar to PSR J0732+2314, its orbital period is also inside the range dominated by the eccentric binaries mentioned above. However the companion for PSR J0824+0028 is not likely a He WD, so it certainly had a different evolution than the eccentric MSPs.

5.3.6 PSR J2204+2700

PSR J2204+2700 was the first binary pulsar found in AO327 data. It is an MRP with a DM of 35.07 $\mathrm{pc\,cm^{-3}}$. It is in a 815.24-day orbit, the seventh largest orbital period of any pulsar binary, and the widest found so far in AO327 data. Using the mass function, we get a minimum companion mass of 0.36 $M_\odot$ and a median mass of 0.43 $M_\odot$. This system is part of a small group of binary pulsars (which includes PSRs J0214+5222, J2016+1948, J0407+1607, J1711−4322 and possibly J1840−0643, see **?**) with orbital periods between 512 and 937 days, spin periods of tens of ms (84.70 ms in this case) and orbital eccentricities of the order of 10^{-3} ($e = 0.00152$ in this cas e), which nevertheless still follow the relation predicted by Phinney (1992). Such systems have been recycled by mass accretion from the companion, but given the large orbital separations, this has happened only during the brief time when the companion was in its giant phase, which explains the mild recycling. This pulsar is a good candidate to Damour-Schäfer test the strong equivalence principle (SEP). The SEP states that all neutral test masses fall with the same acceleration in an external gravitation fields, the gravitational and inertial masses of self-gravitating bodies are identical. To test this theory, binary pulsars with low companions mass, small eccentricity, and long orbital periods are ideal, as demonstrated in (Gonzalez et al., 2011).

5.3.7 Nature of the Binary Companions

None of the five binaries presented here have a detectable optical counterpart for their companions in the online DSS2 optical survey red/blue filters, nor in the 2MASS survey. Also, none of the binaries show any evidence of eclipses in their timing residuals. This suggests that none of the companions is a main sequence (or at least an extended) star, implying by default that the companions are white dwarf stars.

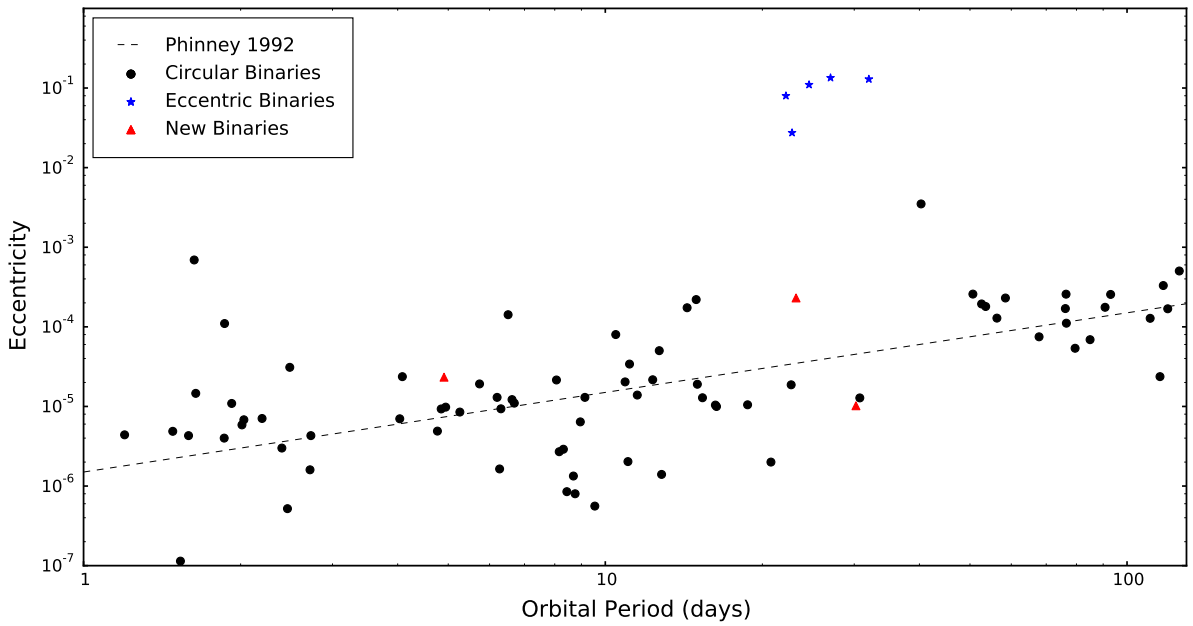

Figure 5.4. Eccentricity (e) as a a function of orbital period (P_b) for recycled pulsars with low-mass companion ($< 0.4 M_\odot$). The dashed line represents the prediction expected from the evolutionary scenario by Phinney (1992). Most recycled pulsars follow this line (shown as solid black circles), although eccentric ($e \sim 0.027 - 0.14$, shown as in blue stars) binaries are found (Knispel et al., 2015; Camilo et al., 2015; Barr et al., 2017a; Octau et al., 2018; Stovall et al., 2019) that likely result from a different evolutionary process (Antoniadis, 2014). For some time, these systems were the only ones found in the $P_b \sim 22 - 32$ days region. The newly discovered PSRs J0732+2314 and J0824+0028 (shown as solid red triangles) are in that P_b region, but are low eccentricity. Also PSR J0509+0856 follows Phinney (1992) evolutionary prediction very well.

5.3.8 Search for pulsars in γ rays

Many MSPs are known to emit detectable γ-ray pulses. This fact motivated us to search for these pulsars in γ rays using the `TEMPO2` *fermi* plugin[5] to fold data from the *Fermi* Large Area Telescope (LAT) (Atwood et al., 2009) at the position of each pulsar. None of the 6 recycled pulsars were detected in γ-rays. The $\dot{E}$ values for four pulsars (J0154+1833, J0509+0856, J0732+2314 and J0824+0028) are above $2 \times 10^{33}\,\mathrm{erg\,s^{-1}}$. Several MSPs have been found with similar values of $\dot{E}$ (Abdo et al., 2009; Ransom et al., 2011).

5.4 Post-Keplerian Parameters

5.4.1 Mass measurement for PSR J0709+0458

For PSR J0709+0458, we have measured three Post-Keplerian (PK) parameters: $\dot{\omega} = 0.026(8)\,^\circ\,\mathrm{yr}^{-1}$ and the Shapiro delay parameters; using the orthometric parameterization (Freire & Wex, 2010) these are $h_3 = 1.86(21)\,\mu\mathrm{s}$ and $\varsigma = 0.75(7)$. These measurements are only possible given the high timing precision of the system and the large companion mass: indeed, an orbital eccentricity of 0.00022 would generally make the measurement of $\dot{\omega}$ impossible.

[5] https://fermi.gsfc.nasa.gov/ssc/data/analysis/user/Fermi_plug_doc.pdf

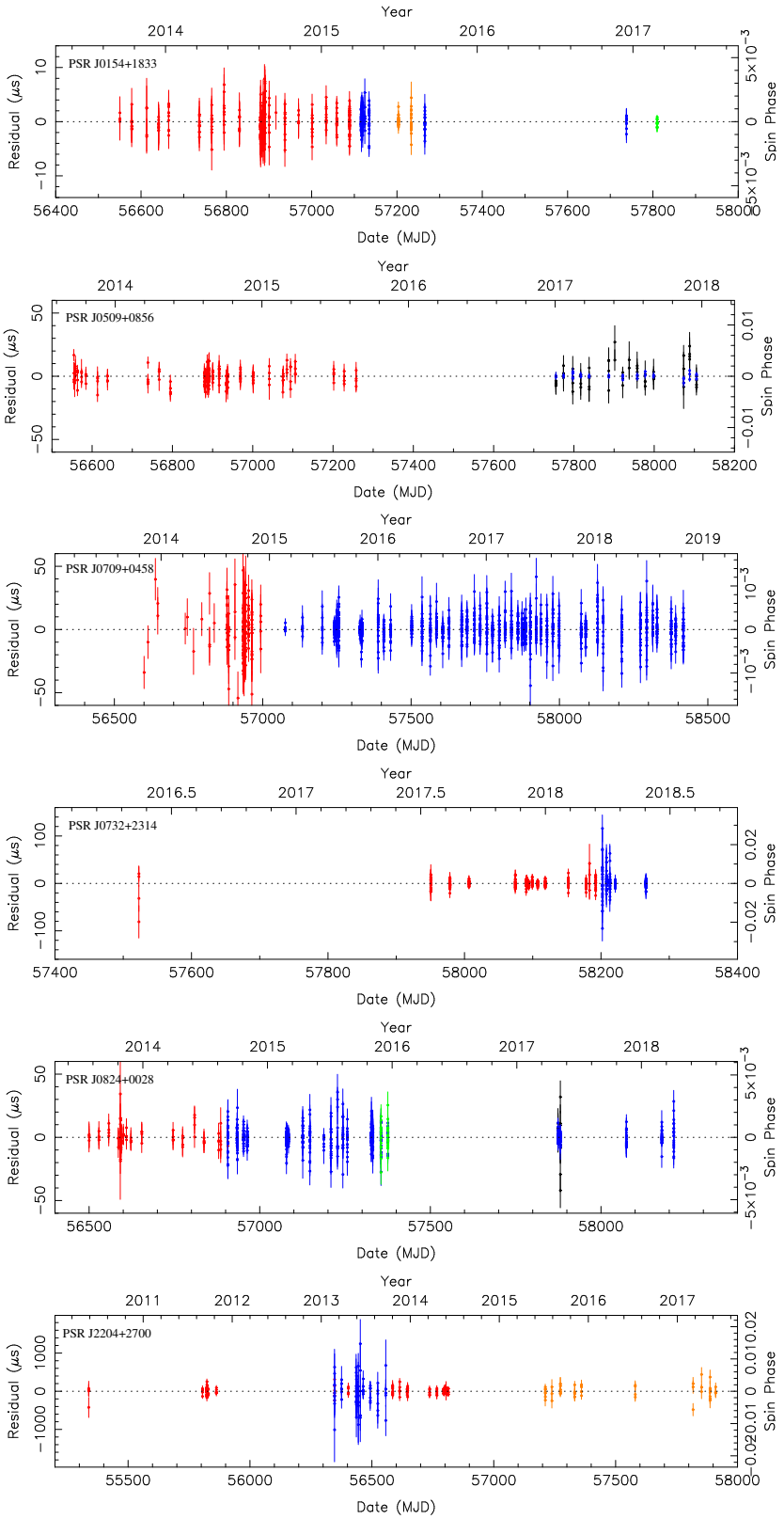

Figure 5.5. TOA residuals as a function of epoch for the six recycled pulsars presented in this paper, with 1-σ error bars. The colors indicate different frequencies and observation modes. *Red:* Incoherent 327-MHz data, *Orange*: coherent 327-MHz data, *Green*: coherent 430-MHz data, *Blue*: coherent L-band (1.15-1.73 GHz) data and *Black*: coherent S-band (1.7-2.2 GHz) data. No unmodeled trends are apparent in this figure and the next, suggesting that the timing solutions in Table 5.1 provide a good description of the TOAs.

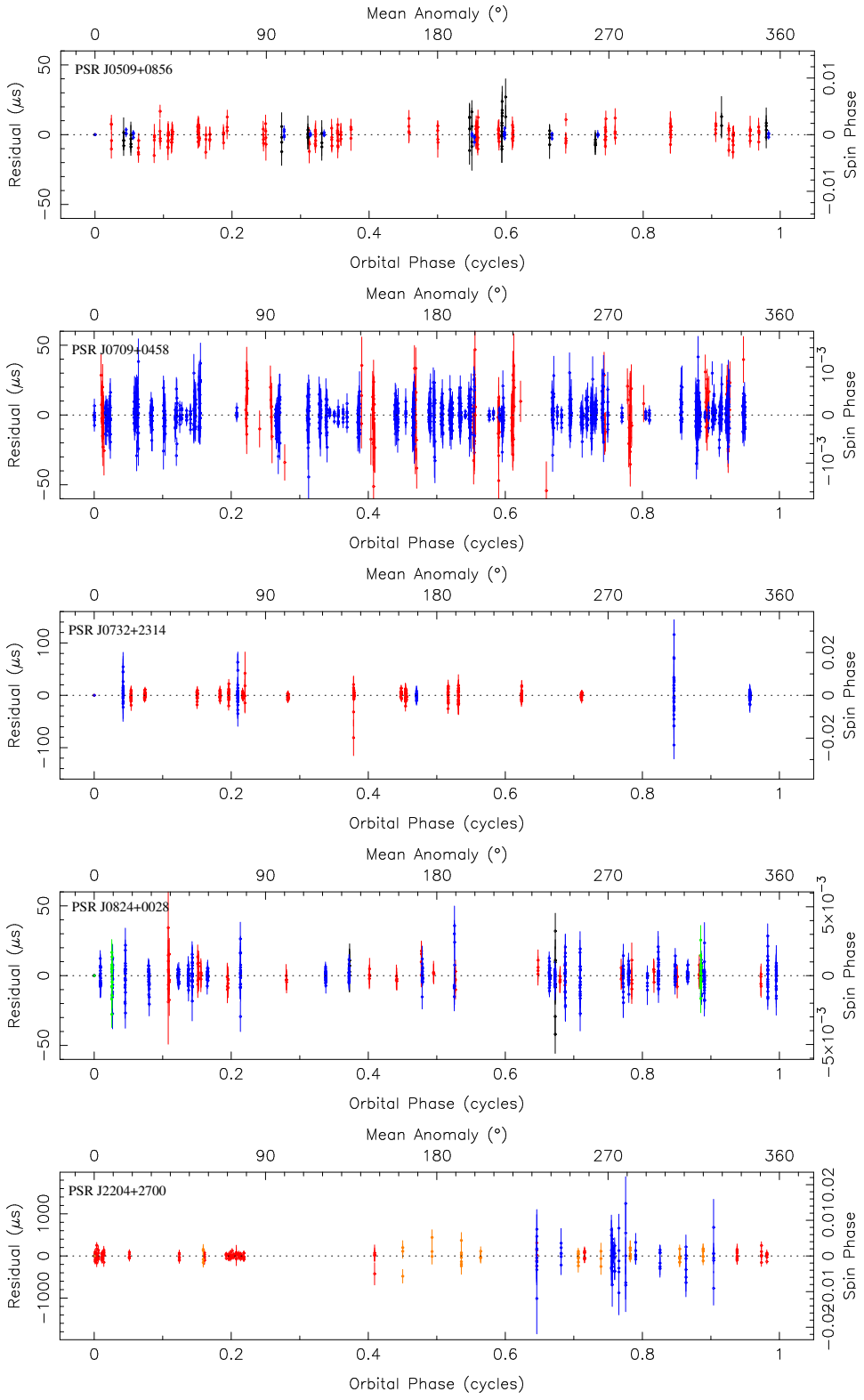

Figure 5.6. Same as in Figure 5.5, but now with the residuals displayed as a function of orbital phase for the five binary pulsars presented in this work. For PSR J0509+0856, where we used the ELL1 model, the mean anomaly is defined relative to the ascending node. For the other pulsars, the mean anomaly is defined relative to periastron.

The mass and inclination constraints introduced by these parameters (assuming GR) are depicted graphically in Figure 5.7. Since we have three PK parameters in this system, this results in a test of that theory. As we can see, all PK parameters agree, so GR passes the test posed by the measurement of these 3 parameters. However, this implies no new constraints on alternative theories of gravity given the limited precision of the PK parameters.

To estimate the mass of the pulsar, the companion and the orbital eccentricity in a self-consistent way (assuming GR), we used the Bayesian method described in detail by Barr et al. (2017b) and references therein. In this method, we make a map of the χ^2 of the residuals (obtained for a DDGR solution for this pulsar) as a function of $\cos i$ (which has a constant probability for randomly oriented orbits) and, unlike in Barr et al. (2017b), h_3[6]. We then transform these χ^2 maps into a 2D probability density function (PDF) in the $\cos i$ - M_c and M_p - M_c planes. The contours holding 68.23% and 95.44% of all probability in these planes are displayed in Figure 5.7. Projecting these 2D PDFs onto the different axes, we obtain the probabilities for the masses and orbital inclination.

The regions of high probability in the main plots are well described by h_3, ς and $\dot{\omega}$ lines and their uncertainties. For the main quantities, the 68.3 % confidence limits are: $M_c = 0.92^{+0.21}_{-0.18}\,M_\odot$, $M_p = 0.86^{+0.38}_{-0.29}\,M_\odot$ and $i = 73.3(3)°$; the 95.4% confidence limits are: $M_c = 0.92^{+0.45}_{-0.34}\,M_\odot$, $M_p = 0.86^{+0.84}_{-0.51}\,M_\odot$ and $i = 73.3(6)°$.

The uncertainties are so large that these values are not yet astrophysically useful (the pulsar mass can be almost anywhere between 0 and 2 $M_\odot$). However, this situation will change with time: The measurement of $\dot{\omega}$ is already constraining the masses significantly; indeed, the the distribution of $\cos i$ is narrower than suggested by the measurement of ς, which implies that the masses have already a significantly narrower distribution than we would obtain from the measurement of ς and h_3 alone.

As the timing baseline T increases, the uncertainty of $\dot{\omega}$ will decrease proportionally to $T^{-3/2}$ (while for ς and h_3, the uncertainties will decrease with $T^{-1/2}$, which implies that the area of the M_c - $\cos i$ plane allowed by the Shapiro delay measurement will decrease with T^{-1}). As we can see in Figure 5.7, a more precise $\dot{\omega}$ will, in combination with the Shapiro delay, yield much more precise masses.

5.5 Conclusions

Recycled pulsars are the major motivation for many large scale pulsar surveys; they present unique studies in physical applications and evolutionary studies of the end phase of binaries. Here we presented the follow-up and timing for six recycled pulsars discovered in the AO327 pulsar survey. Five of the recycled pulsars were found to be in a binary system, with four of them having He WD companions and one with either a CO or ONeMg WD companion. Three of these pulsars (PSRs J0509+0856, J0709+0458 and J0732+2314) are being used in PTAs in efforts to detect low-frequency GWs. The AO327 pulsar survey keeps discovering pulsars that have good timing precision. This happens because of the short exposure times (60 s) and the large sensitivity of the telescope; which in return finds the brightest pulsars that also happen to have sharp profile features.

We were able to measure post-Keplerian parameters for two of our new systems, PSR J0709+0458

[6]We chose the latter variable instead of M_c in order to optimally cover all the regions of the plane with relatively good fits to the timing data (i.e., with a low χ^2), thus spending less time on regions of the parameter space with very poor fits - the latter have negligible associated probability.

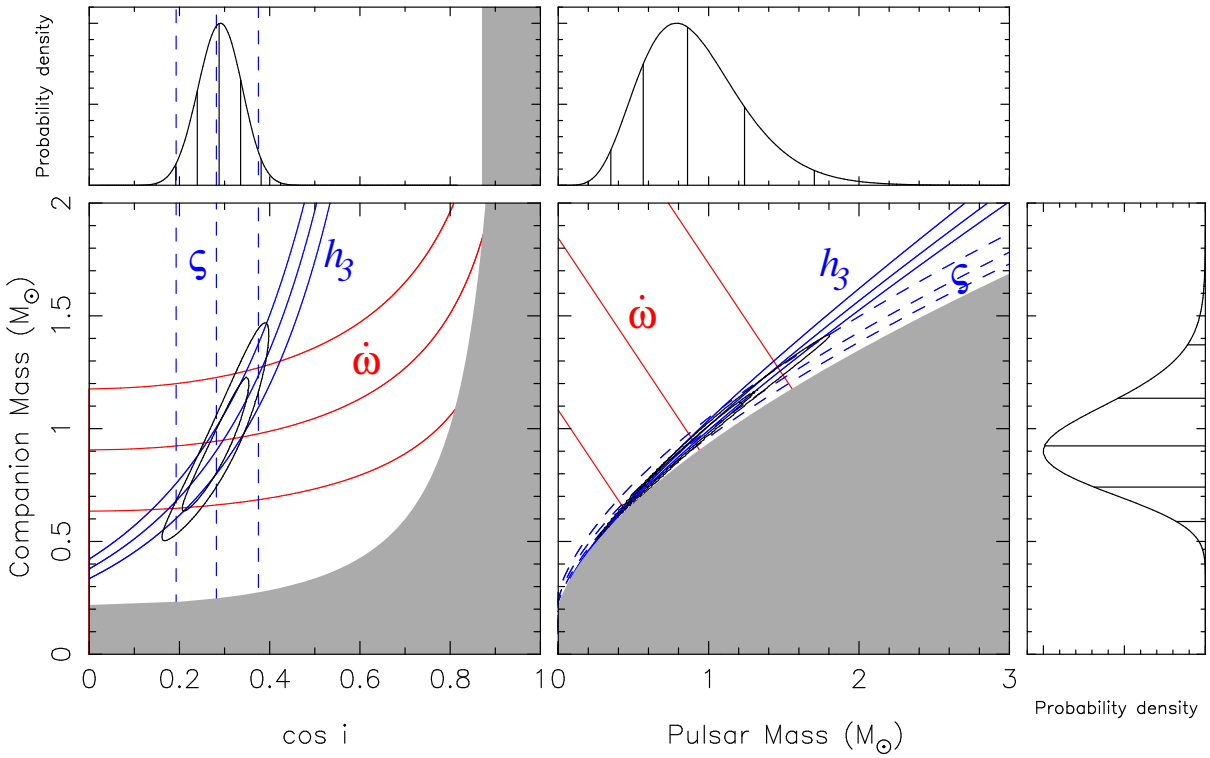

Figure 5.7. Mass constraints for PSR J10709+0458. In the lower plots, the lines indicate the regions that are (according to general relativity) consistent with the nominal and $\pm 1\sigma$ measurements of h_3 (solid blue), ς (dashed blue) and $\dot{\omega}$ (solid red) obtained from the DDFWHE model (see Table 5.1). The contour plots include 68.23 and 95.44% of the total 2-dimensional probability density function (PDF), derived from the quality (χ^2) of the TEMPO fits using a DDGR model to the ToA data set we have obtained for this pulsar. The location of the regions of high probability is well described by the h_3 and ς parameters and their uncertainties, with an important influence from $\dot{\omega}$: note that the distribution of $\cos i$ is narrower than suggested by the measurement of ς. In the left plot, we display the cosine of the orbital inclination ($\cos i$, which has, for randomly inclined orbits, a flat PDF) versus the companion mass (M_c); the gray region is excluded because the pulsar mass (M_p) must be larger than 0. In the right plot, we display M_p versus M_c; the gray region is excluded by the constraint $\sin i \leq 1$. The side panels display the 1-d PDFs for $\cos i$ (top left), M_p (top right) and M_c (right). The vertical lines in these PDFs indicate the median and the percentiles corresponding to 1 and 2 σ around the median.

and J0824+0028, and for the first system we were able to determine the component masses, albeit at low precision. Continued timing observations should substantially improve these PK parameters and, at least in the first case, determine precise component masses in the not too distant future.

The short exposure time implies that the survey is not strongly biased against the discovery of MSPs in tight orbits, should they exist in large numbers. Despite this, all the systems we have discovered to date have relatively wide orbits. This suggests that compact binaries are a relatively rare population, at least for the high Galactic latitudes probed by this survey.

Table 5.1. Timing Parameters for Six Pulsars

PSR	J0154+1833	J0509+0856	J0709+0458	J0732+2314	J0824+0028	J2204+2700
Right Ascension (RA), α (J2000)	01:54:36.88273(3)	05:09:22.23486(1)	07:09:08.36540(1)	07:32:37.5153(8)	08:24:24.84028(5)	22:04:43.609(3)
Declination (decl.), δ (J2000)	+18:33:50.758(9)	+08:56:25.0247(8)	+04:58:51.4940(5)	+23:14:54.18(7)	00:28:0.570(2)	+27:00:54.69(4)
Proper Motion RA, μ_α(masyr^{-1})	10.3(9)	5.4(1)	-0.9(1)	–	-4.9(4)	–
Proper Motion decl, μ_δ(masyr^{-1})	-8.9(1.9)	-4.3(5)	-1.2(3)	–	-10.9(1.4)	–
Pulsar Period, P(s)	0.0023645697763005(4)	0.0040558382315642(6)	0.0344289781774587(9)	0.004090137082359(4)	0.009861348670368(1)	0.0847026154913(2)
Period Derivative, $\dot{P}$ (10^{-20} ss^{-1})	0.292(1)	0.441(1)	38.035(1)	0.61(3)	14.688(1)	13.09(0.20)
Dispersion Measure, DM (pc cm^{-3}) ...	19.7978(1)	38.318(4)	44.2679(5)	44.6723(1)	34.5485(6)	35.074(1)
DM derivative, DM1 (pc cm^{-3} yr^{-1}) ...	0.0013(1)	0.0006(2)	-0.0004(1)	-0.0057(8)	–	–
DM derivative, DM2 (pc cm^{-3} yr^{-2}) ...	–	–	0.0011(1)	0.064(7)	–	–
Rotation measure, (rad m^2)	21.6(1)	42.4(6)	43.4(3)	3.6(1.4)	39.3(5)	–
Binary Parameters						
Orbital model	–	ELL1	DDGR	DDH	DDH	DD
Orbital Period, P_b (days)	–	4.907976893(1)	4.3666799229(1)	30.2300768(4)	23.206955707(5)	815.24544(6)
Projected Semi-major Axis, x (lt-s)	–	2.4580255(3)	15.7165842(3)	10.625839(1)	18.988922(4)	210.68063(5)
Epoch of Periastron, T_0 (MJD)	–	56519.61(1)	56983.4412(1)	57753.2(2)	56519.295(2)	56635.37(3)
Orbital Eccentricity, e	–	0.0000227(3)	0.00022539(2)	0.0000092(1)	0.00023063(8)	0.0015227(8)
Longitude of Periastron, ω (°)	–	32.3(8)	322.721(9)	72.8(1.8)	46.31(3)	6.40(1)
Derived parameters						
Mass Function, f ($M_\odot$)	–	0006619679(3)	0.21860219(1)	0.0014095937(4)	0.0136504619(9)	0.0151070557(9)
Min. Companion Mass, M_c ($M_\odot$)	–	0.11	1.11	0.15	0.34	0.36
Galactic Longitude, l	143.18	192.48	210.49	195.93	223.57	82.99
Galactic Latitude, b	-41.80	-17.93	6.20	19.03	20.78	-22.64
DM Derived Distance*, d_1/d_2 (kpc)	0.86/1.62	1.45/0.82	1.79/1.20	1.66/1.15	1.53/1.68	2.15/3.15
Galactic height, z_1/z_2 (kpc)	-0.57/-1.08	-0.45/-0.25	0.19/0.13	0.54/0.37	0.54/0.59	-0.82/-1.22
Transversal velocity, $v_\perp$(km s^{-1})	56(14)	48(2)	12(3)	–	74(18)	50(12)
Intrinsic spin period derivative $P_{int}^{\cdot}$(ss^{-1}).	$2.2^{+0.2}_{-0.2} \times 10^{-21}$	$3.5^{+0.2}_{-0.2} \times 10^{-21}$	$377.7^{+0.6}_{-0.6} \times 10^{-21}$	$5.9^{+0.06}_{-0.06} \times 10^{-21}$	$143.4^{+0.9}_{-0.9} \times 10^{-21}$	$139.2^{+1.2}_{-1.1} \times 10^{-21}$
Surface Magnetic Field Strength B_0 (10^8 G)	0.7	1.2	36.4	1.6	1.2	34.6
Characteristic Age, τ_c (Gyr)	16.9	18.2	1.4	11	1.1	9.6
Spin-down Luminosity, $\dot{E}$ (ergs s^{-1})	6.59×10^{33}	2.1×10^{33}	3.7×10^{32}	3.4×10^{33}	5.9×10^{33}	9.0×10^{30}
Observations parameters						
Timing epoch (MJD)	56900	57384	56983	58000	56600	56805
Span of timing data (MJD)	56550-57809	56516-58251	56600-58328	57522-58265	56499-58213	55338-58327
Number of TOAs	504	307	1518	478	824	295
Integration time per TOA (min)	5	5	5	5	5	5
TOA error scale factor (search/fold)	–	2.04/1.5	1.2/1.1	–/1.76	–/–	1.04/1.07
rms post-fit residuals (μs)	1.18	3.44	5.01	4.41	4.66	79.94

* The distance is derived from the DM using (Cordes & Lazio, 2002) (d_1) and Yao et al. (2016) (d_2) model of the Galactic electron density.

Chapter 6

Summary and future work

6.1 Summary

In this thesis, we studied recycled radio pulsars; how they are discovered, how they are timed, and revealed aspects of the science of the timing analysis. Indeed, timing of recycled pulsars has many important applications, such as the study of ultra-dense matter (Özel & Freire, 2016), the tests of relativistic theories of gravity (Kramer et al., 2006), the search for low-frequency gravitational waves (Verbiest et al., 2016), and evolution of binary systems (Bhattacharya & van den Heuvel, 1991; Tauris et al., 2011, 2012). I have done a full study from the discovery, to follow-up observations, and timing analysis for the 8 recycled pulsars in this thesis, with a focus on measuring their masses and their evolutions.

The vast majority of the precise mass measurements of neutron stars have been performed using radio observations of binary pulsars. Isolated radio pulsars masses cannot be measured, since all of the current methods rely on precise tracking of the orbital motions through pulsar timing of binary pulsars. It is important to probe the distribution of neutron star masses in order to understand the nature of supernovae and neutron star formations, as well as binary stellar evolution and their interactions. In Chapter 3, we report of the discovery of the first asymmetric double neutron star (DNS) system. We measure the individual masses of the 4.07 day binary pulsar J0453+1559 after measured the rate of advance of periastron and Shapiro delay. The mass of the pulsar is $M_p = 1.559 \pm 0.005 M_\odot$ and the companion is $M_c = 1.174 \pm 0.004 M_\odot$, having a mass ration of $q = 0.75$. This system was the first DNS with mass ratio less to unity as compared to the others before ($q \geq 0.91$). The companion is a neutron star, as indicated by the orbital eccentricity of the system ($e = 0.11$), and its the smallest precisely measured mass for any neutron star, to this date. PSR J0453+1559 has a spin period of 45.7 ms and a spin period derivative $\dot{P} = (1.8616 \pm 0.0007) \times 10^{-19}$s s^{-1}; from these we derived a characteristic age of $\sim 4.1 \times 10^9$ years and a surface magnetic field strength of $\sim 2.9 \times 10^9$ G. This pulsar was mildly recycled by accretion of matter from the progenitor of the companion star. This suggests that it was formed with (approximately) its current mass. Hence neutron stars form with a wide range of masses, which is important for understanding their formation in supernovae (Tauris et al., 2017). It is now evident that we should not assume all DNS systems are symmetric, which is important for the search for gravitational waves released during a DNS mergers.

In Chapter 4, we report the initial follow-up of PSR J1411+2551, another DNS system discovered in the AO327 survey. The timing observations reveal a precise measurement of its spin period (62.4 ms) and its derivative ($\dot{P} = 9.6 \pm 0.7 \times 10^{-20}$ s s^{-1}); from these, we derive a characteristic age of $\sim 9.1 \times 10^9$ and a surface magnetic field strength of $\sim 2.6 \times 10^9$ G. These numbers indicate that this pulsar was mildly recycled. The system has an eccentric ($e = 0.17$) 2.61 day orbit, which allows for a precise measurement of the rate of advance of periastron, $\dot{\omega} = 0.07686 \pm 0.00046^\circ$yr^{-1}. By assuming GR accurately describes the orbital motion, this implies a total system mass of $M_{\rm tot} = 2.538 \pm 0.022 M_\odot$. Since there was no other PK measured for this system, the individual masses were not measurable; but using the mass function we

determined a minimum companion mass of $> 0.92 M_{\odot}$ and the maximum pulsar mass is $< 1.6 M_{\odot}$. The companion mass and especially the orbital eccentricity suggest that PSR J1411+2551 is a DNS; among the lightest known to date. Furthermore, the relatively low orbital eccentricity and small proper motion limits suggest that the second supernova had a relatively small associated kick; this and the low system mass suggest that it was an ultra-stripped supernova (Tauris et al., 2017).

Chapter 5 is a study of several types of recycled pulsars discovered in AO327 survey. We must discover and study the largest number possible of all recycled pulsars in a way that is as unbiased as possible, to fully understand their evolution and population. In this chapter, we present the discovery and timing solutions of five recycled pulsars in binary systems (PSRs J0509+0856, J0709+0458, J0732+2314, J0824+0028, J2204+2700) and one isolated millisecond pulsar (PSR J0154+1833). All these pulsars have a low DM of ($\lesssim 45\,\mathrm{pc\,cm^{-3}}$), and have a DM-determined distance of $\lesssim 3$ kpc. Their timing solutions, which have data spans ranging from 1 to ~ 7 years, include precise estimates of their spin and astrometric parameters, and for the binaries, precise estimates of their Keplerian binary parameters:

- PSR J0154+1833 is an isolated MSP with a spin period of 2.36 ms and a DM of 19.79 pc cm^{-1}. The evolution scenario for isolated millisecond pulsars is a mystery. There are two hypothesis that may explain their evolution. One is that some MSPs are evaporating their companion, a hypothesis coming from the first eclipsing pulsar binary system, which are now known as 'black-widow' system (Fruchter et al., 1988). These 'black-widow' systems have an eclipsing orbital periods ($\sim$ few hours) and very low mass companions ($\lesssim 0.1 M_{\odot}$). The companion is undergoing mass loss from being ablated by the strong wind of the pulsar. This was believed that the strong ablation process seen in PSR B1957+20 and similar objects could eventually make the companion star completely evaporate, thus providing an explanation for the existence of isolated MSPs in the Galaxy (Fruchter et al., 1988). However, it was later realized that the typical timescale for such a process would be too long (more than a Hubble time) to complete and thus the idea was abandoned (Ryba & Taylor, 1991). Another hypothesis is that some isolated MSPs are ejected from globular clusters (GCs). Many exchange encounters happen inside GCs, where some isolated MSPs are located within or just outside GC, some could even be kicked out fully from GCs gravitational wells. Nevertheless, up to this date, no hypothesis fully describes how the total population of isolated MSPs in our galaxy are formed.

- PSR J0509+0856 is an binary MSP with a spin period of 4.05 ms and a DM of 38.25 pc cm^{-1}. It is in a 4.90 day almost circular ($e = 0.000023$) orbit. No PK parameters were measurable in this system, due to its very circular eccentricity and relatively large orbit. By using its measured orbital parameters with the mass function we get a minimum companion mass of 0.11 $M_{\odot}$ and a median companion mass of 0.13 $M_{\odot}$. Even though the companion mass is a bit low of a Helium WD, the spin period of the pulsar and the orbital eccentricity are compatible with those of other MSP − Helium WD. This suggests that, if the companion is a Helium WD, then the system has a low orbital inclination, which is consistent with the non-detection of the Shapiro delay in this system. This pulsar has very good timing precision and has been included in the timing campaign carried out by NANOGrav.

- PSR J0709+0458 is a almost circular ($e = 0.00022$) binary MRP that has a measure-

ment, with some precision, of the rate of advance of periastron, and also a detection of Shapiro delay. Generally a pulsar binary system with an this eccentricity would make the measurement of $\dot{\omega}$ impossible. This was only possibly given by the high timing precision of the system and the large companion mass ($0.6 \geq 1.4$ $M_{\odot}$). In a couple of decades this system will have precise individual mass measurements once a more precise measurement of $\dot{\omega}$ has been reached. This pulsar has also been included in the timing campaign by NANOGrav.

- PSR J0732+2314 is a binary MSP with no PK parameters measured. The apparently low companion mass and the lack of a detection of Shapiro delay is consistent with our rotating vector model (Radhakrishnan & Cooke, 1969), which resulted in the measurement of the system's inclination angle $i \sim 53^{+2.4}_{-2.5}$ degrees. This pulsar follows the Phinney (1992) relationship, where MSP−Helium WD binaries are in almost circular binary system. There was a noticeable gap within the range of $P_b \sim 22-32$ days where the population is dominated by recent eccentric binaries that also have Helium WD companions (Stovall et al., 2019, and references therein). These eccentric binaries have shown that not all MSP−Helium WD follow the original evolution scenario of Phinney (1992) but now by Antoniadis (2014). This new hypothesis proposes that the orbital eccentricity is caused by material ejected from the He WD due to unstable hydrogen shell burning. Nevertheless PSR J0732+2314, shows that not all such systems in this interval of orbital periods become eccentric. This pulsar has also been included in the timing campaign by NANOGrav.

- PSR J0824+0028 is a binary MSP with a low significance detection of Shapiro delay but no other PK parameters. Even though there is no detection of the rate of advance of periastron, more observations at superior conjunction could lead to individual mass measurements from Shapiro delay alone, as done by other systems (Demorest et al., 2010, and references therein). The orbital eccentricity of the system and spin period of the pulsar matches well to the Phinney (1992) relation. Similar to PSR J0732+2314, its orbital period is also inside the range dominated by the eccentric binaries. However the companion for PSR J0824+0028 is not likely a He WD, its minimum mass estimate from the mass function gives a more massive WD, likely a CO WD.

- PSR J2204+2700 is a binary MRP with the seventh largest orbital period (815.2 day) of any pulsar binary. This pulsar is a good candidate for Damour-Schäfer test of the strong equivalence principle (SEP). Binary pulsars with low companions mass, small eccentricity, and long orbital periods are ideal for SEP tests, as demonstrated in Gonzalez et al. (2011).

In order to expand our knowledge about all pulsars, we must study as many possible. The continuation of more sensitive pulsar surveys and studying more interesting discoveries will further increase to the vast scientific potential of pulsars.

6.2 Future work

The search for pulsars still continues in the HTRU-N survey, since there is a lot more data to process. In this thesis, as of today, I have only processed 4505 beams in the mid-lat region ($|b| < 15°$), where a total of 126136 beams have been observed in this region. The entire survey,

to this date, has a total of 359257 beams observed. At this moment, this survey's full potential has not yet even been fully explored. There are many pulsars waiting to be discovered in this survey, since it is the only norther sky survey at center frequency 1.36 GHz.

At the end of writing this thesis, I will be responsible for the continued of timing all new pulsars from the AODrift survey. This includes the continuation of timing systems like PSR J0709+0458 and J0824+0028, where in the future individual mass measurements are possible. Apart from that, I discovered four new recycled pulsars (see discovery plots in Figure 6.4, 6.3, 6.1, 6.2) during my doctoral studies, three MSP and one isolated MRP that seems to be a disrupted recycled pulsar (DRP). A DRP has the same evolutionary scenario as high-mass binary system (as mentioned in Section 1.3.3.2). Although for the case of a DRPs, they are suggested to be remains of a high-mass binary system that was disrupted at the time of the second supernova explosion (Lorimer et al., 2004). The follow-up of all known DRPs, could help determine an estimate of the second supernova explosion kick by measuring the proper motion of the DRPs. Most DRPs have been neglected for timing observations, since they are isolated pulsars.

The future of pulsar searching will be up to the next generation of radio telescopes. Already one of these telescopes has been continuing the hunt for new pulsars. The Five-hundred-meter Aperture Spherical Telescope[1] (FAST; Nan et al., 2011), is a spherical reflector of 500 meters in diameter with a 300 meter illuminated area, located in the Guizhou Province, Southwest China. This huge collecting area allows it to reach very high sensitivities over very short time scales, an ideal instrument for searching for highly relativistic binary systems. So far this telescope has discovered a running total of 64 new radio pulsars[2]. There are also two other major radio telescopes that will be soon be available to radio astronomers. The first is MeerKAT[3], an array of 64 dishes, each 13.5 meters in diameter, located in South Africa. The first observations have began and show a much higher sensitivity than expected. This is a result from its large collection area and wide observing bandwidth. This telescope is, for now, the most sensitive radio telescope in the Southern Hemisphere until the completion of the Square Kilometre Array[4] (SKA). The SKA will be a telescope composed of a thousands of small antennas, which will be located across two continents in South Africa and Australia. Once the SKA will be fully completed, it will have a collecting area of $\sim$ 1 kilometer. No other radio telescope in the world would compare to the unprecedented sensitivity of SKA! Thus this will very likely produce major advances in many scientific areas, could be capable of doubling the known pulsar population, and maybe even discovering radio pulsars beyond our galaxy.

[1] http://fast.bao.ac.cn/en/
[2] http://crafts.bao.ac.cn/pulsar/
[3] http://public.ska.ac.za/meerkat
[4] https://www.skatelescope.org/

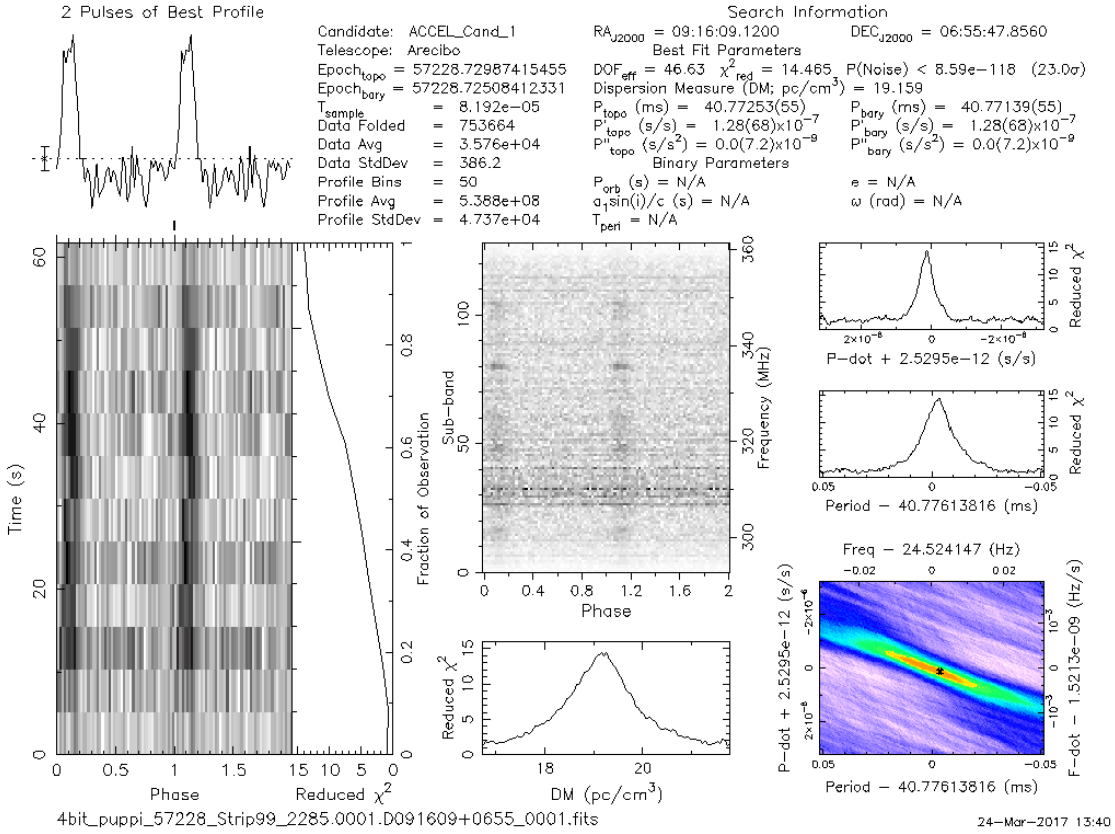

Figure 6.1. This is a PRESTO's folded plot of the confirmation observation of PSR J0916+06, a discovery I made in AODrift from June 22, 2017.

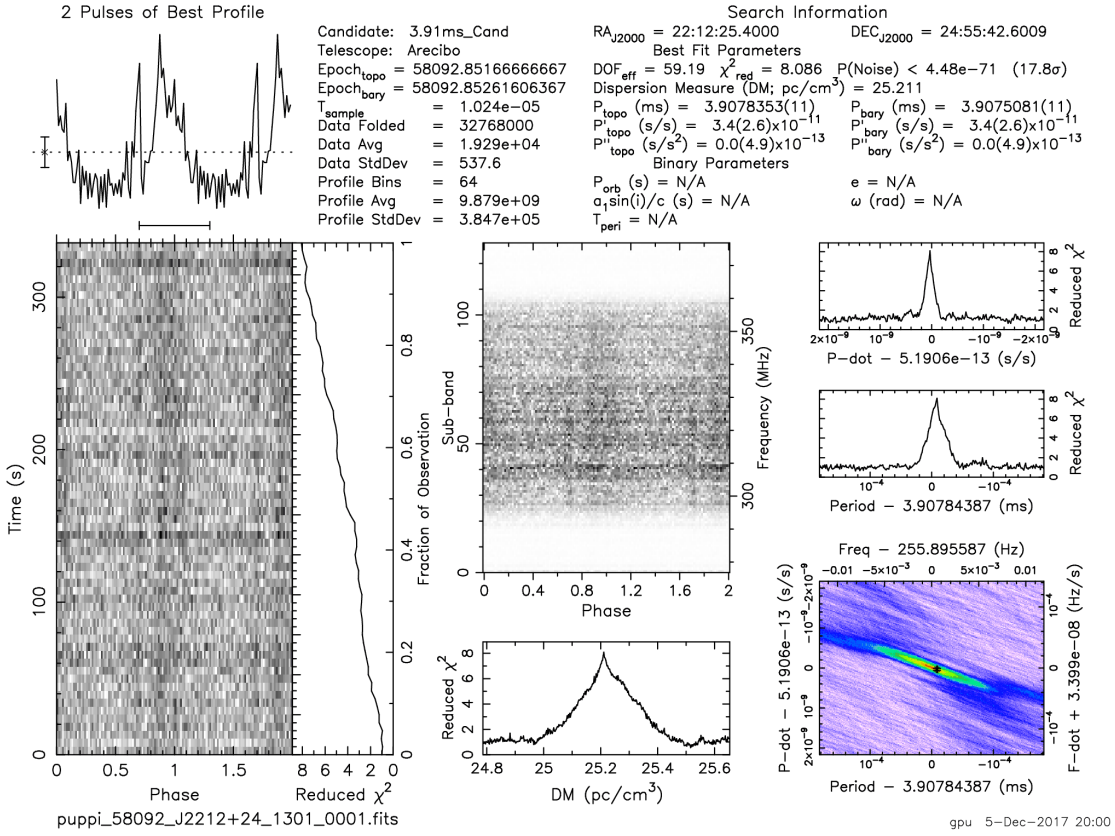

Figure 6.2. This is a PRESTO's folded plot of the confirmation observation of PSR J2202+21, a discovery I made in AODrift from November 10, 2017.

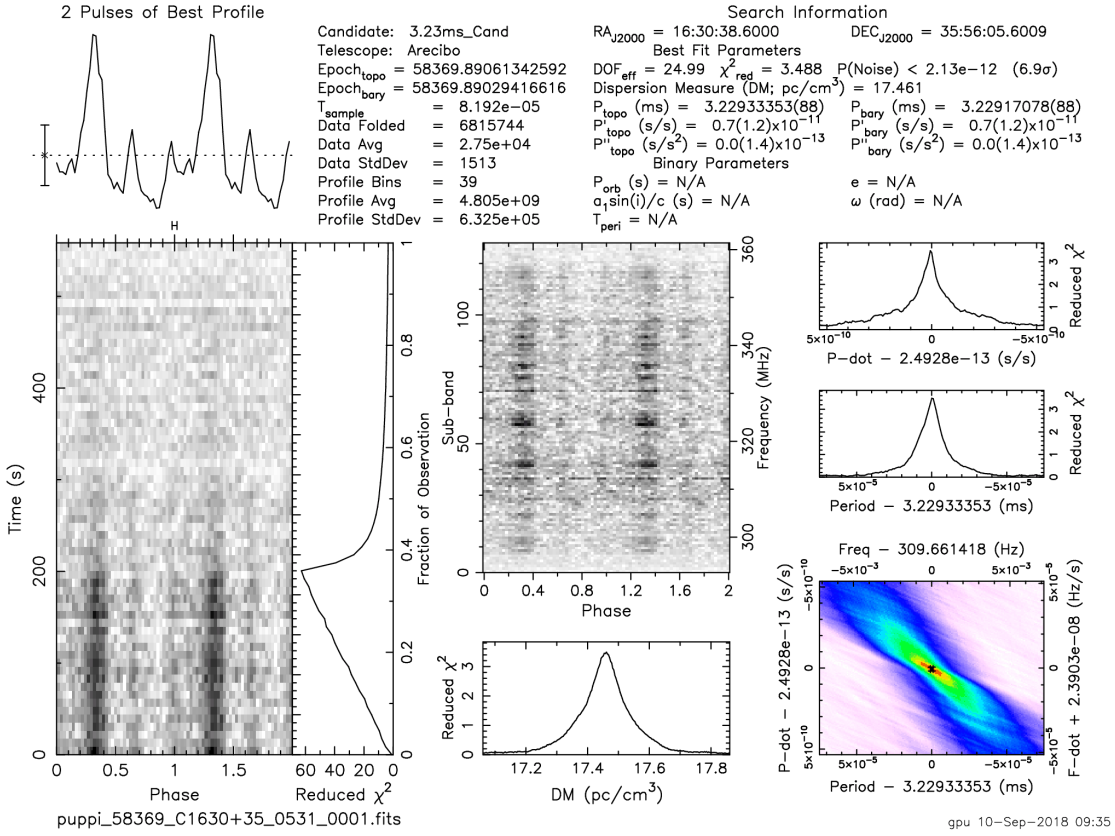

Figure 6.3. This is a PRESTO's folded plot of the confirmation observation of PSR J1630+35, a discovery I made in AODrift from January 17, 2018.

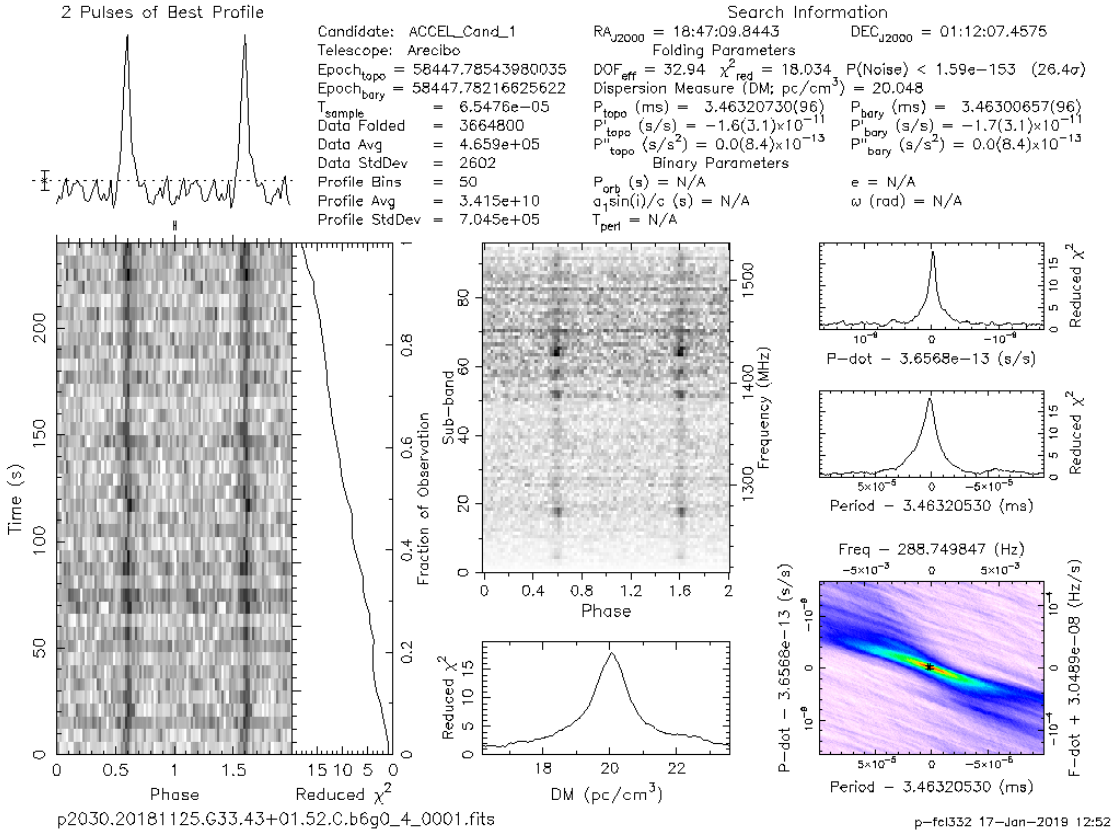

Figure 6.4. This is a PRESTO's folded plot of the confirmation observation of PSR J1847+01, a discovery I made in PALFA from January 22, 2019.

Bibliography

Abadie J., et al., 2012, Phys. Rev. D, 85, 082002 (Cited on page 64.)

Abbott B. P., et al., 2009, Phys. Rev. D, 79, 122001 (Cited on page 64.)

Abbott B. P., et al., 2016, Physical Review Letters, 116, 061102 (Cited on pages 24 and 66.)

Abbott B. P., et al., 2017, Physical Review Letters, 119, 161101 (Cited on pages 66, 73, 74 and 109.)

Abdo A. A., et al., 2009, ApJ, 699, 1171 (Cited on page 85.)

Alpar M. A., Cheng A. F., Ruderman M. A., Shaham J., 1982, Nature, 300, 728 (Cited on pages 23 and 76.)

Anderson S., Gorham P., Kulkarni S., Prince T., Wolszczan A., 1989, IAU Circ., 4772, 1 (Cited on page 55.)

Antoniadis J., 2014, ApJ, 797, L24 (Cited on pages 85, 95 and 110.)

Antoniadis J., van Kerkwijk M. H., Koester D., Freire P. C. C., Wex N., Tauris T. M., Kramer M., Bassa C. G., 2012, MNRAS, 423, 3316 (Cited on page 64.)

Antoniadis J., et al., 2013, Science, 340, 448 (Cited on pages 25, 64, 73 and 76.)

Antoniadis J., Kaplan D. L., Stovall K., Freire P. C. C., Deneva J. S., Koester D., Jenet F., Martinez J. G., 2016, ApJ, 830, 36 (Cited on pages 67 and 77.)

Archibald A. M., et al., 2009, Science, 324, 1411 (Cited on pages 23 and 24.)

Archibald R. F., et al., 2016, ApJ, 819, L16 (Cited on page 16.)

Archibald A. M., et al., 2018, Nature, 559, 73 (Cited on page 76.)

Arzoumanian Z., Joshi K., Rasio F. A., Thorsett S. E., 1996, in Johnston S., Walker M. A., Bailes M., eds, Astronomical Society of the Pacific Conference Series Vol. 105, IAU Colloq. 160: Pulsars: Problems and Progress. pp 525–530 (arXiv:astro-ph/9605141) (Cited on pages 60 and 72.)

Arzoumanian Z., et al., 2018, ApJ, 859, 47 (Cited on pages 76 and 78.)

Atwood W. B., et al., 2009, ApJ, 697, 1071 (Cited on page 85.)

Baade W., Zwicky F., 1934, Proceedings of the National Academy of Science, 20, 259 (Cited on page 13.)

Backer D. C., Kulkarni S. R., Heiles C., Davis M. M., Goss W. M., 1982, Nature, 300, 615 (Cited on page 23.)

Barr E. D., et al., 2013a, MNRAS, 429, 1633 (Cited on page 30.)

Barr E. D., et al., 2013b, MNRAS, 435, 2234 (Cited on pages 30, 33 and 66.)

Barr E. D., Freire P. C. C., Kramer M., Champion D. J., Berezina M., Bassa C. G., Lyne A. G., Stappers B. W., 2017a, MNRAS, 465, 1711 (Cited on pages 83, 85 and 110.)

Barr E. D., Freire P. C. C., Kramer M., Champion D. J., Berezina M., Bassa C. G., Lyne A. G., Stappers B. W., 2017b, MNRAS, 465, 1711 (Cited on page 88.)

Bhat N. D. R., Cordes J. M., Camilo F., Nice D. J., Lorimer D. R., 2004, ApJ, 605, 759 (Cited on page 41.)

Bhattacharya D., van den Heuvel E. P. J., 1991, Phys. Rep., 203, 1 (Cited on pages 23, 24, 52, 76 and 93.)

Blandford R., Teukolsky S. A., 1976, ApJ, 205, 580 (Cited on page 50.)

Britton M. C., 2000, ApJ, 532, 1240 (Cited on page 43.)

Burgay M., et al., 2003, Nature, 426, 531 (Cited on pages 24, 54, 55 and 66.)
Cameron A. D., et al., 2018, MNRAS, 475, L57 (Cited on page 76.)
Camilo F., Rasio F. A., 2005, in Rasio F. A., Stairs I. H., eds, Astronomical Society of the Pacific Conference Series Vol. 328, Binary Radio Pulsars. p. 147 (arXiv:astro-ph/0501226) (Cited on page 30.)
Camilo F., et al., 2015, ApJ, 810, 85 (Cited on pages 83, 85 and 110.)
Casares J., Jonker P. G., Israelian G., 2017, preprint, (arXiv:1701.07450) (Cited on page 66.)
Champion D. J., Lorimer D. R., McLaughlin M. A., Cordes J. M., Arzoumanian Z., Weisberg J. M., Taylor J. H., 2004, MNRAS, 350, L61 (Cited on page 55.)
Champion D. J., et al., 2005, MNRAS, 363, 929 (Cited on page 55.)
Champion D. J., et al., 2010, ApJ, 720, L201 (Cited on page 24.)
Chen K., Ruderman M., 1993, ApJ, 402, 264 (Cited on page 23.)
Cognard I., et al., 2011, ApJ, 732, 47 (Cited on page 30.)
Cooley J. W., Tukey J. W., 1965, Math. Comput., 19, 297 (Cited on page 36.)
Cordes J. M., Lazio T. J. W., 2002, ArXiv Astrophysics e-prints, (Cited on pages 18, 59, 70, 78 and 91.)
Cordes J. M., et al., 2006, ApJ, 637, 446 (Cited on pages 30 and 66.)
Corongiu A., Kramer M., Stappers B. W., Lyne A. G., Jessner A., Possenti A., D'Amico N., Löhmer O., 2007, A&A, 462, 703 (Cited on page 55.)
Damour T., Deruelle N., 1985, Ann. Inst. Henri Poincaré Phys. Théor., Vol. 43, No. 1, p. 107 - 132, 43, 107 (Cited on pages 50, 51, 57 and 68.)
Damour T., Deruelle N., 1986, Ann. Inst. Henri Poincaré Phys. Théor., Vol. 44, No. 3, p. 263 - 292, 44, 263 (Cited on pages 50, 51, 57, 68 and 78.)
Damour T., Taylor J. H., 1991, ApJ, 366, 501 (Cited on pages 57, 60 and 79.)
Damour T., Taylor J. H., 1992, Phys. Rev. D, 45, 1840 (Cited on page 52.)
Demorest P. B., Pennucci T., Ransom S. M., Roberts M. S. E., Hessels J. W. T., 2010, Nature, 467, 1081 (Cited on pages 64 and 95.)
Deneva J. S., Stovall K., McLaughlin M. A., Bates S. D., Freire P. C. C., Martinez J. G., Jenet F., Bagchi M., 2013, ApJ, 775, 51 (Cited on pages 30, 33, 54, 66, 67 and 77.)
Deneva J. S., et al., 2016, ApJ, 821, 10 (Cited on pages 40 and 67.)
Drout M. R., et al., 2017, preprint, (arXiv:1710.05443) (Cited on page 73.)
Eatough R. P., Molkenthin N., Kramer M., Noutsos A., Keith M. J., Stappers B. W., Lyne A. G., 2010, MNRAS, 407, 2443 (Cited on page 40.)
Edwards R. T., Hobbs G. B., Manchester R. N., 2006, MNRAS, 372, 1549 (Cited on pages 42, 44, 52 and 57.)
Espinoza C. M., Lyne A. G., Kramer M., Manchester R. N., Kaspi V. M., 2011, ApJ, 741, L13 (Cited on page 16.)
Everett J. E., Weisberg J. M., 2001, ApJ, 553, 341 (Cited on page 43.)
Faulkner A. J., et al., 2005, ApJ, 618, L119 (Cited on pages 55 and 64.)
Ferdman R. D., et al., 2010, ApJ, 711, 764 (Cited on page 64.)
Ferdman R. D., et al., 2013, ApJ, 767, 85 (Cited on page 66.)
Ferdman R. D., et al., 2014, MNRAS, 443, 2183 (Cited on pages 55, 64 and 69.)
Fonseca E., Stairs I. H., Thorsett S. E., 2014, ApJ, 787, 82 (Cited on page 55.)
Foster R. S., Backer D. C., 1990, ApJ, 361, 300 (Cited on page 24.)

Freire P. C. C., 2013, in van Leeuwen J., ed., IAU Symposium Vol. 291, Neutron Stars and Pulsars: Challenges and Opportunities after 80 years. pp 243–250 (arXiv:1210.3984), doi:10.1017/S1743921312023770 (Cited on page 30.)

Freire P. C. C., Ridolfi A., 2018, MNRAS, 476, 4794 (Cited on pages 42 and 77.)

Freire P. C. C., Wex N., 2010, MNRAS, 409, 199 (Cited on pages 51, 57, 62, 78 and 85.)

Freire P. C., Kramer M., Lyne A. G., 2001, MNRAS, 322, 885 (Cited on page 49.)

Freire P. C. C., et al., 2011, MNRAS, 412, 2763 (Cited on page 64.)

Freire P. C. C., et al., 2012, MNRAS, 423, 3328 (Cited on pages 23, 25, 64 and 76.)

Fruchter A. S., Stinebring D. R., Taylor J. H., 1988, Nature, 333, 237 (Cited on pages 23 and 94.)

Gold T., 1968, Nature, 218, 731 (Cited on page 14.)

Gonzalez M. E., et al., 2011, ApJ, 743, 102 (Cited on pages 84 and 95.)

Gravity Collaboration et al., 2018, A&A, 615, L15 (Cited on page 79.)

Han J. L., Manchester R. N., van Straten W., Demorest P., 2018, ApJS, 234, 11 (Cited on page 25.)

Hankins T. H., Rickett B. J., 1975, in Alder B., Fernbach S., Rotenberg M., eds, Volume 14 Vol. 14, Methods in Computational Physics. Volume 14 - Radio astronomy. pp 55–129 (Cited on page 32.)

Heiles C., et al., 2001, PASP, 113, 1274 (Cited on page 43.)

Hessels J. W. T., Ransom S. M., Stairs I. H., Freire P. C. C., Kaspi V. M., Camilo F., 2006, Science, 311, 1901 (Cited on pages 23 and 30.)

Hewish A., Bell S. J., Pilkington J. D. H., Scott P. F., Collins R. A., 1968, Nature, 217, 709 (Cited on pages 13, 17 and 31.)

Hobbs G., Edwards R., Manchester R., 2006, Chinese Journal of Astronomy and Astrophysics Supplement, 6, 189 (Cited on pages 42, 44 and 57.)

Hotan A. W., van Straten W., Manchester R. N., 2004, PASA, 21, 302 (Cited on pages 11, 42, 57, 68 and 78.)

Hotokezaka K., Kiuchi K., Kyutoku K., Okawa H., Sekiguchi Y.-i., Shibata M., Taniguchi K., 2013, Phys. Rev. D, 87, 024001 (Cited on page 64.)

Hulse R. A., Taylor J. H., 1975, ApJ, 195, L51 (Cited on pages 24, 54, 55 and 65.)

Jackson J. D., 1962, Classical Electrodynamics (Cited on page 15.)

Jacoby B. A., Cameron P. B., Jenet F. A., Anderson S. B., Murty R. N., Kulkarni S. R., 2006, ApJ, 644, L113 (Cited on page 55.)

Janssen G. H., Stappers B. W., Kramer M., Nice D. J., Jessner A., Cognard I., Purver M. B., 2008, A&A, 490, 753 (Cited on page 55.)

Jenet F. A., Hobbs G. B., Lee K. J., Manchester R. N., 2005, ApJ, 625, L123 (Cited on pages 24 and 25.)

Just O., Bauswein A., Ardevol Pulpillo R., Goriely S., Janka H.-T., 2015, preprint, (arXiv:1504.05448) (Cited on page 64.)

Keane E. F., Kramer M., Lyne A. G., Stappers B. W., McLaughlin M. A., 2011, MNRAS, 415, 3065 (Cited on page 40.)

Keane E. F., et al., 2017, preprint, (arXiv:1706.04459) (Cited on page 66.)

Keith M. J., Kramer M., Lyne A. G., Eatough R. P., Stairs I. H., Possenti A., Camilo F., Manchester R. N., 2009, MNRAS, 393, 623 (Cited on page 55.)

Keith M. J., et al., 2010, MNRAS, 409, 619 (Cited on pages 30 and 66.)

Keith M. J., et al., 2013, MNRAS, 429, 2161 (Cited on page 45.)
Kim C., Perera B. B. P., McLaughlin M. A., 2015, MNRAS, 448, 928 (Cited on page 66.)
Knispel B., et al., 2015, ApJ, 806, 140 (Cited on pages 83, 85 and 110.)
Kopeikin S. M., 1996, ApJ, 467, L93 (Cited on pages 60 and 72.)
Kramer M., et al., 2006, Science, 314, 97 (Cited on pages 25, 54, 55, 64, 66, 76 and 93.)
Lange C., Camilo F., Wex N., Kramer M., Backer D. C., Lyne A. G., Doroshenko O., 2001, MNRAS, 326, 274 (Cited on pages 46, 52 and 78.)
Large M. I., Vaughan A. E., Mills B. Y., 1968, Nature, 220, 340 (Cited on page 14.)
Lattimer J. M., Prakash M., 2001, ApJ, 550, 426 (Cited on pages 28, 73, 74, 107 and 109.)
Lazaridis K., et al., 2009, MNRAS, 400, 805 (Cited on page 79.)
Lee K. J., et al., 2013, MNRAS, 433, 688 (Cited on page 40.)
Lentati L., et al., 2015, MNRAS, 453, 2576 (Cited on page 76.)
Lorimer D. R., 2008, Living Reviews in Relativity, 11 (Cited on pages 25, 54 and 66.)
Lorimer D. R., 2011, SIGPROC: Pulsar Signal Processing Programs, Astrophysics Source Code Library (ascl:1107.016) (Cited on page 33.)
Lorimer D. R., Kramer M., 2004, Handbook of Pulsar Astronomy (Cited on pages 15, 17, 19, 20, 34, 40, 45, 49, 50, 52 and 61.)
Lorimer D. R., Lyne A. G., Camilo F., 1998, A&A, 331, 1002 (Cited on page 30.)
Lorimer D. R., et al., 2004, MNRAS, 347, L21 (Cited on page 96.)
Lorimer D. R., et al., 2006, ApJ, 640, 428 (Cited on page 55.)
Lorimer D. R., et al., 2015, MNRAS, 450, 2185 (Cited on page 60.)
Lynch R. S., Freire P. C. C., Ransom S. M., Jacoby B. A., 2012, ApJ, 745, 109 (Cited on page 55.)
Lyne A., Graham-Smith F., 2012, Pulsar Astronomy (Cited on page 14.)
Lyne A. G., Rickett B. J., 1968, Nature, 219, 1339 (Cited on page 20.)
Lyne A. G., Brinklow A., Middleditch J., Kulkarni S. R., Backer D. C., 1987, Nature, 328, 399 (Cited on page 30.)
Lyne A. G., et al., 2004, Science, 303, 1153 (Cited on pages 24, 54 and 66.)
Manchester R. N., 1988, Proceedings of the Astronomical Society of Australia, 7, 548 (Cited on page 30.)
Manchester R. N., et al., 2001, MNRAS, 328, 17 (Cited on page 30.)
Manchester R. N., Hobbs G. B., Teoh A., Hobbs M., 2005, AJ, 129, 1993 (Cited on pages 21, 23, 30 and 66.)
Manchester R. N., et al., 2010, ApJ, 710, 1694 (Cited on pages 43 and 83.)
Martinez J. G., et al., 2015, ApJ, 812, 143 (Cited on pages 67, 68, 69, 72 and 77.)
Martinez J. G., et al., 2017, ApJ, 851, L29 (Cited on page 77.)
McGaugh S., 2018, preprint, p. arXiv:1808.09435 (`arXiv:1808.09435`) (Cited on page 79.)
McLaughlin M. A., et al., 2006, Nature, 439, 817 (Cited on page 40.)
McMillan P. J., 2017, MNRAS, 465, 76 (Cited on pages 68 and 72.)
Metzger B. D., Giannios D., Thompson T. A., Bucciantini N., Quataert E., 2011, MNRAS, 413, 2031 (Cited on page 73.)
Nan R., et al., 2011, International Journal of Modern Physics D, 20, 989 (Cited on page 96.)
Nyquist H., 1928, Transactions of the American Institute of Electrical Engineers, Volume 47, Issue 2, pp. 617-624, 47, 617 (Cited on page 32.)

Octau F., Cognard I., Guillemot L., Tauris T. M., Freire P. C. C., Desvignes G., Theureau G., 2018, A&A, 612, A78 (Cited on pages 83, 85 and 110.)
Özel F., Freire P., 2016, ARA&A, 54, 401 (Cited on pages 25 and 93.)
Özel F., Psaltis D., Narayan R., Santos Villarreal A., 2012, ApJ, 757, 55 (Cited on page 64.)
Phinney E. S., 1992, Philosophical Transactions of the Royal Society of London Series A, 341, 39 (Cited on pages 83, 84, 85, 95 and 110.)
Podsiadlowski P., Rappaport S., Pfahl E. D., 2002, ApJ, 565, 1107 (Cited on pages 23 and 24.)
Press W. H., Teukolsky S. A., Vetterling W. T., Flannery B. P., 1992, Numerical recipes in FORTRAN. The art of scientific computing (Cited on page 36.)
Radhakrishnan V., Cooke D. J., 1969, Astrophys. Lett., 3, 225 (Cited on pages 83 and 95.)
Radhakrishnan V., Srinivasan G., 1982, Current Science, 51, 1096 (Cited on page 23.)
Ransom S. M., 2001, PhD thesis, Harvard University (Cited on pages 11 and 33.)
Ransom S. M., 2008, in Bassa C., Wang Z., Cumming A., Kaspi V. M., eds, American Institute of Physics Conference Series Vol. 983, 40 Years of Pulsars: Millisecond Pulsars, Magnetars and More. pp 415–423 (arXiv:0710.3626), doi:10.1063/1.2900267 (Cited on page 30.)
Ransom S. M., Eikenberry S. S., Middleditch J., 2002, AJ, 124, 1788 (Cited on pages 36 and 38.)
Ransom S. M., et al., 2011, ApJ, 727, L16 (Cited on pages 30 and 85.)
Ransom S. M., et al., 2014, Nature, 505, 520 (Cited on page 76.)
Ray P. S., et al., 2012, preprint, (arXiv:1205.3089) (Cited on page 30.)
Rezzolla L., Kumar P., 2015, ApJ, 802, 95 (Cited on page 73.)
Rezzolla L., Baiotti L., Giacomazzo B., Link D., Font J. A., 2010, Classical and Quantum Gravity, 27, 114105 (Cited on page 64.)
Rickett B. J., Coles W. A., Bourgois G., 1984, A&A, 134, 390 (Cited on page 20.)
Robertson H. P., 1938, Ann. Math., 38, 101 (Cited on page 69.)
Rosswog S., 2013, Royal Society of London Philosophical Transactions Series A, 371, 20272 (Cited on page 64.)
Rowlinson A., O'Brien P. T., Metzger B. D., Tanvir N. R., Levan A. J., 2013, MNRAS, 430, 1061 (Cited on page 73.)
Russell H. N., 1931, MNRAS, 91, 951 (Cited on page 14.)
Ryba M. F., Taylor J. H., 1991, ApJ, 380, 557 (Cited on page 94.)
Scheuer P. A. G., 1968, Nature, 218, 920 (Cited on page 20.)
Shannon C. E., 1949, IEEE Proceedings, 37, 10 (Cited on page 32.)
Shannon R. M., et al., 2015, Science, 349, 1522 (Cited on page 76.)
Shklovskii I. S., 1970, Soviet Ast., 13, 562 (Cited on pages 57, 60, 68, 72 and 79.)
Spitler L. G., et al., 2016, Nature, 531, 202 (Cited on page 40.)
Splaver E. M., Nice D. J., Arzoumanian Z., Camilo F., Lyne A. G., Stairs I. H., 2002, ApJ, 581, 509 (Cited on page 61.)
Staelin D. H., Reifenstein I. E. C., 1968, Science, 162, 1481 (Cited on page 14.)
Stovall K., et al., 2014, ApJ, 791, 67 (Cited on pages 30 and 66.)
Stovall K., et al., 2018, ApJ, 854, L22 (Cited on page 76.)
Stovall K., et al., 2019, ApJ, 870, 74 (Cited on pages 47, 77, 83, 85, 95, 108 and 110.)
Swiggum J. K., et al., 2015, ApJ, 805, 156 (Cited on page 55.)
Tauris T. M., Savonije G. J., 1999, A&A, 350, 928 (Cited on pages 79 and 83.)

Tauris T. M., Takens R. J., 1998, A&A, 330, 1047 (Cited on page 23.)
Tauris T. M., van den Heuvel E. P. J., 2006, Formation and evolution of compact stellar X-ray sources. pp 623–665 (Cited on pages 23, 24, 66 and 76.)
Tauris T. M., van den Heuvel E. P. J., Savonije G. J., 2000, ApJ, 530, L93 (Cited on page 24.)
Tauris T. M., Langer N., Kramer M., 2011, MNRAS, 416, 2130 (Cited on pages 23, 24, 52, 64, 76 and 93.)
Tauris T. M., Langer N., Kramer M., 2012, MNRAS, 425, 1601 (Cited on pages 23, 24, 52, 60, 68, 76, 79 and 93.)
Tauris T. M., Langer N., Moriya T. J., Podsiadlowski P., Yoon S.-C., Blinnikov S. I., 2013, ApJ, 778, L23 (Cited on page 71.)
Tauris T. M., Langer N., Podsiadlowski P., 2015, MNRAS, 451, 2123 (Cited on pages 63, 64, 71 and 76.)
Tauris T. M., et al., 2017, ApJ, 846, 170 (Cited on pages 66, 69, 71, 72, 93, 94 and 109.)
Taylor J. H., 1987, in MacCallum M. A. H., ed., General Relativity and Gravitation. pp 209–222 (Cited on page 51.)
Taylor J. H., 1992, Philosophical Transactions of the Royal Society of London Series A, 341, 117 (Cited on pages 44, 57, 68 and 78.)
Taylor J. H., Weisberg J. M., 1982, ApJ, 253, 908 (Cited on pages 25, 54 and 69.)
Taylor J. H., Weisberg J. M., 1989, ApJ, 345, 434 (Cited on page 51.)
The CHIME/FRB Collaboration et al., 2019, arXiv e-prints, (Cited on page 40.)
Thornton D., et al., 2013, Science, 341, 53 (Cited on page 40.)
Thorsett S. E., Arzoumanian Z., Camilo F., Lyne A. G., 1999, ApJ, 523, 763 (Cited on page 64.)
Verbiest J. P. W., et al., 2016, MNRAS, 458, 1267 (Cited on pages 24, 25 and 93.)
Verbunt F., Freire P. C. C., 2014, A&A, 561, A11 (Cited on page 23.)
Weisberg J. M., Huang Y., 2016, ApJ, 829, 55 (Cited on page 76.)
Weisberg J. M., Taylor J. H., Fowler L. A., 1981, Scientific American, 245, 74 (Cited on page 61.)
Weisberg J. M., Nice D. J., Taylor J. H., 2010, ApJ, 722, 1030 (Cited on pages 55 and 64.)
Wolszczan A., 1991, Nature, 350, 688 (Cited on page 55.)
Wolszczan A., Frail D. A., 1992, Nature, 355, 145 (Cited on page 25.)
Woosley S. E., Weaver T. A., 1986, ARA&A, 24, 205 (Cited on page 14.)
Yao J. M., Manchester R. N., Wang N., 2016, preprint, (`arXiv:1610.09448`) (Cited on pages 18, 79 and 91.)
Zhang B., Mészáros P., 2001, ApJ, 552, L35 (Cited on page 73.)
Zhu W. W., et al., 2014, ApJ, 781, 117 (Cited on page 40.)
van Leeuwen J., et al., 2015, ApJ, 798, 118 (Cited on page 55.)
van Straten W., Bailes M., 2011, PASA, 28, 1 (Cited on pages 11 and 56.)
van Straten W., Demorest P., Oslowski S., 2012, Astronomical Research and Technology, 9, 237 (Cited on pages 11, 42, 57, 68 and 78.)

List of Figures

List of Tables